RADIATION DAMAGE MONITORING IN HADRON FORWARD CALORIMETRY

by

İrem Zöğ

B.S., Computer Engineering, Boğaziçi University, 2017

Submitted to the Institute for Graduate Studies in
Science and Engineering in partial fulfillment of
the requirements for the degree of
Master of Science

Graduate Program in Physics
Boğaziçi University
2019

ACKNOWLEDGEMENTS

I am very grateful to my thesis advisor Prof. Erhan Gulmez for his endless support and guidance.

My thanks go to also my family and friends for their precious help and support throughout my life.

I thankfully acknowledge the TAEK (Grant Number: 2018 TAEK CERN A5.H6.-F2-18) and Bogazici University Research Fund (Grant Number: 18B03P2 and 14040) for their financial support in this work.

ABSTRACT

RADIATION DAMAGE MONITORING IN HADRON FORWARD CALORIMETRY

Placed at high absolute pseudorapidity, Hadron Forward (HF) calorimeters are exposed to high energy particles more than other parts of the CMS HCAL detector in CERN. Radiation resulting from high energy particles lead to a decrease in transparency of the HF quartz fibres, effecting the calibration and decreasing the lifetime of the calorimeter. Thus, observation of change in transparency of the HF quartz fibres with respect to the accumulated dose of radiation and time is crucial. From the first proposal in 2003 to 2018, radiation damage (RadDam) tests and measurements have been performed with the HCAL Laser System. Yet, the HCAL Laser generates wide pulses, resulting in signals spread over several time slices and are hard to analyse. A new light source that is specialized for the HF RadDam system has been proposed as part of the Phase I Upgrade of the HF calorimeter. In this thesis, the analysis of HF Online RadDam Measurements with the new specialized light source is described. Noisy events are eliminated using time-to-digital converter (TDC) information from the new electronic chips QIE10. No significant difference in radiation damage is observed in channels at a given pseudorapidity for varying azimuthal angle. The closer the channels are to the beam line, the more pronounced radiation damage and recovery become. Total systematic error is estimated as 0.5%.

ÖZET

İLERİ HADRON KALORİMETRESİNDE RADYASYON HASARI GÖZLEMİ

İleri Hadron Kalorimetresi yüksek mutlak psödorapiditede bulunduğundan dolayı, yüksek enerjili parçacıklara, Hadron Kalorimetresi'nin diğer parçalarından daha fazla maruz kalmaktadır. Yüksek enerjili parçacıkların oluşturduğu radyasyon, İleri Hadron Kalori- metresi'nin kuartz fiber kablolarının ışık geçirgenliğinde düşüşe yol açmaktadır. Bu durum kalorimetrenin kalibrasyonunu ve yaşam süresini belirlemektedir. Bundan dolayı, İleri Hadron Kalorimetresi'nin kuartz fiber kablolarının ışık geçirgenliğinin zamana ve toplam radyasyon dozuna göre değişiminin incelenmesi gereklidir. Kullanımının önerildiği 2003'den 2018'e kadar, radyasyon hasarı testleri ve gözlemi için Hadron Kalorimetresi'nin lazer sistemi kullanılmıştır. Ancak bu lazerden üretilen sinyal istenenden daha geniş olduğundan analizi güç olmuştur. İleri Hadron Kalorimetresi'nin Faz I güncellemeleri altında ise radyasyon hasarı gözlemi için özelleştirilmiş yeni bir lazer sistemi kullanılmaya başlanmıştır. Bu tezde yeni lazer sistemiyle alınan radyasyon hasar gözlemi verilerinin analizi anlatılmaktadır. İstenmeyen olaylar, QIE10'dan gelen TDC verileri kullanılarak ayıklanmıştır. Aynı η değerinde olan kanallarda azimutal açıya göre radyasyon hasarında anlamlı bir fark gözlemlenmemiştir. Kanalların çarpışma eksenine yakınlığı arttıkça radyasyon hasarları daha belirginleşmektedir. Toplam sistematik hata oranı %0.5 olarak hesaplanmıştır.

TABLE OF CONTENTS

LIST OF FIGURES

LIST OF TABLES

LIST OF SYMBOLS

^oC	Celsius
fC	Femto Coulomb
GeV	Giga electron-Volt
K	Kelvin
MeV	Mega electron-Volt
nm	Nano meter
ns	Nano seconds
Q	Charge
TeV	Tera electron-Volt
γ	Photon
η	Pseudorapidity
μ^-	Muon Particle
τ^-	Tau Particle
ϕ	Azimuthal Angle

LIST OF ACRONYMS/ABBREVIATIONS

ADC	Analogue to Digital Converter
ALICE	A Large Ion Collider Experiment
ATLAS	A Toroidal LHC ApparatuS
BEH	Brout-Englert-Higgs
CERN	European Organization for Nuclear Research
CMS	Compact Muon Solenoid
DAQ	Data Acquisition
ECAL	Electron Calorimeter
EM	Electromagnetic
Fermilab	Fermi National Accelerator Laboratory
HB	Hadron Barrel Calorimeter
HCAL	Hadron Calorimeter
HE	Hadron End-cap Calorimeter
HF	Hadron Forward Calorimeter
HO	Hadron Outer Calorimeter
LEIR	Low Energy Ion Ring
LEP	Large Electron-Positron Collider
LHC	Large Hadron Collider
LHCb	LHC Beauty
LHCf	LHC Forward
LINAC	Linear Accelerator
MoEDAL	Monopole and Exotics Detector at the LHC
Nb-Ti	Niobium-Titanium
PMT	Photo-multiplier Tube
PS	Proton Synchrotron
PSB	Proton Synchrotron Booster
QIE	Charge Integrator Encoder
RadDam	Radiation Damage

RBX	Read-Out Box
RF	Radio Frequency
SPS	Super Proton Synchrotron
TDC	Time to Digital Converter
TOTEM	Total Elastic and Diffractive Cross Section Measurement
TS	Time Slice

1. INTRODUCTION

Large Hadron Collider (LHC) is the world's largest and most powerful particle accelerator that is located beneath the Swiss and French border. Its design luminosity is $10^{34} cm^{-2} s^{-1}$ and the design energy is 7 TeV per particle. Physics goals of the LHC has a broad range from the discovery of the Higgs boson to search for extra dimensions and supersymmetric particles, which could make up dark matter.

Compact Muon Solenoid (CMS) is, along with A Toroidal LHC ApparatuS (ATLAS), one of the two general-purpose detectors on the LHC. The discovery of the Higgs boson has been accomplished by collaborations of CMS and ATLAS in 2012. Giant solenoid magnet, which gives the CMS its name, produces 3.8 Tesla, 100,000 times higher than the Earth's magnetic field.

CMS detector is composed of several layers of sub-detectors, one of which is Hadron Calorimeter (HCAL). Calorimeter, in general, is a device that measures energy. Hadron Calorimeter in CMS is specialized to measure energy and momentum of hadrons. Hadronic Forward (HF) or in other words Very Forward Calorimeter is a part of the HCAL and lies at high η values ($3 < |\eta| < 5$). By design, HF tries to measure high energy forward particles and jets. Thus, it is exposed to the highest radiation among all components of the HCAL.

Radiation damage caused by primary and secondary particles affects calibration and lifetime of a detector. Therefore, *in situ* radiation damage (RadDam) monitoring of detectors, which are exposed to significant amount of radiation, is vital for ensuring data quality. Accordingly, On-line RadDam Monitoring of the HF Calorimeter have been done since 2003. As part of the Phase I Upgrade of the HCAL, laser system of the HF RadDam has been renewed to get more precise measurements. The subject of this thesis is the analysis of HF RadDam data taken with the new laser system.

The following chapter introduces the Large Hadron Collider, with motivation, history, accelerator facility and details of the experiments conducted. Next chapter gives specific aspects of the CMS experiment and detector. Fourth chapter continues with HCAL, describing hadronic showers and sub-detectors. Next two chapters are about the working principle of the HF and RadDam system. The chapter after that gives the analysis and results.

2. LARGE HADRON COLLIDER

LHC is a cyclic particle accelerator and collider specialized for hadron experiments. It is located inside a 27-km circumference circular underground tunnel beneath the Swiss and French border, and its mostly composed of superconducting magnets and radio frequency (RF) cavities. The design energy of LHC operations is 7 TeV [1], seven times higher than its closest competitor Tevatron in Fermilab, which operated at 1 TeV until its shut down at 2011.

For a particle collider, a meaningful parameter is luminosity. Luminosity is, in some manner, a measure of collisions that will take place in a unit of time. The design luminosity of the LHC was $10^{34} cm^{-2} s^{-1}$ [1], which corresponds to 600 million collisions per second on average for proton-proton collisions. Yet, the LHC is not operating every second and cumulative radiation resulting from particle collisions is a more useful measure of data. Hence, the concept of integrated luminosity, a measure of total number of collisions during a time interval, is substituted with luminosity for radiation damage studies and cross section measurements.

2.1. History

LHC was proposed and accepted in 1994, as the operation of LEP was still continuing. LEP was the Large Electron-Positron storage ring and collider operated from 1989 to 2000. As the name suggests, electrons and positrons were used and maximum 209 GeV collision energy was reached by LEP.

LHC's 27-km circumference ring is inherited from LEP. Size, i.e. circumference for circular accelerators, determines the maximum energy that particles can gain. Despite using the same length storage ring, collision energy gap between LEP and LHC can be explained by the phenomenon called synchrotron radiation. LHC, unlike LEP, works with hadrons such as protons or heavy ions. Certain amount of energy is lost during acceleration of a charged particle in a circular path (Figure 2.1). Energy loss of electron is much higher compared to relatively heavier particles such as protons or any other hadrons. Hence, hadrons can be accelerated up to 35 times higher energies than leptons, even if the length of the accelerator is the same.

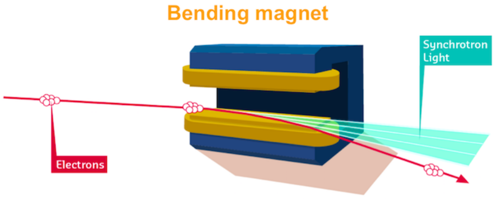

Figure 2.1. Illustration of synchrotron radiation [2].

2.2. Purpose

Particle physics tries to understand the fundamental particles and forces that make up the universe we live in. The physicists have developed a model, named the Standard Model of Particle Physics, containing all of the discovered elementary particles and their interaction. Still, the Standard Model has missing pieces.

Three of the four basic forces of the universe, which are gravity, electromagnetic, weak and strong forces, are represented with a corresponding field and a boson as mediator in the Standard Model. Physicists accomplished to unite the electromagnetic and weak forces as electroweak at very high energies, which means the mediator bosons should be identical. Nonetheless, photon, mediator of electromagnetic force, is a massless particle unlike W and Z bosons of weak force. As the hot universe got colder, a phenomenon called spontaneous symmetry breaking occurred. Thus, W and Z bosons acquired mass and the photon remained massless.

In 1964 Brout, Englert and Higgs came up with BEH mechanism in order to explain spontaneous symmetry breaking. The claim is that particles gain mass when they interact with the BEH field. The mediator of this field is called the Higgs boson. Its presence was a major prediction of the Standard Model and its discovery was one of the main goals of the LHC.

Search for supersymmetric partners of known particles, which may be an answer to dark matter and dark energy problems, understanding the matter-antimatter imbalance of observable universe and investigation of quark-gluon plasma are some of the other objectives for the construction of the LHC.

2.3. Structure

CERN accelerator complex is composed of several synchrotron accelerators and linear accelerators.

Synchrotron is a special type of circular accelerator, which uses RF cavities to accelerate, dipole magnets to keep particles on track, i.e. circular path, and quadrupole magnets to focus the beam.

In LHC, dipole magnets are composed of Niobium-Titanium (Nb-Ti) cables which become superconducting, meaning that they conduct electricity without resistance, below 10 K [3]. LHC operates at even lower temperature around 1.9 K, which is colder than outer space. Cooling of magnets is achieved by super fluid helium.

2.3.1. Accelerators

Three types of collisions take place at the detectors of LHC: proton-proton, proton-heavy ion and heavy ion - heavy ion.

For proton-proton (*pp*) collisions, procedure is as following: nucleus of hydrogen atom is stripped from its electron. Then, Linear Accelerator 2 (LINAC2) accelerates the Hydrogen nuclei, i.e. protons, up to 50 MeV and feeds into Proton Synchrotron Booster (PSB), which is a 157 m circumference synchrotron. PSB accelerates the protons up to 1.7 GeV energy and transfers them to the Proton Synchrotron (PS), which is a synchrotron as well, with 628 m circumference. When the protons reach 25 GeV energy, they are transferred to the Super Proton Synchrotron (SPS), a seven-km circumference synchrotron. SPS accelerates the beam to 450 GeV energy and injects to

LHC in both clockwise and counter clockwise directions. LHC accelerates two beams separately at the same time until they gain 6.5 GeV energy (currently).

For heavy ion runs, ionized *Pb* nuclei are accelerated in LINAC3 to the energy of 4.2 MeV per nucleus and transferred to Low Energy Ion Ring (LEIR) which is a 78 m circumference ion storage ring. LEIR accelerates the beam up to 72 MeV per nucleus and injects it to the PS. The rest of the process is similar with *pp* collisions, except for the final energy the heavy ions gain is approximately 2.56 TeV per nucleon. Figure 2.2 illustrates the CERN accelerator complex, leading up to the LHC.

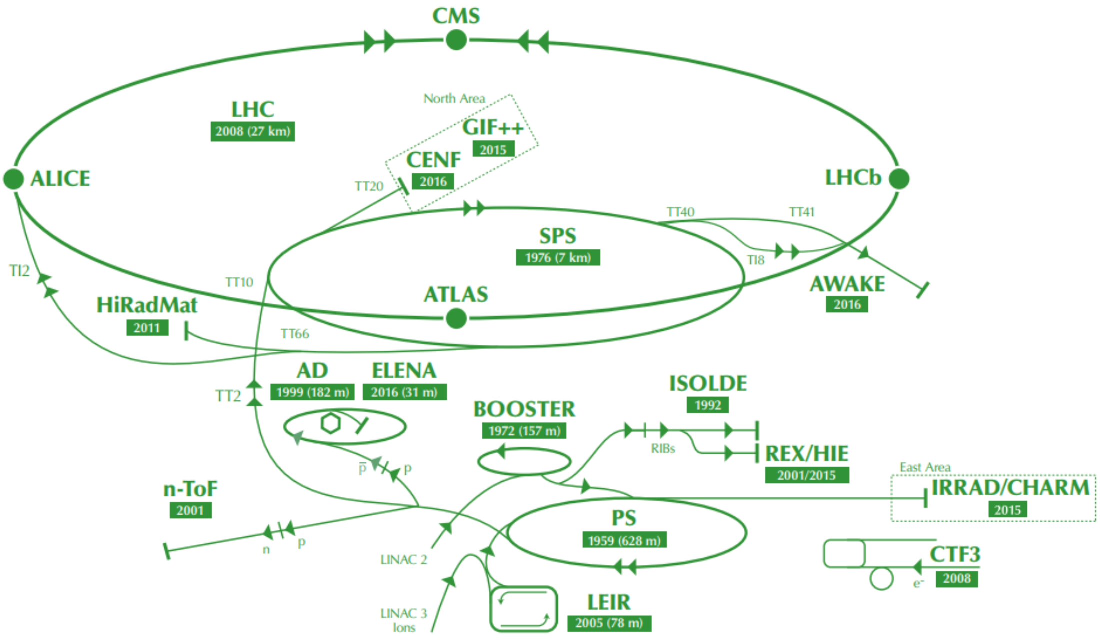

Figure 2.2. The CERN accelerator complex leading up to the LHC [3].

2.3.2. Detectors

On the LHC, four comprehensive and three small-scaled experiments are being conducted.

A Large Ion Collider Experiment (ALICE) detector is specialized for heavy ion, particularly lead-lead, collisions. The main purpose of the ALICE experiment is to study the quark-gluon plasma. Quark-gluon plasma is a state of matter where quark colour confinement is not in effect. It requires trillion degree Kelvin approximately, which was the case just microseconds after the Big Bang.

ATLAS is a general purpose detector similar to the CMS. Physics objectives of ATLAS and CMS range from the discovery of Higgs boson to the study of particle physics beyond the Standard Model. Despite having the same goals, designs of ATLAS and CMS are quite different. ATLAS uses a doughnut-shaped, i.e. toroidal, magnet system (Figure 2.3), whereas CMS has a solenoid magnet. By volume, ATLAS is the largest detector ever built.

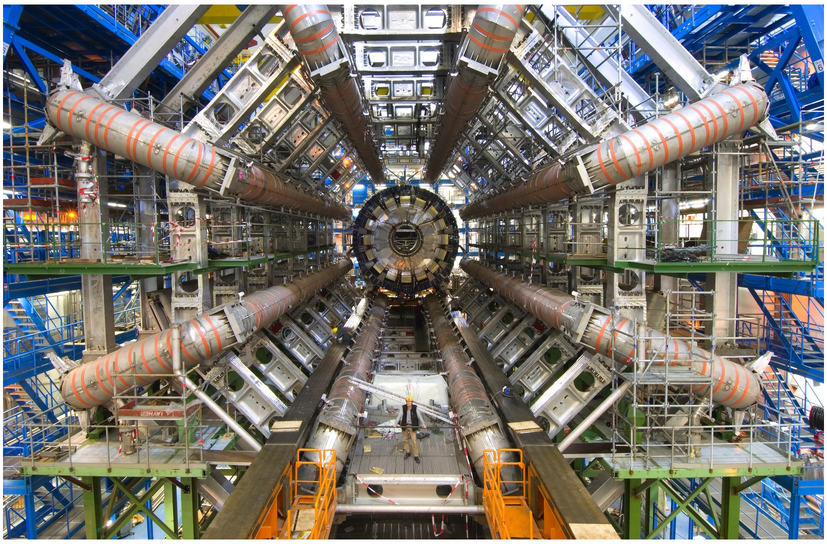

Figure 2.3. Toroidal magnet system of the ATLAS detector [4].

LHC Beauty (LHCb) experiment, on the other hand, is interested in the matter-antimatter asymmetry involving b-hadrons, the particles that contain beauty (bottom) quark.

Total Elastic and Diffractive Cross Section Measurement (TOTEM), LHC Forward (LHCf) and Monopole and Exotics Detector at the LHC (MoEDAL) are more specific and small-scale experiments running on the LHC.

3. COMPACT MUON SOLENOID DETECTOR

Compact Muon Solenoid experiment is one of the most comprehensive experiments in LHC. Aim of the experiment ranges from the discovery of the Higgs Boson to search for extra dimensions and particles. The total weight of the detector is 14,000 tonnes, and it is shaped roughly like a cylinder of 15 m diameter and 28.7 m length.

The name Compact Muon Solenoid comes from the giant solenoid magnet which produces 3.8 Tesla, and it is the most powerful solenoid in the world.

3.1. Structure

The CMS detector is composed of several layers of sub-detectors, each one is specialized for a different task for identifying the trajectory, charge, momentum and energy of secondary particles produced in collisions (Figure 3.1).

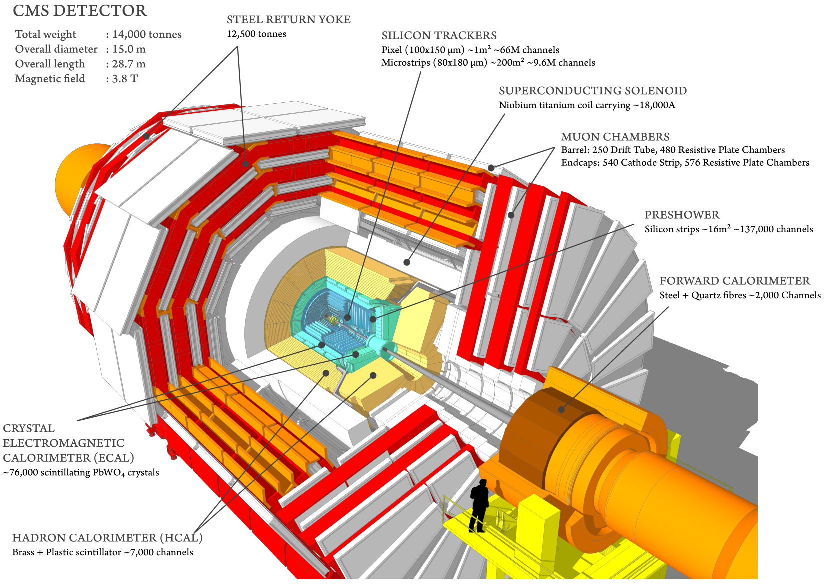

Figure 3.1. Structure of the Compact Muon Solenoid detector [5].

3.1.1. Silicon Tracker

Silicon Tracker is at the core of the CMS, closest to where the collisions take place, and it is exposed to the highest particle radiation among all of the components. In order to reduce the radiation damage, the tracker is kept at -20^{o}C. Trajectories of the charged particles are tracked by the Silicon Tracker accurately, since short-lived rare particles like τ^{-} decay immediately and do not reach the other parts of the CMS detector.

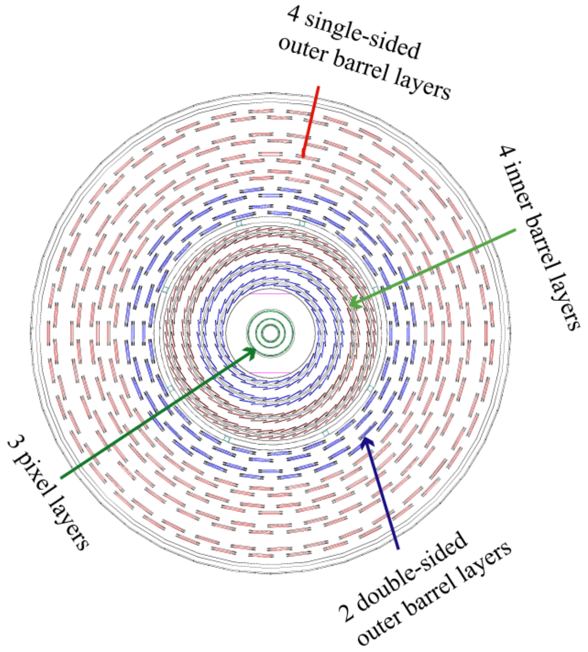

Figure 3.2. Layers of Silicon Tracker [6].

Silicon Tracker is composed of pixels and silicon microstrips (Figure 3.2). Charged particles create electron-hole pairs by ejecting electrons from silicon atoms when passing through a pixel or strip. An electronic chip is attached to each pixel and amplifies the signal. Silicon strip and pixels provide information to be used to reconstruct trajectories of secondary particles.

3.1.2. Electromagnetic Calorimeter

Electromagnetic calorimeter (ECAL) is designed to capture and measure the energy of electrons, positrons and photons. In order to understand the working mechanism of ECAL, interaction of these particles with matter should be discussed.

Above 100 MeV, electrons and positrons lose energy by Bremsstrahlung and photons by pair production for the most part. Bremsstrahlung is energy loss by acceleration or deceleration, primarily based on passing by atomic nuclei, which is similar to the synchrotron radiation discussed in Section 2.1. As a result of Bremsstrahlung, new photons are emerged. Pair production gives birth to new electrons and positrons. Therefore, a single electron (or positron) in a medium can start a domino effect and lead to the creation of many more electrons, positrons and photons. This phenomenon is called electromagnetic (EM) shower. Pair production is stopped after photons' energy falls below the critical level, called pair production threshold, which is approximately equal to two times the rest mass of an electron ($\sim$ 1 MeV). Then, the number of particles in the EM shower decays exponentially.

Lead tungstate crystals ($PbWO_4$) are used in the CMS ECAL, which produce scintillation in small EM showers. Scintillation means the material emits light when its atoms de-excite after they are excited by high energy particles passing through. Amount of light produced in scintillation depends on the energy of the incident particle. Thus, ECAL can measure the energy of the particles indirectly.

ECAL lies between Silicon Tracker and HCAL in CMS detector. HCAL is based on a similar principle with ECAL but it relies on nuclear reactions and it is optimized for hadrons. The operation and details of the HCAL will be explained in Chapter 4.

3.1.3. Solenoid Magnet

The motivation behind the solenoid magnet is to bend the trajectories of secondary particles in order to determine their charge and momentum. Positively and negatively charged particles are deflected to opposite directions when a perpendicular magnetic field to their direction of motion is applied. High-momentum particles are bent less than those with low-momentum.

CMS uses a very powerful solenoid magnet which produces 3.8 Tesla, $100,000$ times greater than Earth's magnetic field. The magnet uses coils of superconducting wires which operate at $-268.5^{o}C$ (4.5 K).

3.1.4. Muon Chambers

Muons and neutrinos, unlike other particles, can pass through all parts of the CMS detector (Silicon Tracker, Calorimeters and Solenoid Magnet) without any interaction. Therefore, muon chambers are built at the outermost layer of the CMS detector, outside of the solenoid magnet.

Muon chambers are made up with layers of drift tubes and iron return yokes in between them. Working mechanism of drift tube is similar to the ionization chamber. When a charged particle passes through the gas inside the drift tube, it creates ion-electron pairs and electrons are drifted to positively charged wires. Then, using electrical signal coming from multiple drift tubes, trajectory of charged particles can be determined.

Magnetic field in the iron return yokes bend the trajectory of muons, helping us to determine the momentum of muons.

3.2. Geometry

3.2.1. Rapidity and Pseudorapidity

In a collider like LHC, it is common that two opposite beams travelling in z-axis (beam line) are not equal in momentum. In such cases, the centre of mass frame of the colliding beams is not the same as the lab frame. Then, a quantity which is invariant under Lorentz boost (transformation) along z-axis is needed. This quantity is defined as

$$y \equiv \frac{1}{2}\ln(\frac{E+P_zc}{E-P_zc}) = \tanh^{-1}(\frac{P_zc}{E}) \tag{3.1}$$

and called rapidity, where E is the total energy of the particle, P_z is the momentum along z-axis and c is the speed of light. Nonetheless, rapidity is not easy to determine. An approximation for highly relativistic particles ($Pc >> mc^2$) leads us to a new quantity pseudorapidity, which is defined as follows:

$$\eta \equiv -\ln(\tan\frac{\theta}{2}) \tag{3.2}$$

where θ is the angle between the positive beam axis and the particle's momentum vector. For highly relativistic particles $\eta \approx y$.

3.2.2. Azimuthal Angle

Azimuthal angle is one of the axis of the spherical coordinate system, and shown as ϕ. In the CMS detector, sectors of sub-detectors are labelled according to η and ϕ coordinates.

4. THE HADRON CALORIMETER

4.1. Purpose

Aim of the HCAL is to measure the energy of hadrons, using hadronic showers. Hadron is a general term for baryons and mesons.

Hadronic showers are similar to the EM showers, which are discussed in Section 3.1.2. EM showers take place under electromagnetic interactions of electrons, positrons and photons. Hadronic shower can be described as the cascade of secondary particles resulting from strong interaction of hadrons with the matter they are passing through.

Hadron calorimeter is, in general, made of dense matter and scintillating (or quartz) material inside them. The dense matter is to initiate and absorb hadronic shower and scintillating material is to detect and transfer the signal generated by secondary particles.

4.2. Structure

HCAL is composed of several parts, each serving a different purpose.

4.2.1. Hadron Barrel

Hadron Barrel (HB) is a cylindrically symmetric, barrel-shaped section of the HCAL (Figure 4.1) which lies in between the ECAL and the solenoid magnet. HB is composed of alternating layers of brass and plastic scintillator plates and covers the pseudorapidity range $-1.3 < \eta < 1.3$. Total of 36 identical wedges, each covering 20^o azimuthal angle, form two parts HB+ and HB−. The brass absorber is composed of 70% Cu and 30% Zn [7].

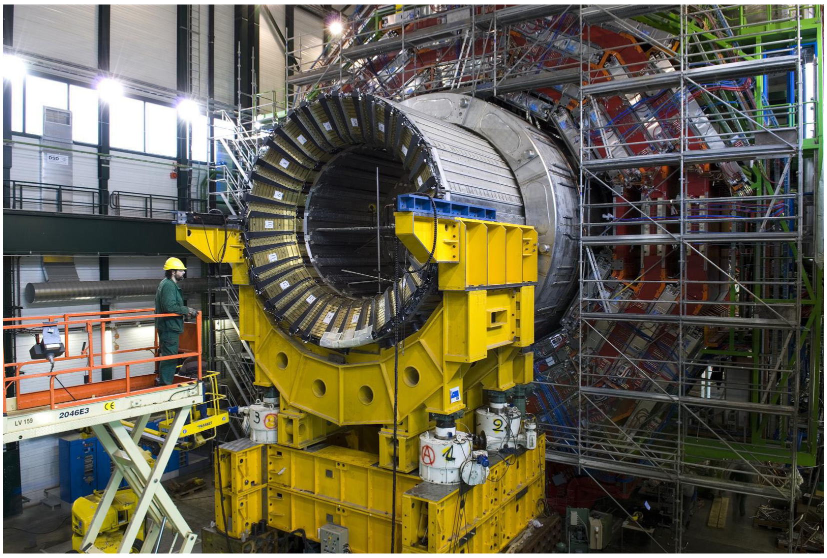

Figure 4.1. Hadron Barrel calorimeter [8].

4.2.2. Hadron Endcap

The name of Hadron Endcap Calorimeter (HE) comes from its cap-like position and coverage with respect to the HB. HE is composed of 18 wedges for each part, HE+ and HE−. They cover the pseudorapidity range $1.3 < |\eta| < 3$. The composition of the Hadron Endcap is the same as the HB.

4.2.3. Hadron Outer

Hadron Outer Calorimeter (HO), as the name suggests, is placed outside of the solenoid magnet. It covers the pseudorapidity range $-1.3 < \eta < 1.3$, same as the HB. The purpose is to detect hadronic showers that pass beyond the HB and magnet. Design of the HO is similar to the muon barrel system of which it is inside.

5. THE HADRON FORWARD CALORIMETER

5.1. Purpose

Very forward calorimeter, known as the Hadron Forward, is designed to detect particles and jets that are in the very forward region with high $|\eta|$ values. The HF calorimeter provides crucial information about missing transverse energy in each collision event. Therefore, the HF detectors are placed at the very ends of the CMS detector (Figure 5.1), which correspond to $3 < |\eta| < 5$, aligned with the beam line. The HF consists of two modules, which are HF+ at $\eta > 0$ and HF− at $\eta < 0$.

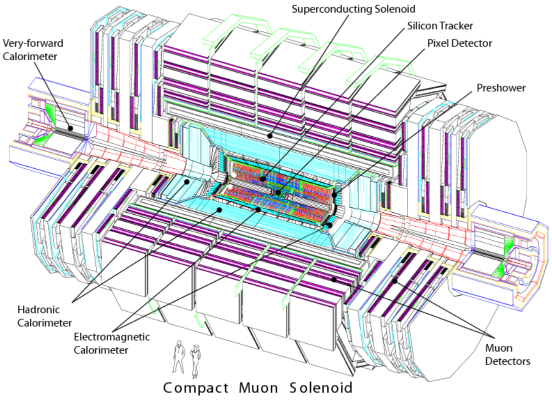

Figure 5.1. In the drawing of the CMS detector, the HF modules are referred as Very-forward Calorimeter [9].

5.2. Structure

Hadron Forward Calorimeters are made of cylindrical iron blocks and embedded with thin quartz fibres. Each HF unit is divided into 18 triangle-shaped slices called wedges (Figure 5.2), that correspond to 20-degree azimuthal angle ϕ.

Furthermore, the wedges are subdivided into 24 sections, namely towers, according to their pseudorapidity values. 22 of them cover 10-degree azimuthal angle, while the remaining two towers that have the largest pseudorapidity values ($|\eta| > 4.7$) cover

Figure 5.2. HF wedges with quartz fibres.

20-degree azimuthal angle. Since increase in the pseudorapidity value means getting closer to the beam line, the size of the towers becomes smaller (Figure 5.3).

In addition, calorimeter is segmented longitudinally by using short and long fibres (Figure 5.4), to distinguish between the hadronic and electromagnetic showers [11]. Two types of fibres are read out separately.

The same type quartz fibres inside a tower are connected to the same photomultiplier tube (PMT). 24 PMTs of a wedge are housed in an read-out box (RBX) with electronic modules. Hence, one RBX is responsible for one half of the wedge, which covers 10-degree azimuthal angle.

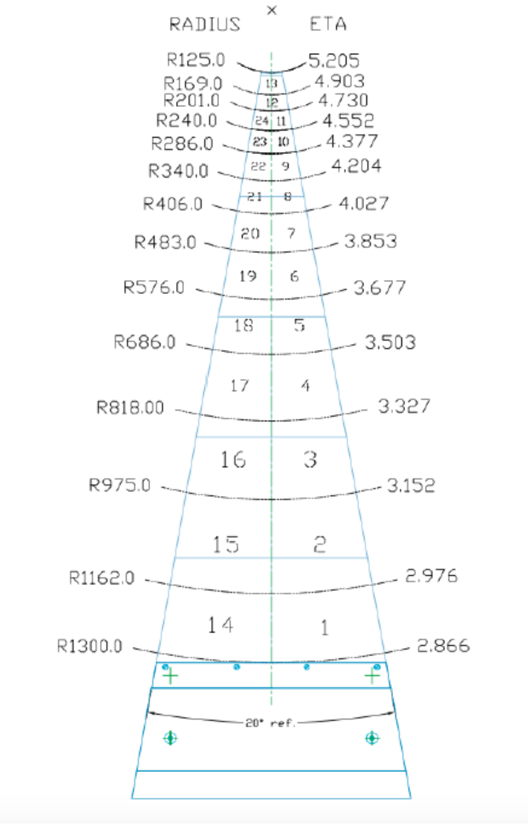

Figure 5.3. HF wedge is divided into 24 towers with different $\Delta\eta \times \Delta\phi$ values [10].

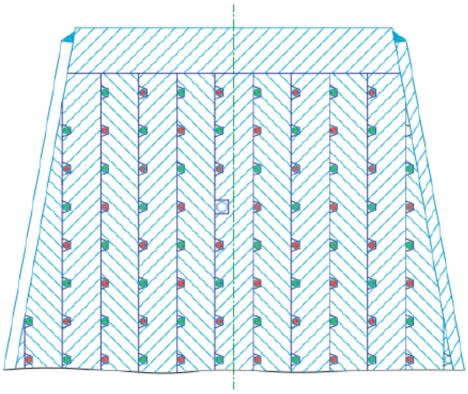

Figure 5.4. HF tower 13, long (*red*) and short (*green*) fibres [10].

5.3. Operation

5.3.1. Iron Absorber

The function of iron absorber, is to create showers, as mentioned in Chapter 4.

In order to understand the motivation behind the longitudinal segmentation of HF towers, a brief explanation is necessary. Although HF is specialized for hadron shower detection, both electromagnetic and hadronic showers occur in the HF. Fortunately, EM showers start at the beginning of the HF iron absorber, unlike the hadrons that are gradually absorbed and produce showers at deeper levels. Hence, the long fibres collect signals from both EM and hadronic showers. The short fibres start from 22 cm deep in the HF units. Therefore, only the signals from the hadronic showers appear on the short fibres.

5.3.2. Cherenkov Radiation

When a high energy charged particle passes through a dielectric medium, if speed of the particle is greater than the speed of light in that medium, an electromagnetic radiation, called Cherenkov radiation, is produced. The basic principle of signal generation in the HF quartz fibres can be summarized as Cherenkov radiation caused by hadronic and EM showers. Generated light travels through the quartz fibres and light guides to be conveyed to the PMTs.

5.3.3. Photomultiplier Tube

Photomultiplier tubes are essentially made of an anode, a cathode and a number of dynodes (Figure 5.5). Incoming light falls on the cathode window that emits an electron by photoelectric effect. Then, the emitted electron is accelerated by the potential difference between the cathode and the first dynode. When this electron hits the dynode, multiple electrons are emitted from the dynode, then these electrons repeat the process between the first and second dynode. Multiplication of electrons continue between the dynodes until all of them reach the anode. Multiplication factor depends on the overall potential difference between the anode and the cathode. In short, PMTs are used for amplification of weak Cherenkov signals generated in the quartz fibres.

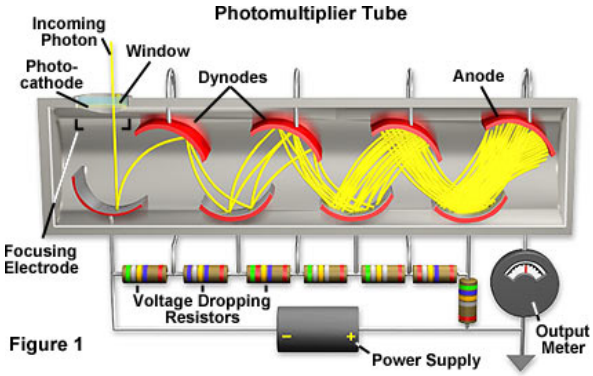

Figure 5.5. Working scheme of a photomultiplier tube [12].

Although the detectors are well covered from outside light, stray muons in the vicinity of the PMTs can produce false signals when they hit a PMT window. 4-anode PMTs are installed in Phase I Upgrade of the HF detector to solve this problem. Stray muons are localized on single anode in 4-anode PMTs, whereas the Cherenkov light from real event illuminates all of them. Hence, 4-anode PMTs help us to distinguish real signals from the signals produced by stray muons.

5.3.4. Read-Out Box and Charge Encoder Integrator

Analogue signal generated by PMT is transmitted to charge encoder integrator, i.e. QIE. QIE is an electronic chip which digitizes the analogue signal. Though the single anode PMTs are replaced with the 4-anode ones, the Data Acquisition (DAQ) System could not be renewed accordingly. In 2016, as part of the HF Phase I Upgrade, QIE10 chips are installed in the new front-end electronic cards and these cards are tested [13]. The new front-end electronic cards allow us to process the 4-anode PMT signals as 2-anode ones.

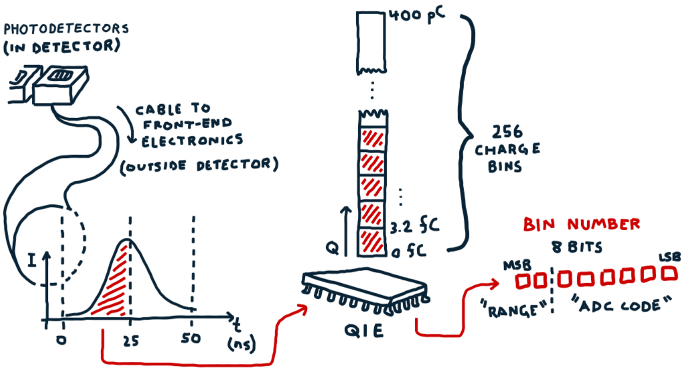

Figure 5.6. Analogue-to-Digital converter [14].

QIE chips integrate the signal over 25 ns time intervals and save as 8-bit values as analogue-to-digital (ADC) count (Figure 5.6). An ADC count corresponds to a charge value in units of fC. Table 5.1 demonstrates the conversion of ADC counts into charge values. The 25 ns interval for data taking is called a time slice (TS).

New QIE chips, e.g. QIE10, also include a time-to-digital converter (TDC). A timer is started when the signal passes a predefined threshold and counts to the end of the time slice. The value is saved in 6-bit registers and called TDC count (Figure 5.7). Hence, TDC counts are between 0 and 63. Single PMT provides 2 ADC and 2 TDC counts in a TS.

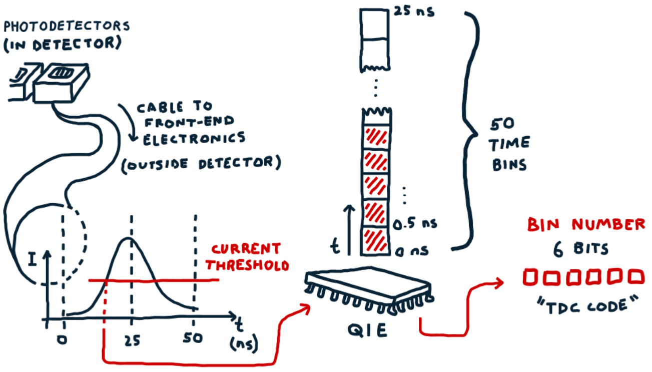

Figure 5.7. Time-to-digital converter [14].

Table 5.1. Ideal QIE10 response mapping of input charge to output code [15].

Range	**Input Charge**	**ADC (Mantissa)**	**Sensitivity (Q/bin)**
0	-16 fC - 34 fC	0-15	3.1 fC/bin
0	34 fC - 158 fC	16-35	6.2 fC/bin
0	158 fC - 419 fC	36-56	12.4 fC/bin
0	419 fC - 592 fC	57-63	28.8 fC/bin
1	517 fC - 915 fC	0-15	28.8 fC/bin
1	915 fC - 1910 fC	16-35	49.6 fC/bin
1	1910 fC - 3990 fC	36-56	99.2 fC/bin
1	3990 fC - 5380 fC	57-63	198.4 fC/bin
2	4780 fC - 7960 fC	0-15	198.4 fC/bin
2	7960 fC - 15.9 pC	16-35	396.8 fC/bin
2	15.9 pC - 32.6 pC	36-56	793.6 fC/bin
2	32.6 pC - 43.7 pC	57-63	1587 fC/bin
3	38.9 pC - 64.3 pC	0-15	1587 fC/bin
3	64.3 pC - 128 pC	16-35	3174 fC/bin
3	128 pC - 261 pC	36-56	6349 fC/bin
3	261 pC - 350 pC	57-63	12.70 pC/bin

In conclusion, high energy particles produce Cherenkov radiation in the fibres. Then the light coming from the Cherenkov radiation falls on the PMTs. Signals produced by the PMTs are transmitted to the RBXs to be processed. The digitized signal in the form of ADC and TDC counts, are stored in the registers for later use. Collision or RadDam data analyses are done using the stored data.

6. RADIATION DAMAGE MEASUREMENT

6.1. Motivation

As placed in high $|\eta|$ values, the HF calorimeters are exposed to high energy particles more than the other parts of the HCAL detector. For this reason, the HF needs to be carefully monitored for the radiation damage.

Radiation resulting from high energy particles leads to a decrease in transparency of the HF quartz fibres. It affects the calibration of the calorimeter and the calorimeter will eventually cease to operate. Thus, observation of the change in transparency, or determining the rate of darkening, of the HF quartz fibres with respect to the accumulated dose of radiation is crucial. RadDam measurement allows us to monitor the change in the calibration and estimate the life time of the detector.

6.2. RadDam Device

In order to measure the radiation damage of the HF *in situ*, a device with a laser system was proposed and installed in 2003 [16]. Four wedges are selected in both HF+ and HF− detectors, in each wedge seven towers, 56 in total, are equipped with RadDam fibres.

Figure 6.1 illustrates the mapping for ϕ angles of the HF towers to iPhi values. In addition, every η ring is mapped to an iEta value. In each η ring, four towers are selected for RadDam. HF RadDam channel list can be found in Table 6.1, minus η values indicates HF−.

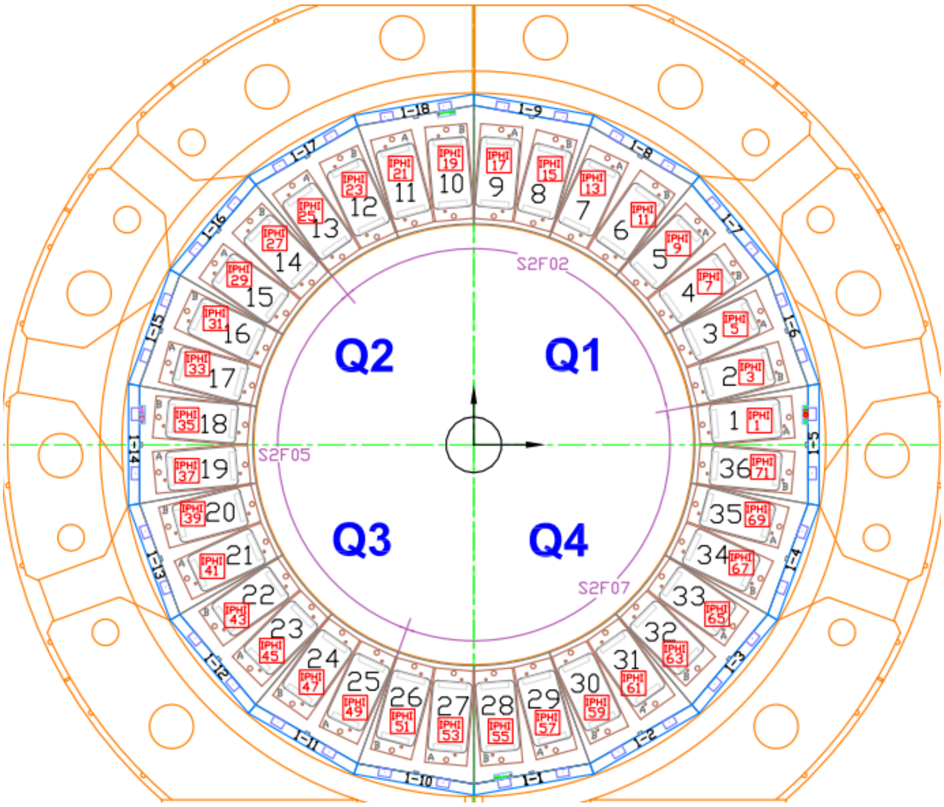

Figure 6.1. HF mapping (indicated with red boxes) [17].

Table 6.1. List of 56 HF channels that are equipped with RadDam fibres.

HF+	**iEta**	**iPhi**
	30	1,21,37,57
	32	1,21,37,57
	34	1,21,37,57
	36	1,21,37,57
	38	1,21,37,57
	40	19,35,55,71
	41	19,35,55,71

HF−	**iEta**	**iPhi**
	-30	15,35,51,71
	-32	15,35,51,71
	-34	15,35,51,71
	-36	15,35,51,71
	-38	15,35,51,71
	-40	15,35,51,71
	-41	15,35,51,71

Every RadDam fibre is connected to a different PMT. To label and differentiate fibres on HF, η and ϕ values are used as the coordinate system. Though, depth is usually used to pinpoint the various lengths of fibres, e.g. S (short) and L (long), only L fibres are installed for HF RadDam. In addition, two channels of data are taken from a single 4-anode PMT in a laser pulse as explained in Section 5.3.4. Hence, depth coordinate indicates the two pairs of anodes of a PMT in RadDam measurements.

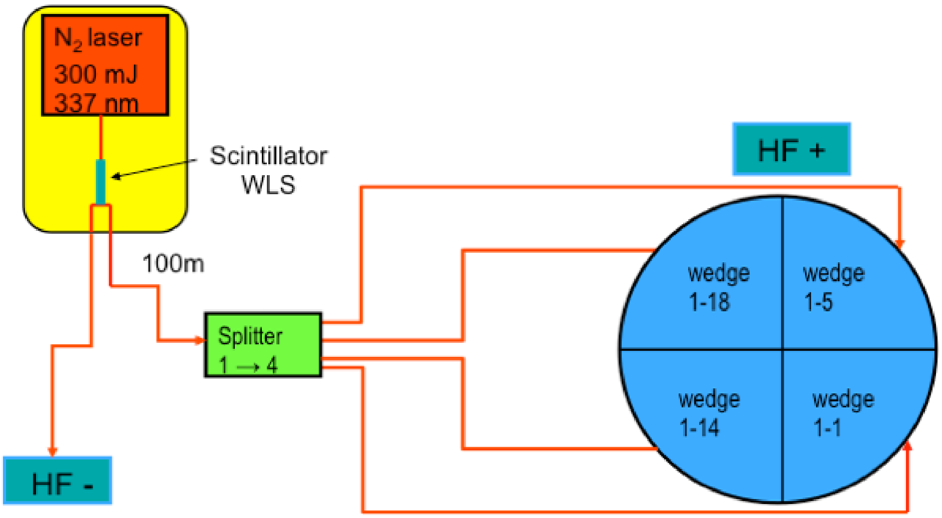

Figure 6.2. RadDam laser system [18].

Working principle of RadDam device can be summarized as the following:

(i) Laser is fired and split in half, one for HF+ and one for HF−.
(ii) The light is split and sent to four wedges of both HF+ and HF− (Figure 6.2).
(iii) Then, the light is transmitted to RadDam fibres with two ends polished for a better reflection (Figure 6.3).
(iv) First reflected light at the front end of the RadDam fibre is read by PMT and labelled as S_1 in our analysis.
(v) The remaining light that have passed through the front end travels to the far end and is reflected by the polished surface. This signal arrives 25 ns later to the PMT after the S_1, and is called S_2 [1] .

---

[1] Ideally, 50% of the incoming signal should pass through the fibre and 50% should be reflected at the front end. Nonetheless, it is a though configuration to achieve physically. Hence, ratio of S_2 and S_1 may be greater than one.

(vi) The ratio of S_2 and S_1 gives a measure for the transparency of the fibre.

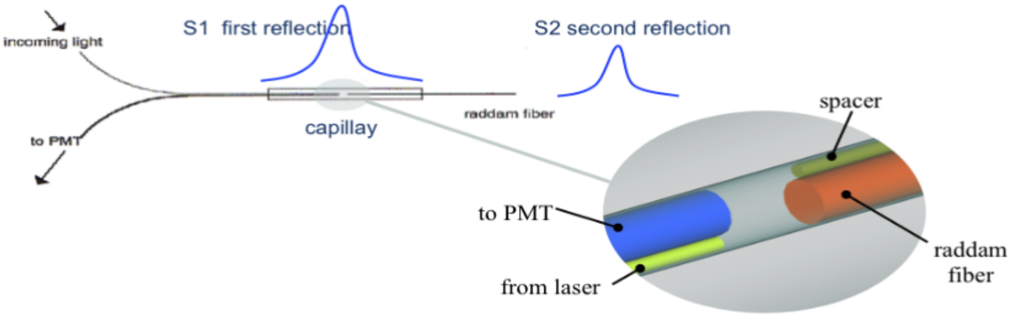

Figure 6.3. Working scheme of HF RadDam monitoring.

6.3. Radiation Damage Recovery

A slight recovery occurs after a while from the irradiation once the radiation goes off. Thus, the ratio $R = S_2/S_1$ depends on both accumulated dose D and the post irradiation time t. Behaviour of the quartz fibres due to radiation damage during the time interval between calibration and data taking is important to get a valid calibration.

Radiation hardness of quartz fibres are measured using 500 MeV electrons up to 50 Mrad [19] and 24 GeV protons up to 1.25 Grad [20]. For a comparison, 1.25 Grad radiation is approximately equals to 12 years of HF operation in LHC. Below 0.6 Grad, high attenuation is observed when the signal is in the range of 550 to 680 nm or lower than 380 nm. Attenuation is minimal and the damage recovery is maximum in between 400 to 520 nm. In addition, the latter experiment with protons demonstrated that there is no recovery after 0.6 Grad for the high attenuation ranges.

PMTs in HF calorimeter which detects Cherenkov light, are sensitive in the range from 400 to 500 nm light, where the damage recovery is maximum. Therefore, 450 nm light is used by RadDam lasers.

6.4. Upgrade

From the first proposal in 2003 to 2018, RadDam device tests and measurements were done with the HCAL Laser System. HCAL Laser was generating wide pulses, so S_1 and S_2 were distributed over three time slices, which makes it hard to analyse. New light source that is specialized for HF RadDam is proposed in Phase I Upgrade of the HF calorimeter [21]. Our aim is to analyse the data coming from this new system.

New light source (or laser system) offers a narrower and sharper signal. With new light source, the intention is to see S_1 and S_2 on the separate but consecutive time slices, specifically on TS_2 and TS_3. In order to adjust incoming S_1 and reflected S_2 signals to be measured in second and third time slices, one has to select the phase carefully. Phase, or delay time, is the time between trigger and laser pulse and can be adjusted using 5 ns steps.

Ideally, HF RadDam runs should be taken daily, in order to clearly see the radiation damage and recovery. An event means a laser fire and corresponds to a single data set including ADC and TDC values of 10 TS, event ID and coordinate of the channel, e.g. iEta, iPhi and iDepth. Channels are represented as (iEta, iPhi) or (iEta, iPhi, iDepth) in the analysis. With new laser system, 35000 events are taken per run, seven different delay times are covered by 5000 events for each.

7. ANALYSIS

7.1. Run List

35 runs were taken with the new light source from August 19 to December 2, 2018. Table 7.1 lists the runs on which our analysis is based.

Table 7.1. List of runs taken with the new light source.

#	Run Number	Date	#	Run Number	Date
1	321466	19.08.18	19	326588	12.11.18
2	321585	21.08.18	20	326642	13.11.18
3	322258	05.09.18	21	326699	14.11.18
4	322417	07.09.18	22	326723	15.11.18
5	322851	17.09.18	23	326795	16.11.18
6	323569	26.09.18	24	326863	18.11.18
7	323739	30.09.18	25	327084	22.11.18
8	323764	30.09.18	26	327153	23.11.18
9	324137	05.10.18	27	327199	24.11.18
10	324223	07.10.18	28	327226	25.11.18
11	324596	14.10.18	29	327279	26.11.18
12	324709	15.10.18	30	327347	27.11.18
13	325262	25.10.18	31	327409	28.11.18
14	325455	29.10.18	32	327449	28.11.18
15	325545	31.10.18	33	327497	30.11.18
16	326342	09.11.18	34	327528	01.12.18
17	326406	09.11.18	35	327567	02.12.18
18	326556	11.11.18			

7.2. Delay Time Settings

The first step of the analysis is the selection of correct delay time slots. In order to achieve this goal, the function

$$\frac{Q_1 + Q_2}{Q_t} \tag{7.1}$$

must be maximized. Q_1 is the total charge in TS_2, and Q_2 is in TS_3. Q_t indicates the total charge in all time slices in a single event. Charge in a TS is evaluated using Table 5.1 and ADC counts provided by QIE, which is explained in Section 5.3.4 in detail.

Thus, $\frac{Q_1 + Q_2}{Q_t}$ vs Event Number graphs are plotted for all 56 fibres[2] .

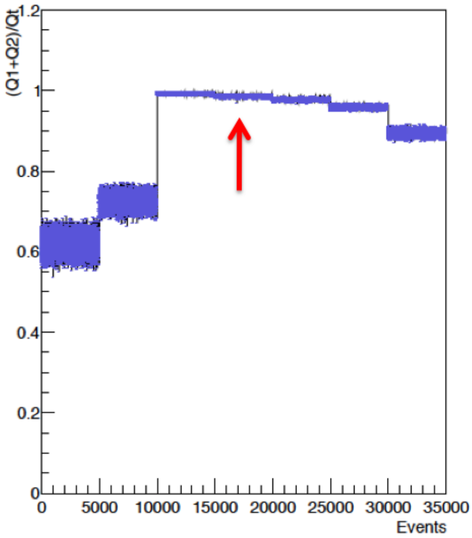

Figure 7.1. $\frac{Q_1 + Q_2}{Q_t}$ vs event number graph for channel (32, 21). X-axis shows the event number, Y-axis shows $\frac{Q_1 + Q_2}{Q_t}$ value, red arrow indicates the selected group of events.

---

[2] Each fibre has a corresponding (unique) PMT. As explained in Chapter 5.3.4, there are two ADC and TDC channels coming from a PMT. Average values of 2 channel data are used as ADC and TDC counts. Nonetheless, significantly different TDC values from a fibre is a cause to discard the data for a given event. From this point on, the terms fibre and channel will be used interchangeably.

A plateau-like region is observed on the graphs (Figure 7.1). The middle part of the plateau region is selected in order to be safe.

Tables 7.2 and 7.3 illustrate the selected delay time slots for channels on HF+ and HF− calorimeters. Table 7.4 illustrates corresponding delay time slot for event numbers.

Table 7.2. List of the HF+ channels delay time selections.

iEta	**iPhi**	**Delay Time Slots**	**iEta**	**iPhi**	**Delay Time Slots**
30	1	4	36	37	5
30	21	4	36	57	5
30	37	4	38	1	5
30	57	4	38	21	5
32	1	4	38	37	5
32	21	4	38	57	5
32	37	5	40	19	5
32	57	4	40	35	5
34	1	4	40	55	5
34	21	5	40	71	5
34	37	5	41	19	5
34	57	4	41	35	5
36	1	5	41	55	5
36	21	4	41	71	3

Table 7.3. List of the HF− channels delay time selections.

iEta	**iPhi**	**Delay Time Slots**	**iEta**	**iPhi**	**Delay Time Slots**
−30	15	4	−36	51	4
−30	35	4	−36	71	3
−30	51	4	−38	15	5
−30	71	3	−38	35	5
−32	15	4	−38	51	5
−32	35	5	−38	71	3
−32	51	5	−40	15	5
−32	71	3	−40	35	5
−34	15	5	−40	51	5
−34	35	5	−40	71	3
−34	51	5	−41	15	5
−34	71	3	−41	35	5
−36	15	4	−41	51	5
−36	35	5	−41	71	5

Table 7.4. Event number vs delay time slots.

Event Number	**Delay Time Slot**
0-4999	1
5000-9999	2
10000-14999	3
15000-19999	4
20000-24999	5
25000-29999	6
30000-34999	7

7.3. Pedestals

Pedestal is the value that is measured even if there is no signal and can be perceived as noise of the system. Average of total charges on TS_0 and TS_1 is used as pedestal.

As it can be seen in Figure 7.2, variation of pedestal for a channel during the full period of data taking, i.e. from August 19 to December 2, is below 1 fC. Considering the fact that the actual signal has 10^3 fC, three orders of magnitude higher, variation in pedestals are negligible for our analysis.

In order to compare the pedestal values between the channels, normalized pedestals are plotted on the same graph. Normalization is achieved via taking the time average of the pedestal for a channel and dividing all values to this average. Therefore, each channel has its own normalization constant. Figure 7.3 illustrates that normalized pedestal variation is small.

Since pedestals are stable enough to perform the analysis, Q_p (pedestal) is subtracted from both Q_1 and Q_2 event by event. From this point on, term Q_1 and Q_2 will actually refer to $Q_1 - Q_p$ and $Q_2 - Q_p$ values, respectively.

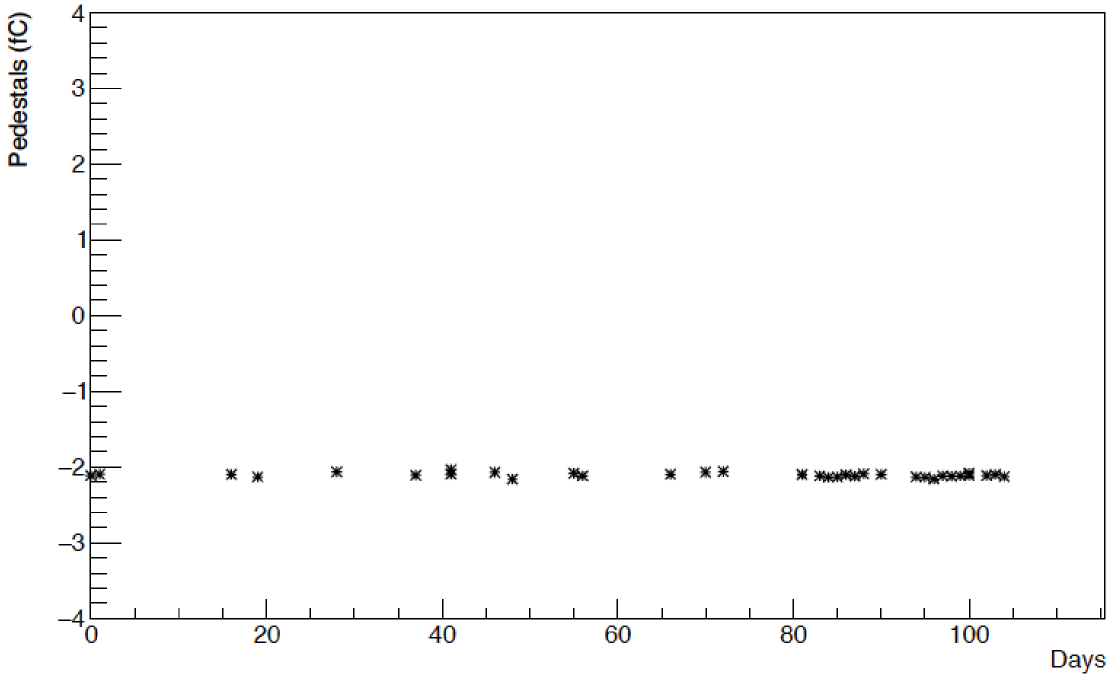

Figure 7.2. Pedestal values for channel (30 1 2) vs time.

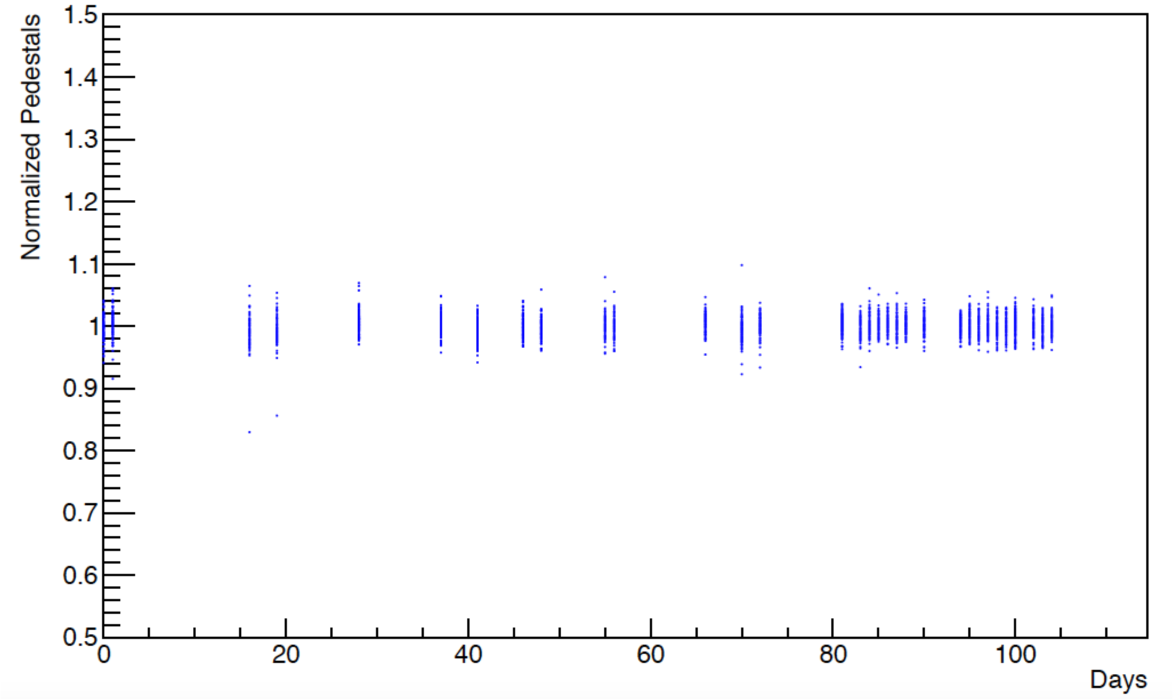

Figure 7.3. Normalized pedestals of all channels.

7.4. Cuts

As explained in Section 5.3.4, 4-anode information is available for a PMT. Nonetheless, our electronic system can process them in two channels. Thus, two channel information comes from a PMT for both ADC and TDC. It is expected that values of two ADC (or TDC) channels in a PMT to be the same or close. In order to check if data are valid, scatter plots are examined for TDC channels. As can be seen in Figures 7.4 and 7.5, points are localized around the value 10 with a little tail in accordance with the expectations.

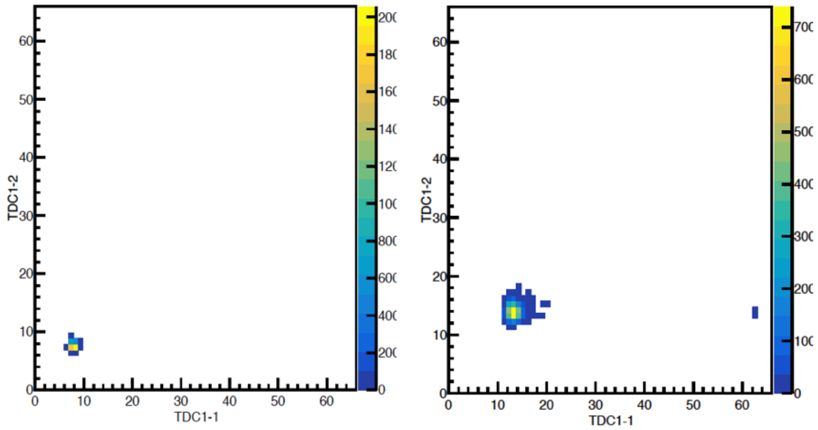

Figure 7.4. Scatter plots of TDC channels in (−36 15) and (30 1) belonging to time slice 2 in run 321466.

For ADC channels, scatter plots (Figures 7.6 and 7.7) are obtained after conversion to charge values using Table 5.1.

In short, the following plots are analysed for each channel of a PMT:

- Scatter Plot of TS_2 TDC Channels
- Scatter Plot of TS_3 TDC Channels
- Scatter Plot of TS_2 ADC Channels
- Scatter Plot of TS_3 ADC Channels

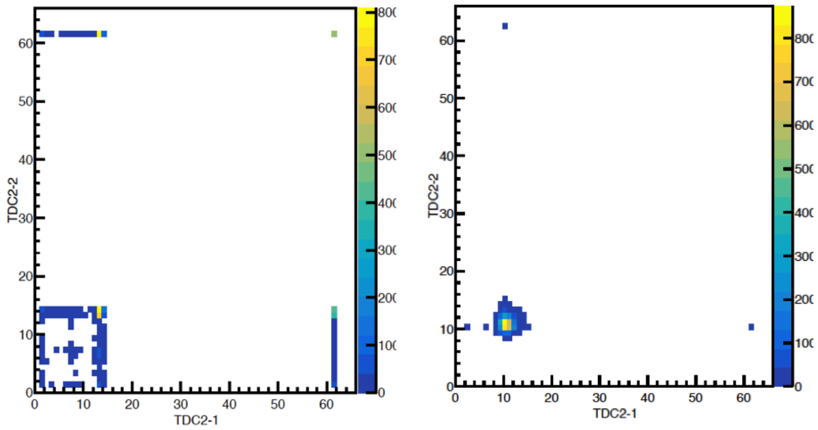

Figure 7.5. Scatter plots of TDC channels in (−38 15) and (32 1) belonging to time slice 3 in run 321466.

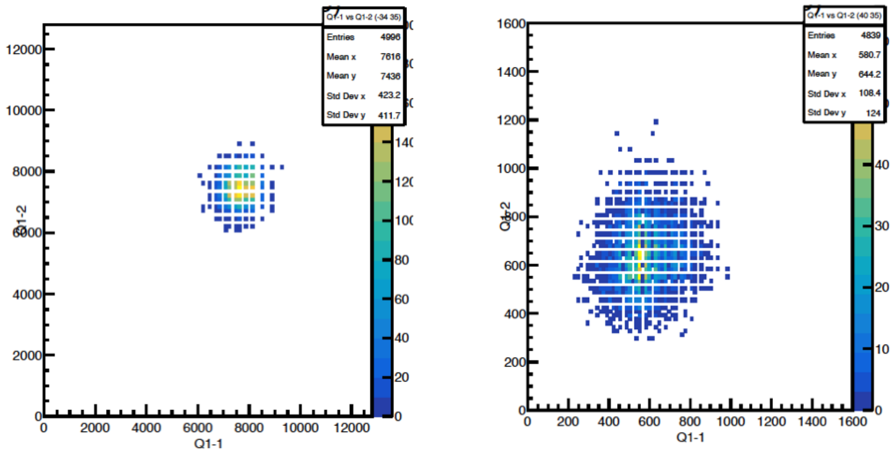

Figure 7.6. Scatter plot of ADC channels in (−34 35) and (40 35) belonging to time slice 2 in run 321466.

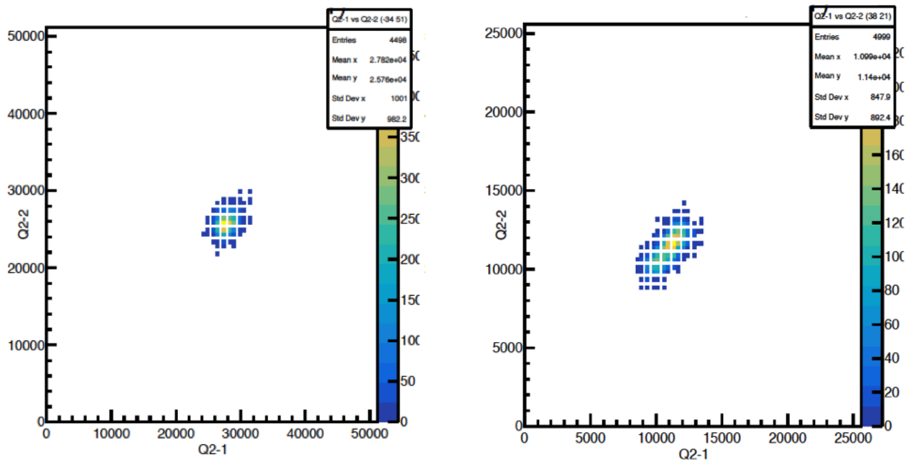

Figure 7.7. Scatter plot of ADC channels in (−34 51) and (38 1) belonging to time slice 3 in run 321466.

7.4.1. TDC Cuts

Not all scatter plots of TDC channels are well localized. Additional cuts for these scattered values of TDC channels are added. Figure 7.8 shows an example of a TDC cut for channel (32 37). By adding cuts, we eliminate the noisy events, which may cause problems in the analysis.

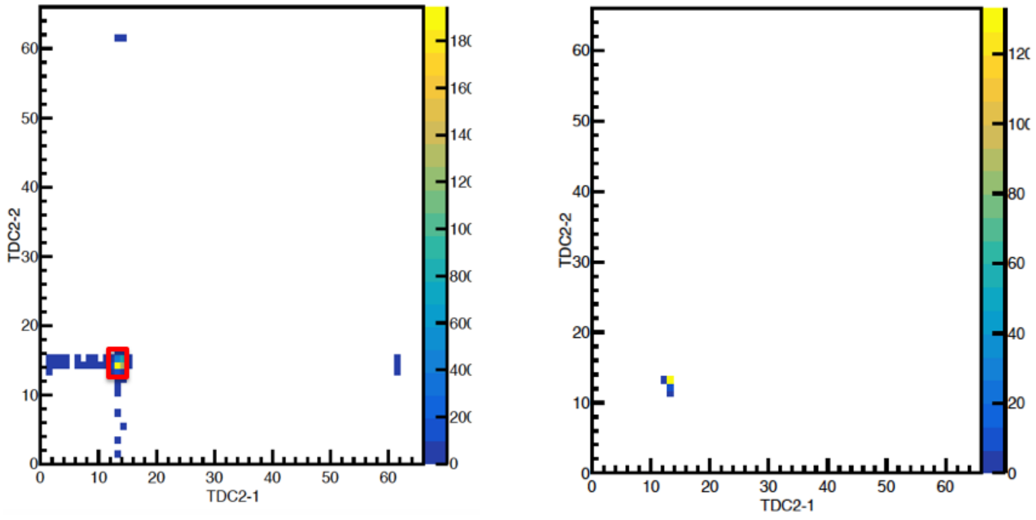

Figure 7.8. Scatter plots of TS_3 TDC counts in channel (32 37), before and after the cuts.

7.4.2. Charge Cuts

A few charge values, which are close to zero, are observed in the later runs for some ADC channels (Figure 7.9). Since the order of magnitude for charge is $\sim 10^3$ fC, cut for $Q < 10fC$ is added to keep these noisy signals out.

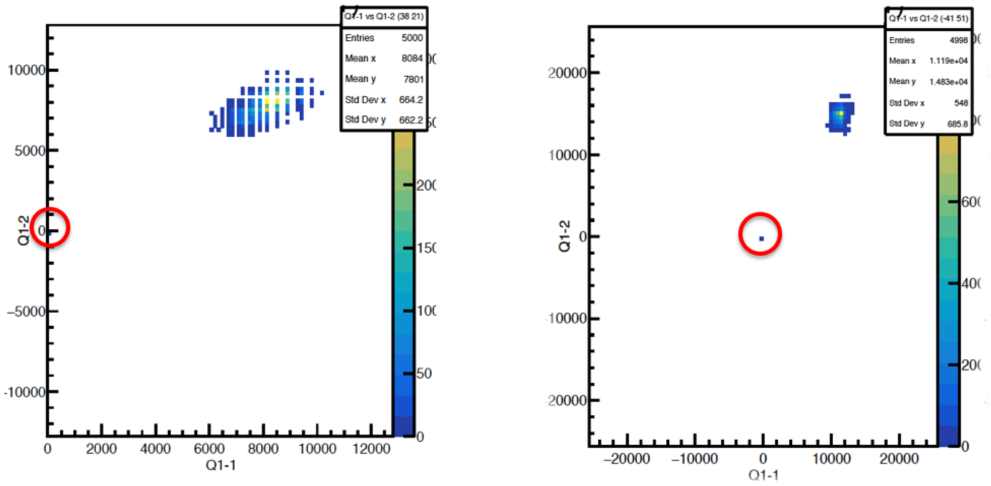

Figure 7.9. Noise on ADC channels (38 21) and (−41 51).

7.5. Charge Histograms

After the cuts, charge histograms of Q_1, Q_2 (Figure 7.10), Q_t and Q_p (Figure 7.11) are plotted separately. The histograms are created using events that remained after cuts. Two-channel data are added together. Nice bell-shaped distribution is observed in all histograms.

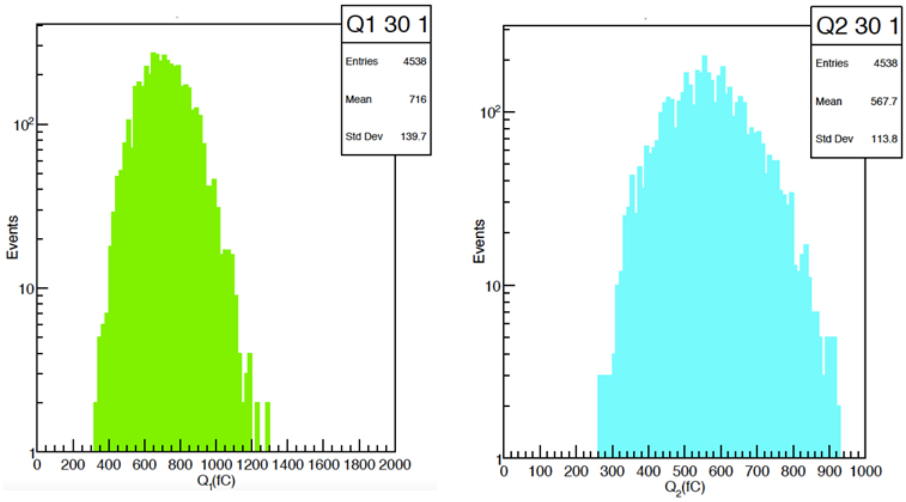

Figure 7.10. Q_1 and Q_2 histograms of channel (30 1) in run 321466.

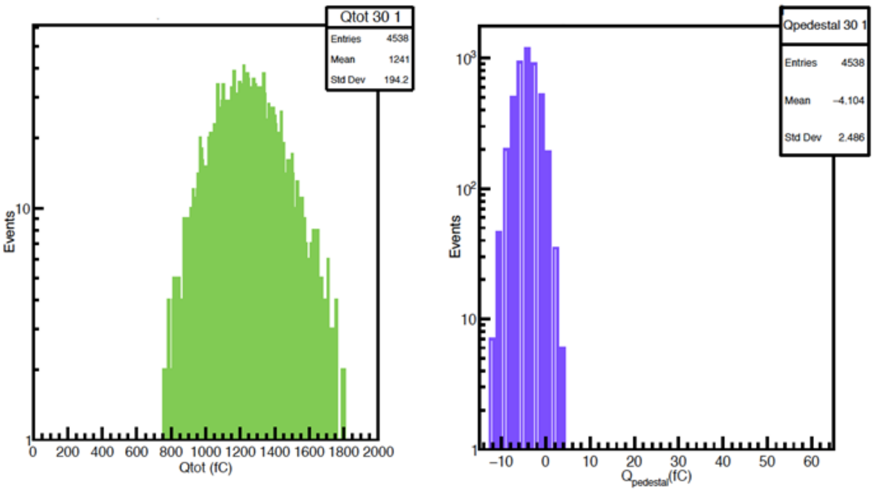

Figure 7.11. Q_{total} and $Q_{pedestal}$ histograms of channel (30 1) in run 321466.

7.6. $\frac{Q_2}{Q_1}$ Histograms

When all the cuts are applied, pedestals are subtracted and value for the $\frac{Q_2}{Q_1}$ ratio is calculated for each channel on an event by event basis. Then, a Gaussian fit is applied to the histograms in each run. Figure 7.12 demonstrates an example of Q_2/Q_1 histogram belonging to channel (30 37), run 327567. Green line shows actual data, where red curve is the Gaussian Fit. Statistics box in the figure contains the total number of entries, mean and standard deviation of data and three parameters (C,μ, σ) of a Gaussian distribution.

Mean value (μ) and its error from the Gaussian fit are used as ratio and statistical error in the analysis.

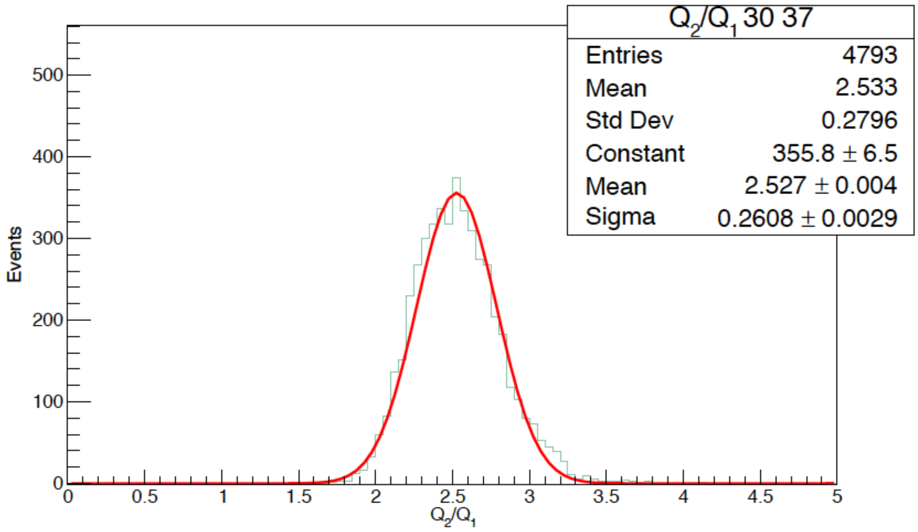

Figure 7.12. Q_2/Q_1 ratio histogram for channel (30 37) in run 327567.

7.7. Integrated Luminosity

As briefly mentioned in Chapter 2, integrated luminosity is a way of measuring the total number of collisions that has occurred during a time interval. Since the radiation is caused by secondary particles which are created in collisions, integrated luminosity gives us a measure of radiation, also. Figure 7.13 illustrates the day-by-day integrated luminosity during the same time interval that RadDam data are taken. This plot will be used to understand the radiation damage in the next section.

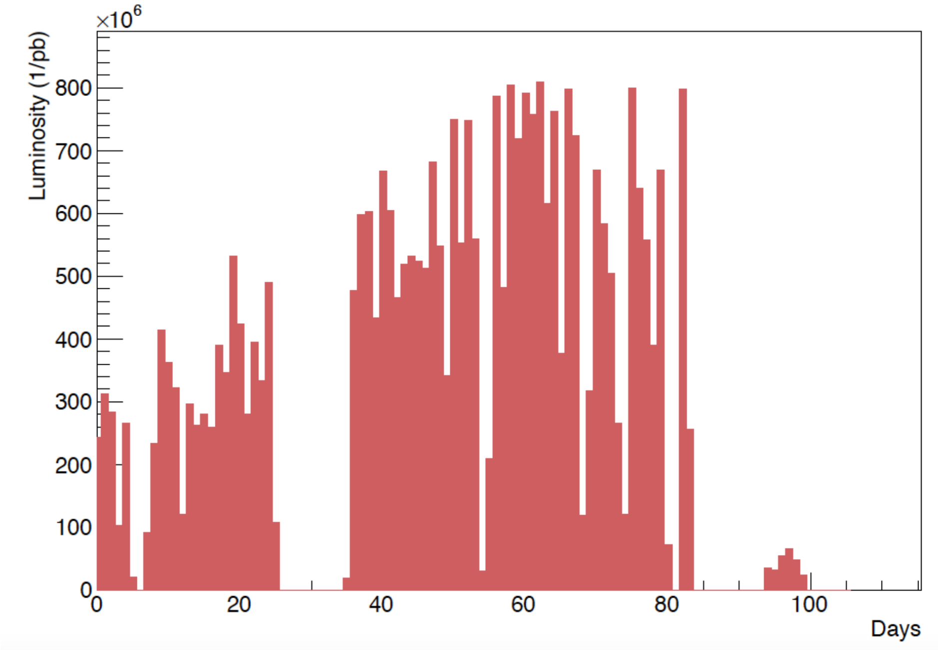

Figure 7.13. Day by day integrated luminosity in CMS during the time interval from August 19 to December 2, 2018.

7.8. Normalized Ratio Graphs

When it comes to the observation of radiation damage and recovery in a fibre, Q_2/Q_1 ratio alone does not say much. Careful examination of change in the ratio values with respect to time is needed. Before plotting graphs of ratio vs time, ratios are normalized with respect to day 0 ratio of each channel. With this normalization, we would like to provide a basis for comparison of each channels' radiation damage and recovery.

Following equations are used for calculating the normalized ratio and error:

$$n_i = \frac{r_i}{r_0} \tag{7.2}$$

$$e_i = \frac{r_i}{r_0} \times \sqrt{(\sigma_i/r_i)^2 + (\sigma_0/r_0)^2} \tag{7.3}$$

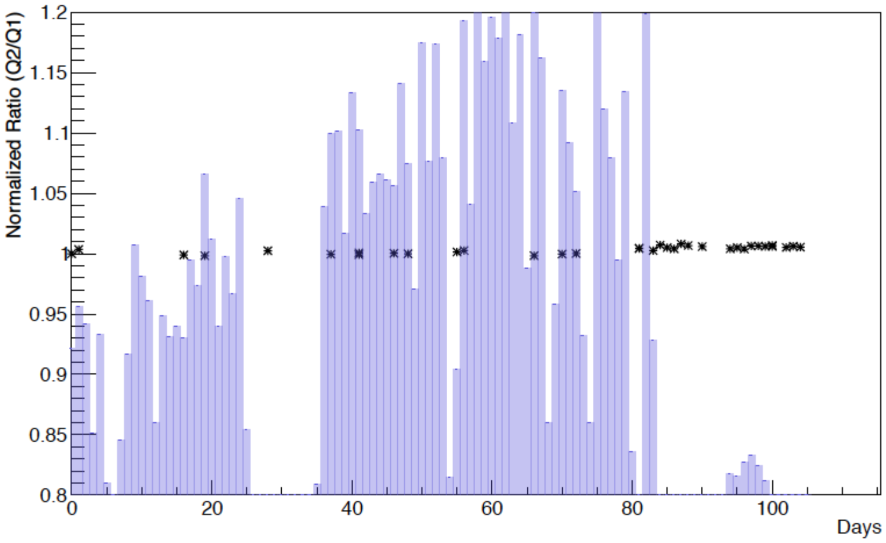

Figure 7.14. Graph of normalized ratios with respect to time of channel (30 21). Violet histogram displays the integrated luminosity for that day.

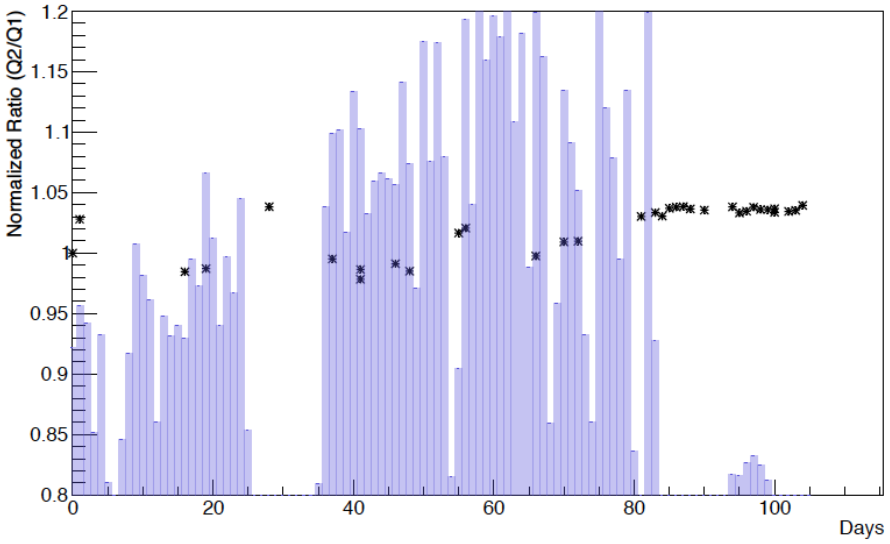

Figure 7.15. Graph of normalized ratios with respect to time of channel (41 19). Violet histogram displays the integrated luminosity for that day.

Figures 7.14 and 7.15 are two examples of normalized ratio histograms for low and high η rings, respectively. These histograms verify two expectations:

(i) Ratios decrease at high luminosity.

(ii) Change in ratios for lower $|\eta|$'s is smaller than higher ones.

7.9. Lego Plots

Since distance of fibres on the same η ring to Interaction Point (IP), where the collision takes place, are equal, radiation damage is expected to be the same. Thus, ratios compared as a function of ϕ for the same η, should show a flat distribution. To see all this in a combined manner, 2D Lego plots are drawn for all η rings on both HF+ and HF−. Figure 7.16 and 7.17 display the plots for low and high η values, respectively.

2D histograms show that there is no significant ratio difference in the channels for same η rings in the same run. Therefore, weighted average is calculated over ϕ values. Then, ratios are displayed with respect to η, for HF+ and HF− on 2D histograms separately (Figures 7.18 and 7.19).

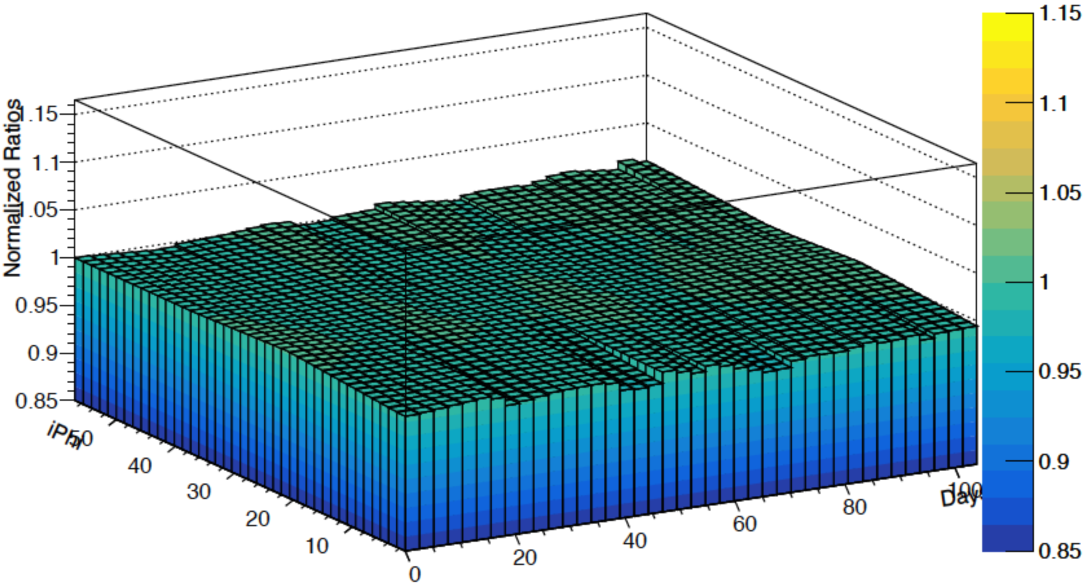

Figure 7.16. 2D lego plot of the ratio distribution in HF+ iEta 30 with respect to azimuthal angle.

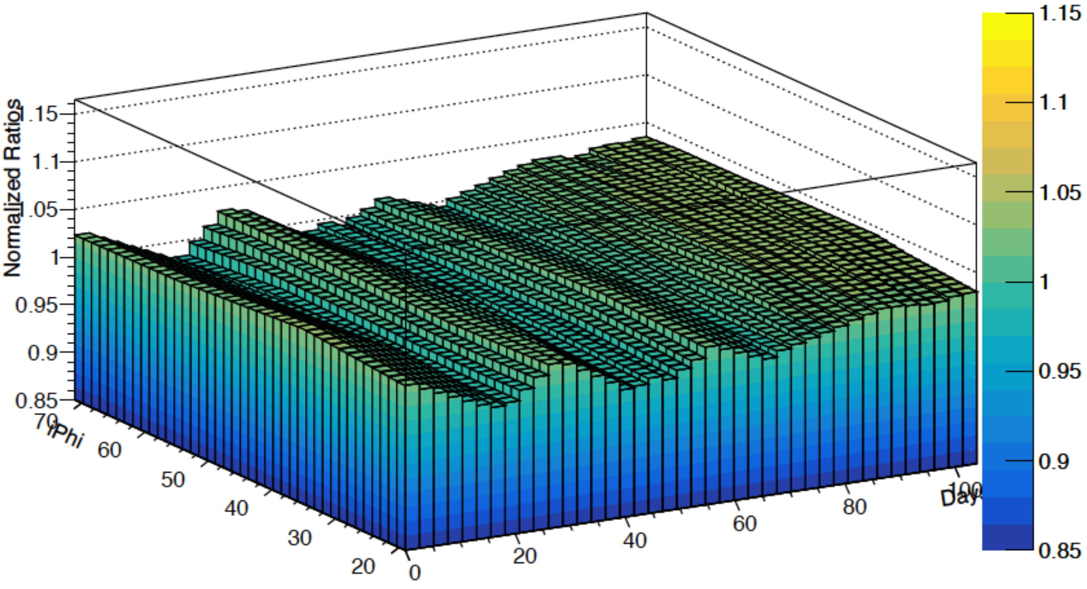

Figure 7.17. 2D lego plot of the ratio distribution in HF+ iEta 40 with respect to azimuthal angle.

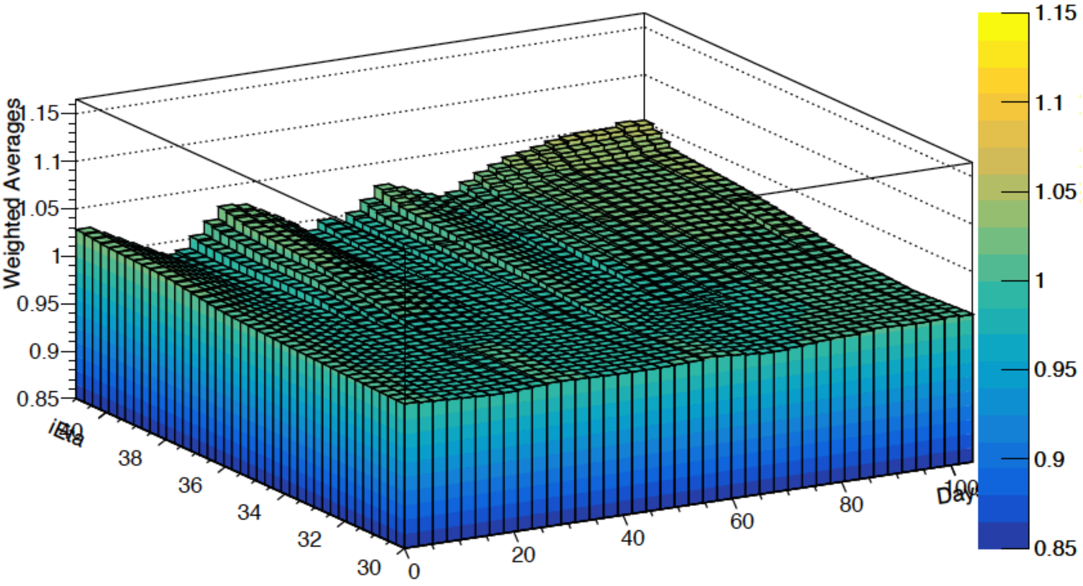

Figure 7.18. 2D lego plot of the ratio distribution in HF+ with respect to iEta (x: iEta, y: days, z: weighted averages).

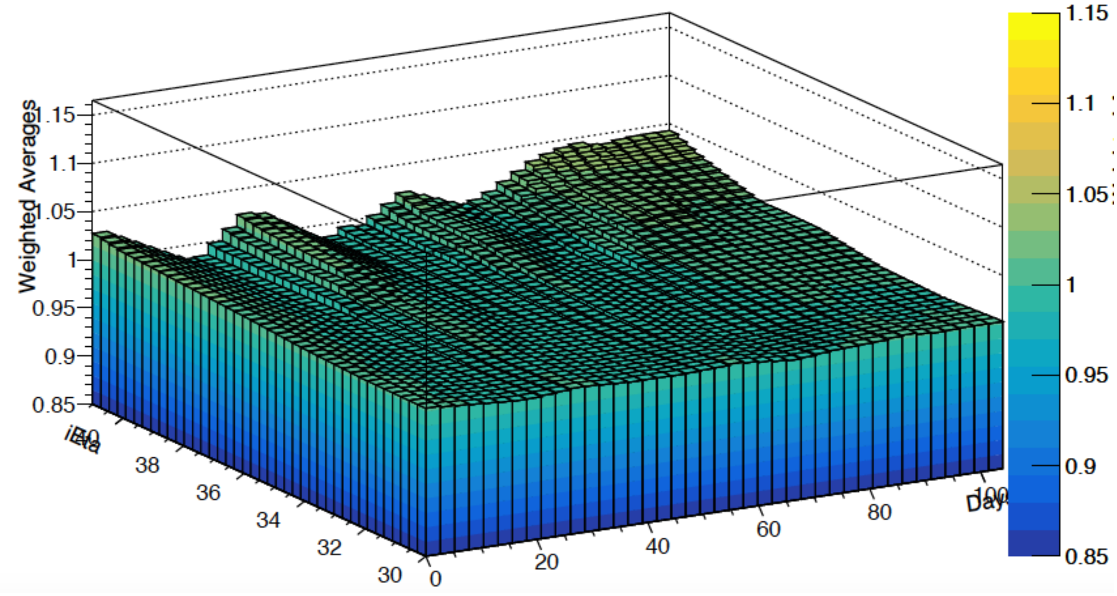

Figure 7.19. 2D lego plot of the ratio distribution in HF- with respect to iEta (x: iEta, y: days, z: weighted averages).

From Figures 7.18 and 7.19, one can conclude that radiation damage is relatively small for channels which are away from IP.

7.10. Hardware Problems

In some of the HF$-$ channels, a jump is observed on the ratio histograms in the runs that are taken after September 17. These channels are listed in Table 7.5.

Table 7.5. List of channels that have hardware problems.

iEta	**iPhi**
-30	35
-32	35
-34	35
-38	35
-40	35

From the Table 7.5, we can see that all problematic channels are at the same azimuthal angle of HF$-$ connected to the same crate. Figure 7.20 is an example of the jump seen in the normalized ratio graph belonging to Channel (-30 35).

In order to identify the problem, $\dfrac{Q_1+Q_2}{Q_t}$ vs Event Number graphs are produced for the run 323569, the first run taken after September 17. Shift at delay time slots is observed for the channels on Table 7.5. Figure 7.21 illustrates $\dfrac{Q_1+Q_2}{Q_t}$ vs Event Number graph of Channel (-32 35), before and after the jump. Thus, third delay time slot is selected for those channels, for the runs that are taken after September 17.

On Channel (-36 35 4), which lies on the same azimuthal angle with other problematic channels, signal is lost after September 17. By careful investigation, it was found out that a bad connection in the crate caused the problem. Figure 7.22 shows the signals before and after the signal loss. Therefore, Channel (-36 35) is not used in the analysis.

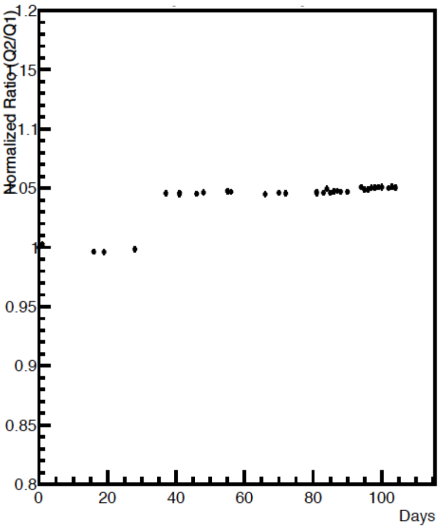

Figure 7.20. Jump observed in normalized ratio histogram of channel (−30 35).

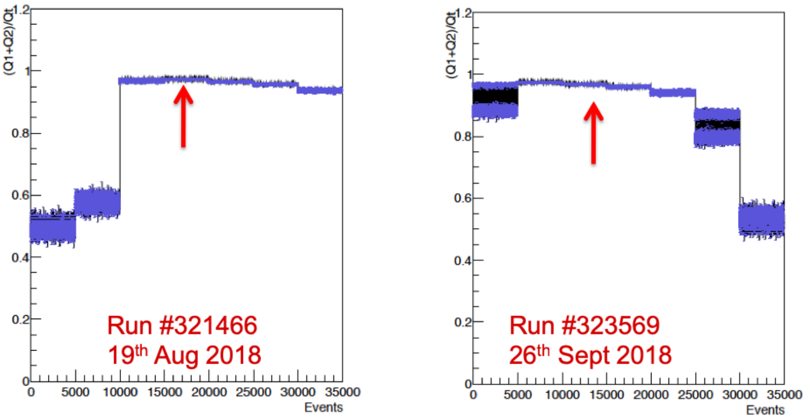

Figure 7.21. $\dfrac{Q_1 + Q_2}{Q_t}$ vs event number graphs of channel (−32 35), before and after the jump.

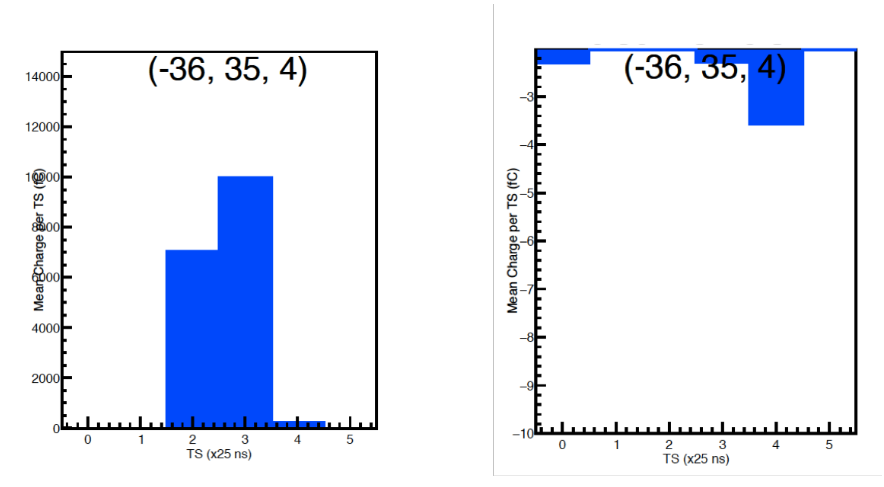

Run #321466
19th Aug 2018

Run #323569
26th Sept 2018

Figure 7.22. Pulse shape histogram of channel (−36 35) for run 321466 and 323569. The scale of the histograms are different.

7.11. Systematic Errors

In a measurement, two types of error are possible: Statistical and Systematic Errors. To reduce the effect of statistical error by means of taking averages, nearly 5000 events per run are used. The error in the mean obtained in the Gaussian fit of the 5000 events is taken as the statistical error. Average statistical uncertainty for the normalized ratios is around 0.2%.

For the systematic errors, three cases are outstanding: Delay Time Slots, TDC Cuts and Day 0 for normalization. Thus, the total systematic error that we can think of is estimated as:

$$\sigma_{total}^2 = \sigma_{delaytime}^2 + \sigma_{cut}^2 + \sigma_{day0}^2 \tag{7.4}$$

7.11.1. Delay Time Error

In order to observe the effect of delay time selection, the analysis is repeated with adjacent delay time slots to the main selection, which are on the plateau-like region also. In Figure 7.23, pink arrow and dots represent delay time slot and ratios for main selection in the analysis, while light and dark blue ones are for the neighbours.

Normalized percentage error is calculated for each run and weighted average of these errors is used as systematic error for delay time selection of the channel. Then, distribution of delay time systematic errors for 55 channels are displayed on a histogram (Figure 7.24).

Mean of the histogram, 0.12%, is used as the final value of the systematic error for delay times.

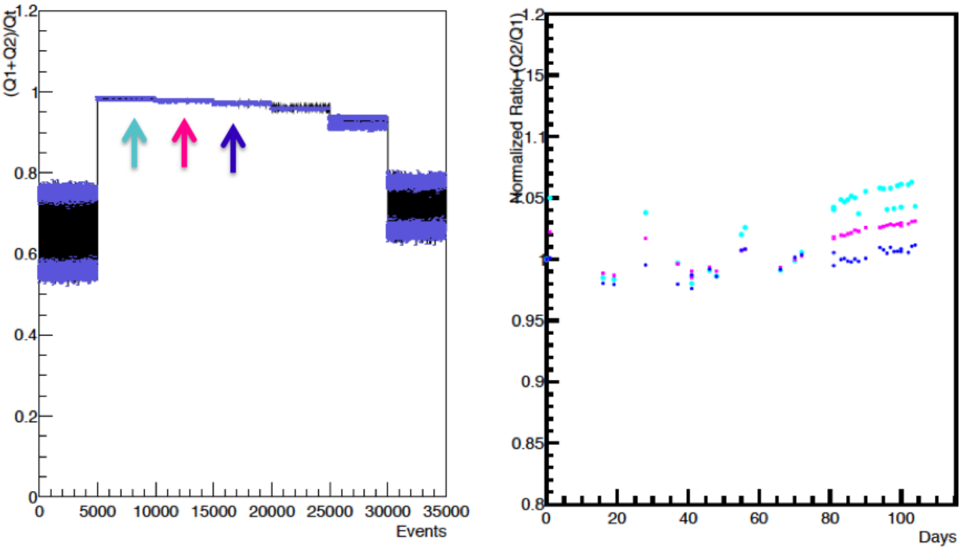

Figure 7.23. Different delay time slots and their ratio graphs for channel (−40 71).

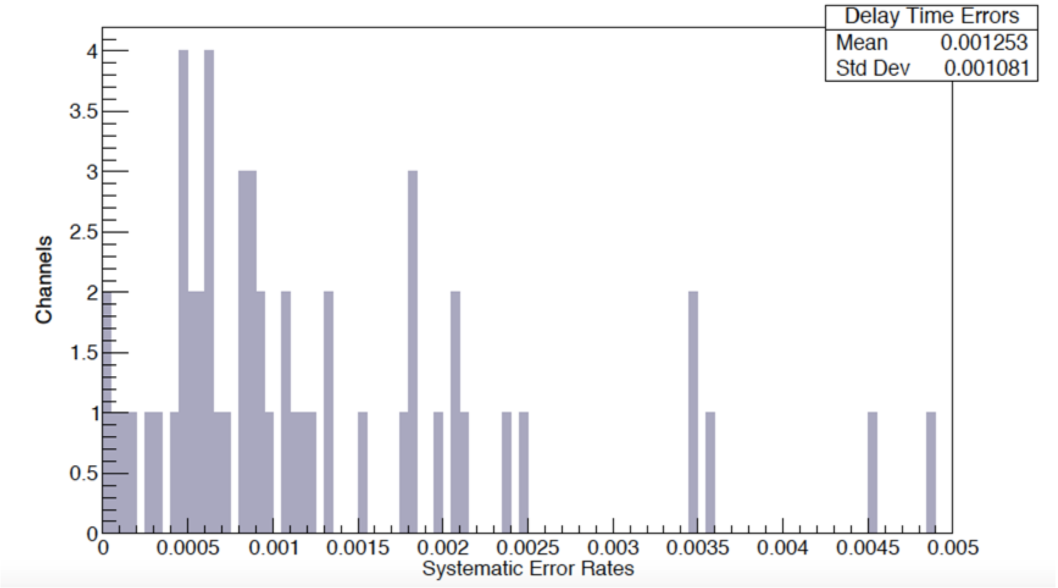

Figure 7.24. Distribution of the delay time errors for 55 channels.

7.11.2. TDC Cut Error

Similar procedure is applied for TDC cuts[3] . The analysis is repeated with all the data, i.e. no cuts placed on TDC values.

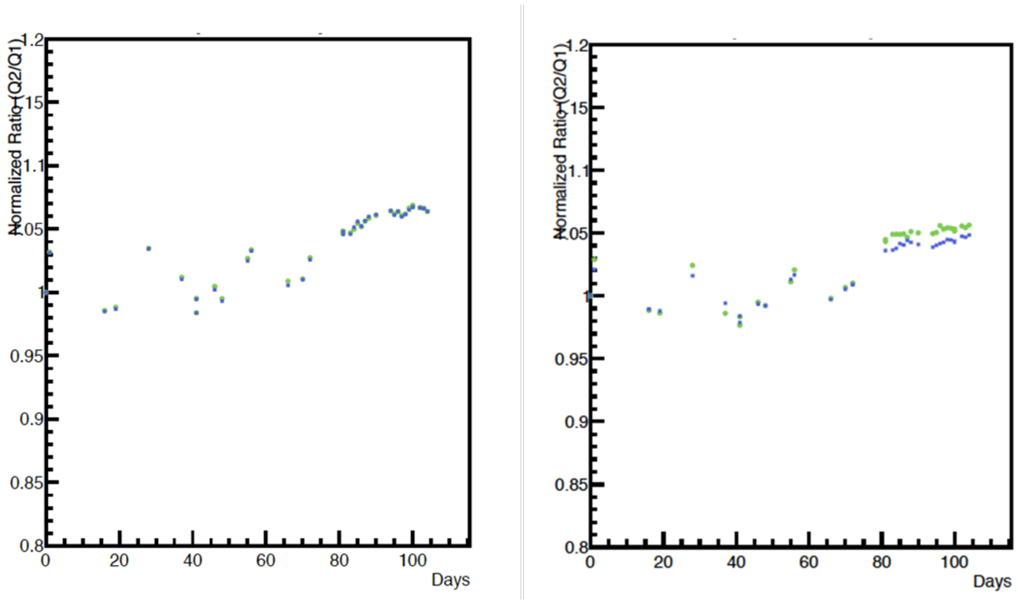

Figure 7.25. Ratio graphs with TDC cuts and full data for channels (41 55) and (−41 35). Blue dots illustrate ratios with no cut while green ones with cuts.

Figure 7.26 shows the distribution of normalized errors of 55 channels due to TDC cuts. Mean of the histogram, 0.02%, is used as the final value of systematic error for TDC cuts.

---

[3] Charge cuts are excluded because including the discarded values produces undefined (zero divide operation) ratio values which makes it impossible to continue with the analysis.

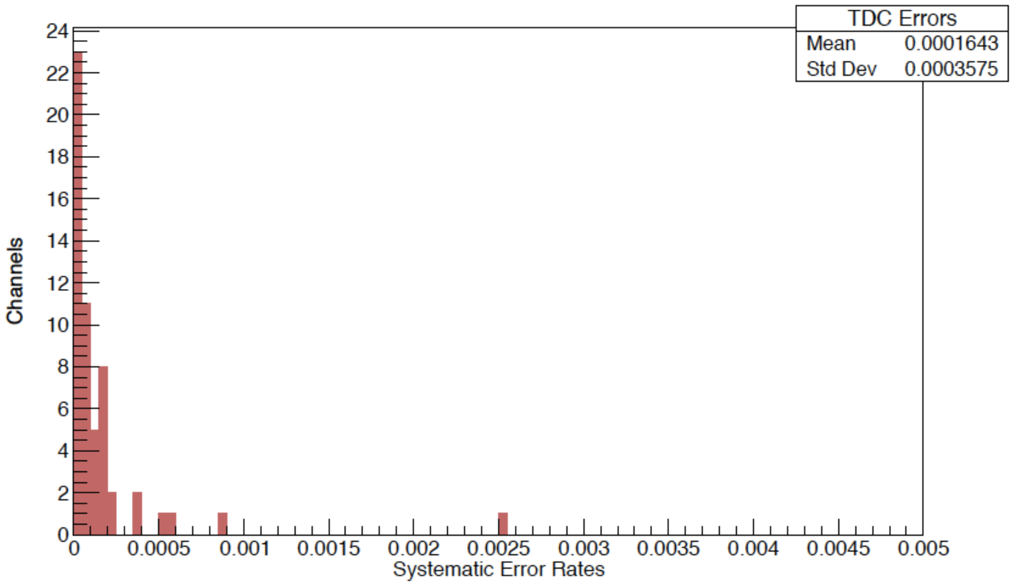

Figure 7.26. Distribution of the TDC cut errors for 55 channels.

7.11.3. Day-0 Error

Ratio value at August 19 (day-0) is selected as normalization constant for each channel, as mentioned earlier. Nonetheless, there may be some fluctuations in this value. Therefore, selection of normalization value gives us a systematic error.

To determine the effect of normalization constant on ratio values, the analysis is repeated with 35 ratios as normalization constant. Then, mean and standard deviations of 35 different ratios are calculated for each run and channel. Furthermore, normalized errors belonging to channels that are on the same η ring are averaged.

Figure 7.27 displays the average normalized errors for different η rings and modules (HF+ and HF−). As demonstrated earlier, lower $|\eta|$'s receive less radiation. However, as η increases the radiation damage effect starts to dominate over the systematic uncertainty due to day-0 normalization. Thus, the day-0 normalization uncertainty is computed using only the values measured at low $|\eta|$'s.

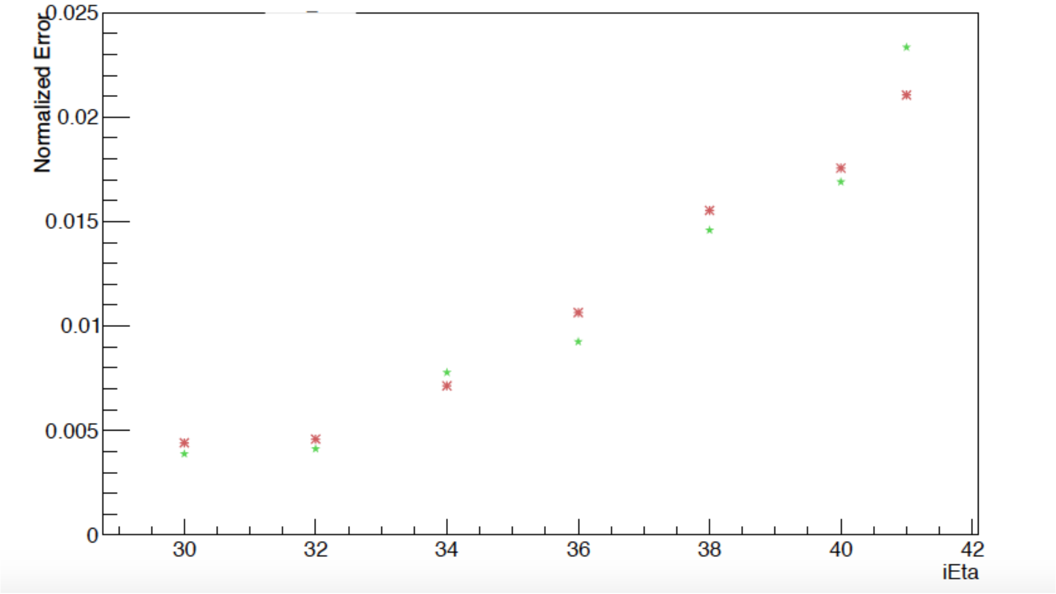

Figure 7.27. Average day-0 normalized uncertainty with respect to $|\eta|$ (green: HF-, terra-cota: HF+).

Average of normalized percentage error for 4 iEta rings 30, 32, −30 and −32, which is 0.5%, is taken as the final value for day-0 systematic error.

Final values of systematic errors are summarized in Table 7.6 below:

Table 7.6. Systematic error estimation.

$\sigma_{delaytime}$	σ_{cut}	σ_{day0}	σ_{total}
0.02%	0.12%	0.5%	0.5%

8. CONCLUSION

Purpose of this analysis is to find the change in transparency of fibres on HF detectors with respect to time and accumulated dose. As a measure of fibre transparency, ratio of the magnitude for the reflected and incoming light is used. The novelty of the new HF RadDam laser system is that incoming and reflected signals are well separated. Thus, it allows us to perform a more accurate analysis of data, compared to past measurements.

TDC is a new functionality of the front-end electronics, which comes with the new QIE10. Along with the ADC information, TDC provides us with a better selection of the real signals. Two channels of the ADC and TDC are helpful to eliminate the noisy signals.

No significant variations of fibre transparency as a function of the azimuthal angle is observed in accordance with the expectations. As absolute pseudorapidity increases, radiation damage and recovery becomes more pronounced.

In the analysis, statistical errors are obtained from the Gaussian fitting of data from nearly 5000 events. Furthermore, possible causes of systematic error are seen as delay time selection, TDC cuts and day-0 selection for normalization. Total systematic error due to these causes is estimated to be 0.5%. Average statistical error for the normalized ratios is 0.2%.

As a follow up for the work discussed in this thesis, radiation dose received by specific $\Delta\eta \times \Delta\phi$ towers of both HF modules will be estimated by using the integrated luminosity. Then, the results of the analysis given here will be used to compare the expected radiation damage due to the dose received by each channel with the measured radiation damage.

REFERENCES

1. Brüning, O. S., P. Collier, P. Lebrun, S. Myers, R. Ostojic, J. Poole and P. Proudlock, *LHC Design Report*, CERN Yellow Reports: Monographs, CERN, Geneva, 2004, `https://cds.cern.ch/record/782076`.

2. *What is a synchrotron?*, `https://www.esrf.eu/about/synchrotron-science/synchrotron`, accessed in March 2019.

3. *LHC the Guide*, `https://cds.cern.ch/record/2255762/files/CERN-Brochure-2017-002-Eng.pdf`, accessed in March 2019.

4. *Magnet System*, `https://atlas.cern/discover/detector/magnet-system`, accessed in March 2019.

5. *Detector*, `http://cms.cern/detector`, accessed in April 2019.

6. *Silicon Strips*, `http://cms.cern/detector/identifying-tracks/silicon-strips`, accessed in April 2019.

7. Baiatian, G. and e. a. Sirunyan, *Design, Performance, and Calibration of CMS Hadron-Barrel Calorimeter Wedges*, Tech. Rep. CMS-NOTE-2006-138. 1, CERN, Geneva, 2007, `https://cds.cern.ch/record/1049915`.

8. Brice, M., L. Vaillet and L. Lazic, *Images of the CMS HCAL Barrel (HB)*, Nov 2008, `https://cds.cern.ch/record/1431485`, CMS Collection.

9. *Measurements of the forward energy flow and forward jet production with CMS*, `http://inspirehep.net/record/930964/plots`, accessed in February 2019.

10. Baiatian, e. a., G, *Design, Performance and Calibration of the CMS Forward Calorimeter Wedges*, Tech. Rep. CMS-NOTE-2006-044, CERN, Geneva, Feb 2006,

`https://cds.cern.ch/record/951395`.

11. Onel, Y., “Present status of CMS HF quartz fiber calorimetry”, *10th International Conference On Calorimetry In Particle Physics*, 2002, `http://cds.cern.ch/record/807347`.

12. *Concepts in Digital Imaging Technology*, `https://micro.magnet.fsu.edu/primer/digitalimaging/concepts/photomultipliers.html`, accessed in March 2019.

13. Koseyan, O. K., *Phase 1 Upgrade of the Hadronic Forward Calorimeter - Testing the Frontend DAQ Electronics Cards*, Master’s Thesis, 2018, `http://cds.cern.ch/record/2307068`.

14. Hughes, E., *A New Generation Of Charge Integrating ADC For The CMS HCAL Upgrade*, `https://indico.cern.ch/event/192695/contributions/353256/attachments/277181/387778/Elliot-Hughes.pdf`, accessed in February 2019.

15. Mans, J. and e. a. Anderson, *CMS Technical Design Report for the Phase 1 Upgrade of the Hadron Calorimeter*, Tech. Rep. CERN-LHCC-2012-015. CMS-TDR-10, Sep 2012, `https://cds.cern.ch/record/1481837`, additional contact persons: Jeffrey Spalding, Fermilab, spalding@cern.ch, Didier Contardo, Universite Claude Bernard-Lyon I, contardo@cern.ch.

16. Merlo, J.-P., “On line monitoring of radiation damage and recovery in quartz fibres using reflected light”, *Astroparticle, Particle and Space Physics, Detectors and Medical Physics Applications*, 2008.

17. *CMS HCAL Service Works*, `https://indico.hephy.oeaw.ac.at/event/130/contribution/1/material/slides/0.pdf`, accessed in March 2019.

18. Merlo, J.-P., “Monitoring of Radiation Damage of Quartz Fibers in the HF-CMS

Detector", *14th ICATPP Conference on Astroparticle, Particle, Space Physics and Detectors for Physics Applications*, Sep 2013.

19. Cankocak, K., N. M. Bakirci, S. Cerci, E. Gülmez, J.-P. Merlo, Y. Onel, F. Ozok, I. Schmidt and N. Sonmez, *Radiation-Hardness Measurements of High* OH^- *Content Quartz Fibres Irradiated with 24 GeV Protons up to 1.25 Grad*, Tech. Rep. CMS-NOTE-2007-003, CERN, Geneva, Jan 2007, `https://cds.cern.ch/record/1020051`.

20. Dumanoglu, I. and J.-P. Merlo, *Radiation-Hardness Studies of High OH Content Quartz Fibers Irradiated with 500 MeV Electrons at CERN*, Tech. Rep. CMS-NOTE-2001-020, CERN, Geneva, May 2001, `https://cds.cern.ch/record/687342`.

21. Onel, Y. (Editor), *Design, Construction and Commissioning of the Upgrade Radiation Damage Monitoring System of the CMS Hadron Forward Calorimeters*, IEEE-NSS-MIC-2018 2018 IEEE Nuclear Science Symposium and Medical Imaging Conference, 2018.

APPENDIX A: HISTOGRAMS

A.1. Pulse Shapes

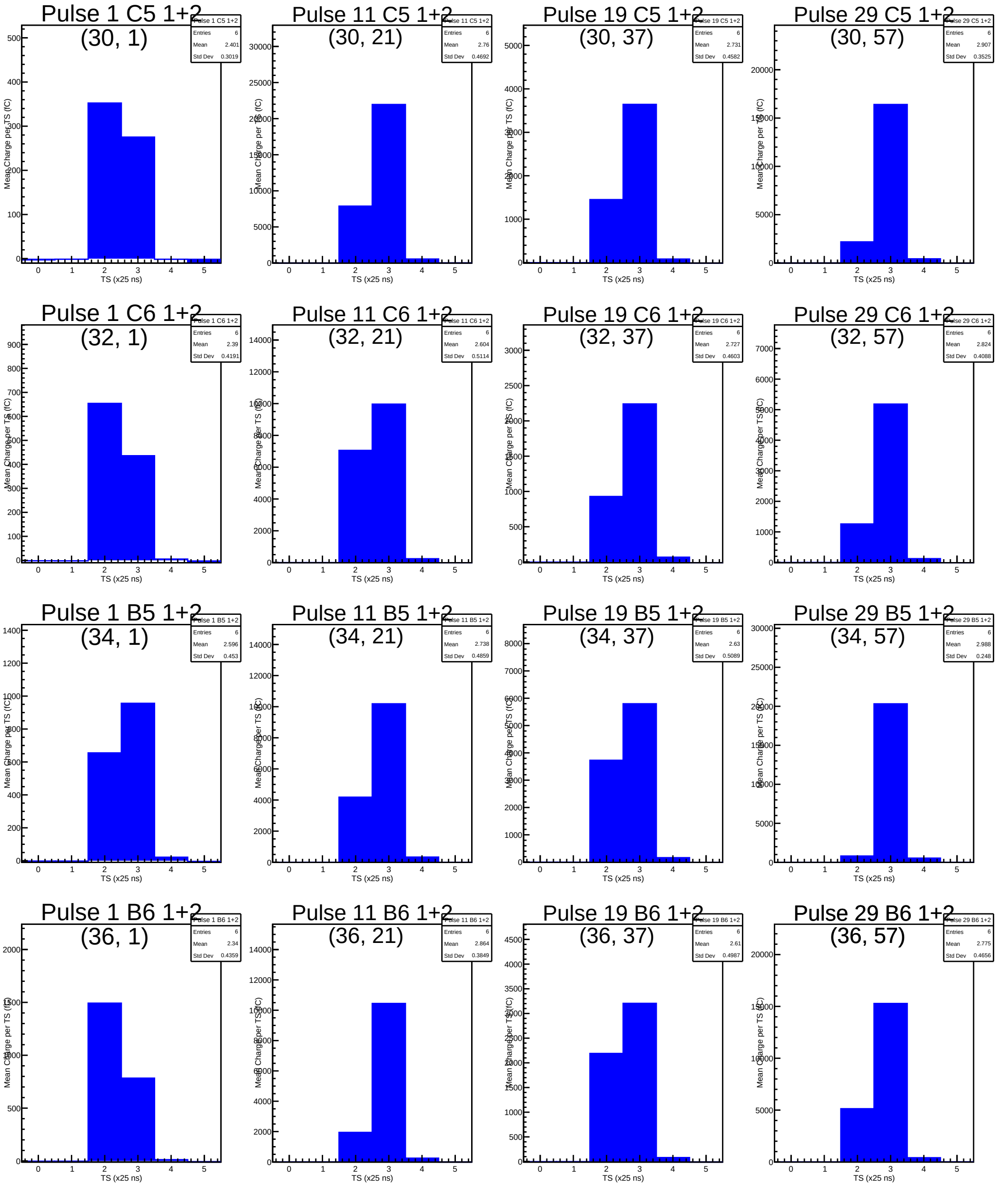

Figure A.1. Pulse shapes histograms of all channels in run 321585.

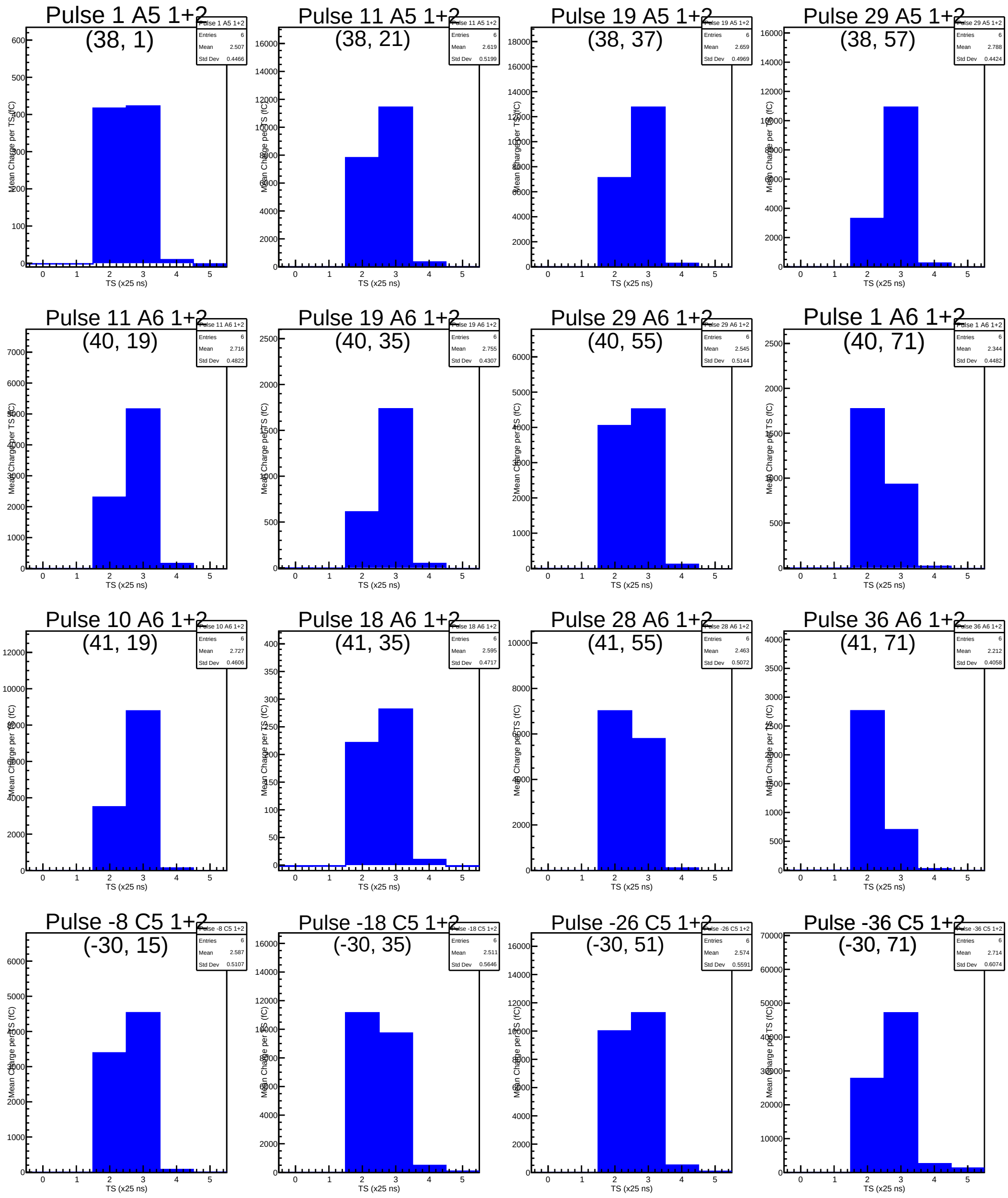

Figure A.1. Pulse shapes histograms of all channels in run 321585 (cont.).

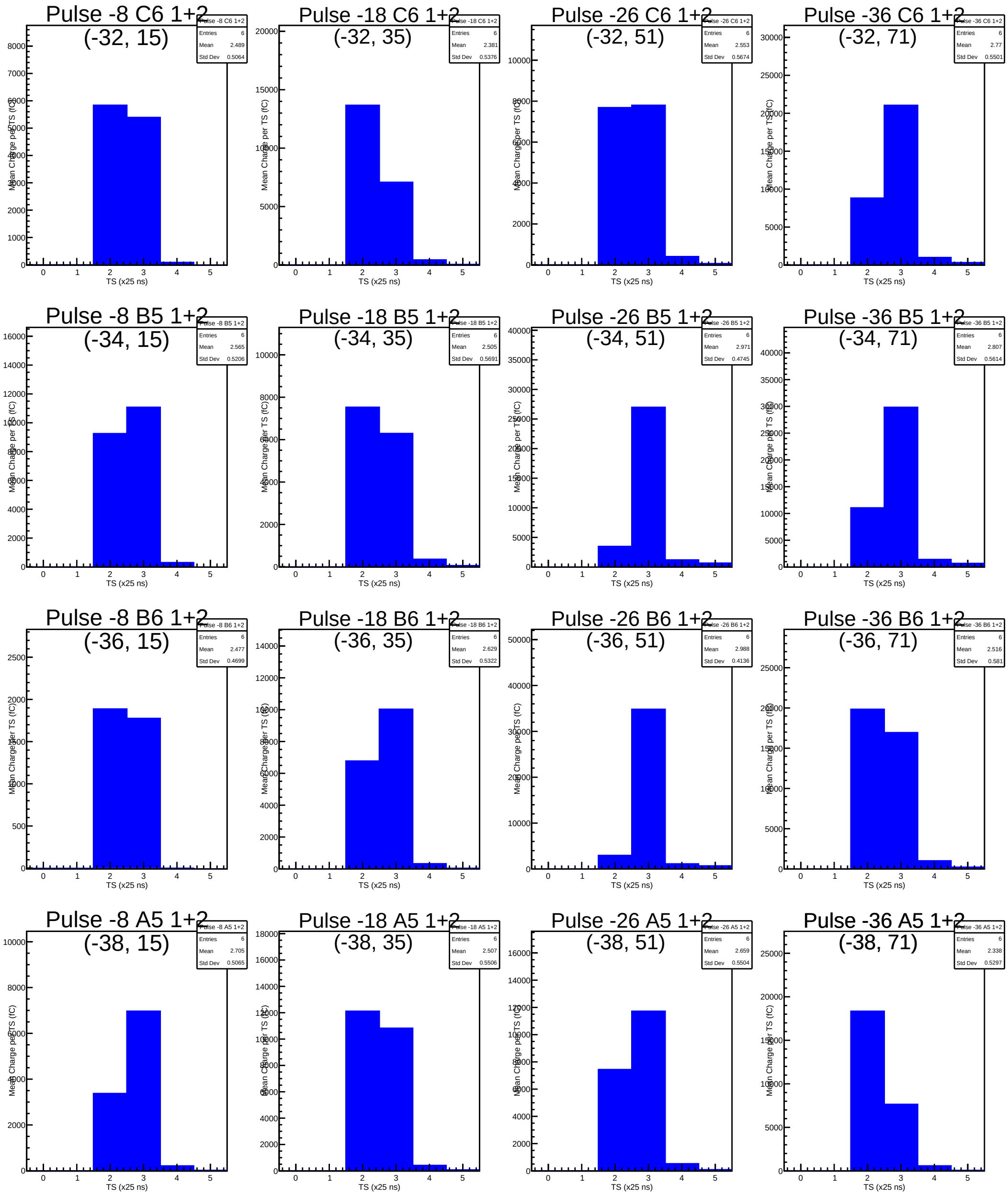

Figure A.1. Pulse shapes histograms of all channels in run 321585 (cont.).

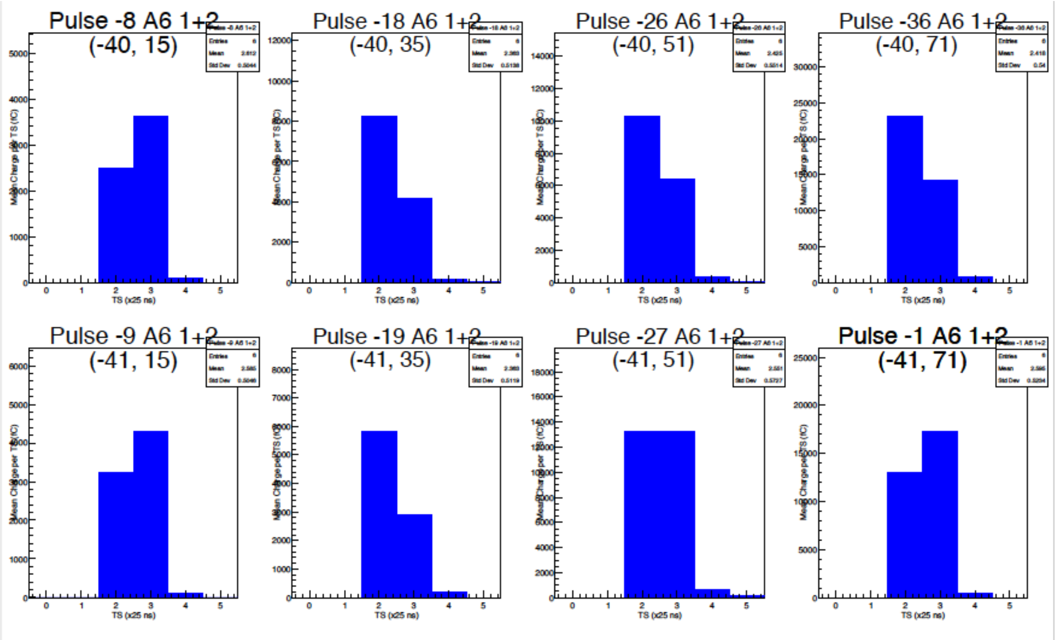

Figure A.1. Pulse shapes histograms of all channels in run 321585 (cont.).

A.2. TDC Shapes

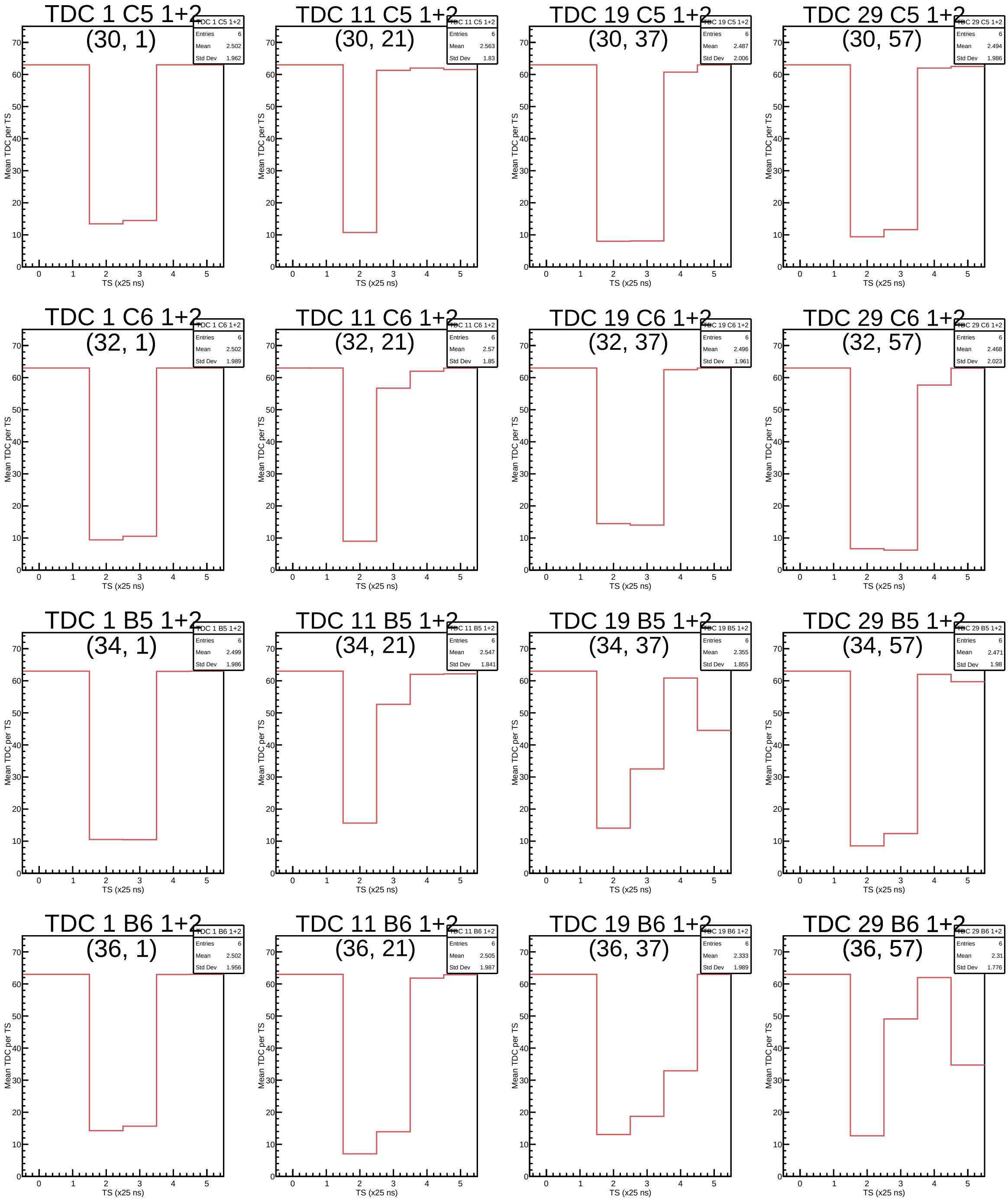

Figure A.2. TDC shapes histograms of all channels in run 321585.

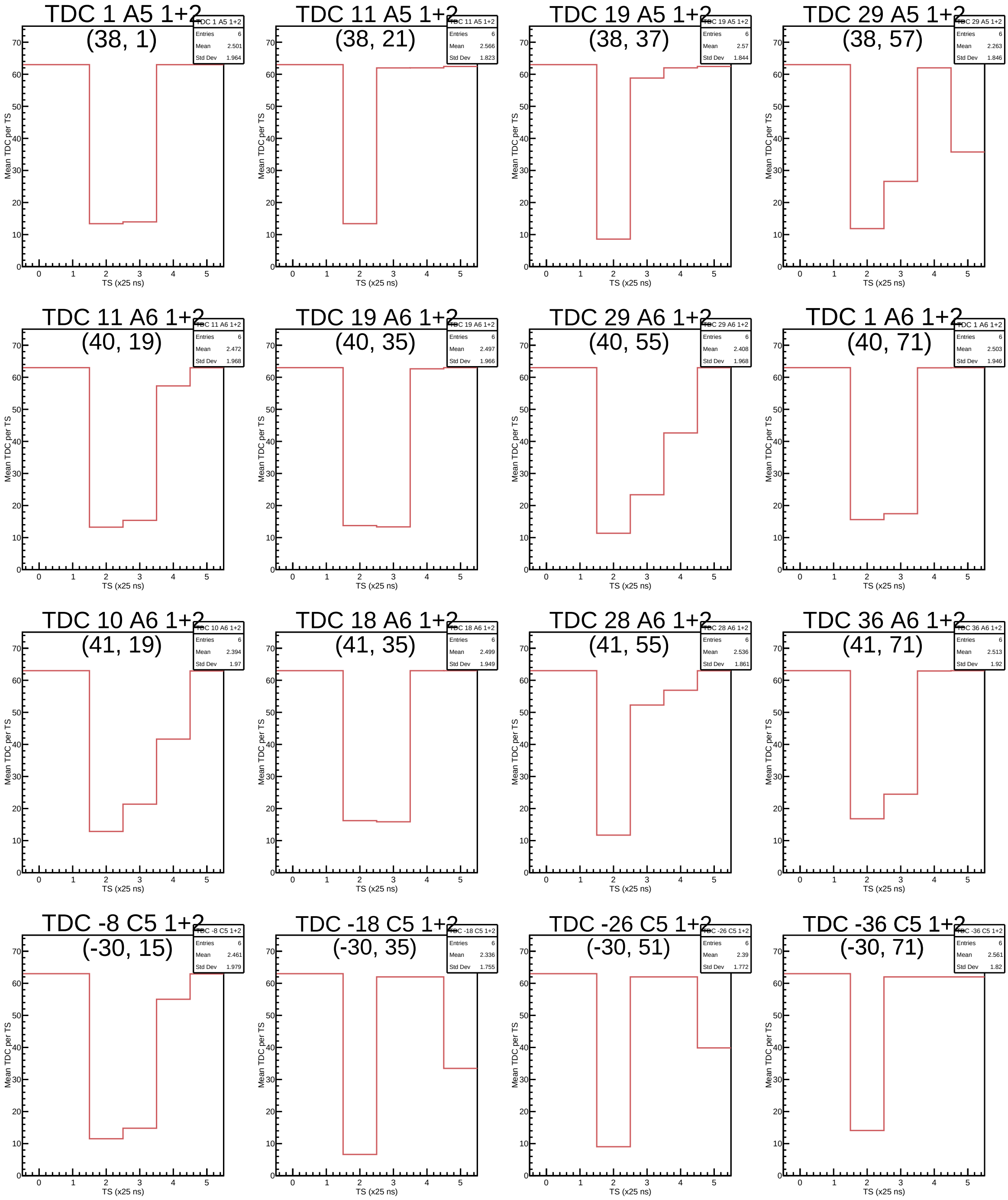

Figure A.2. TDC shapes histograms of all channels in run 321585 (cont.).

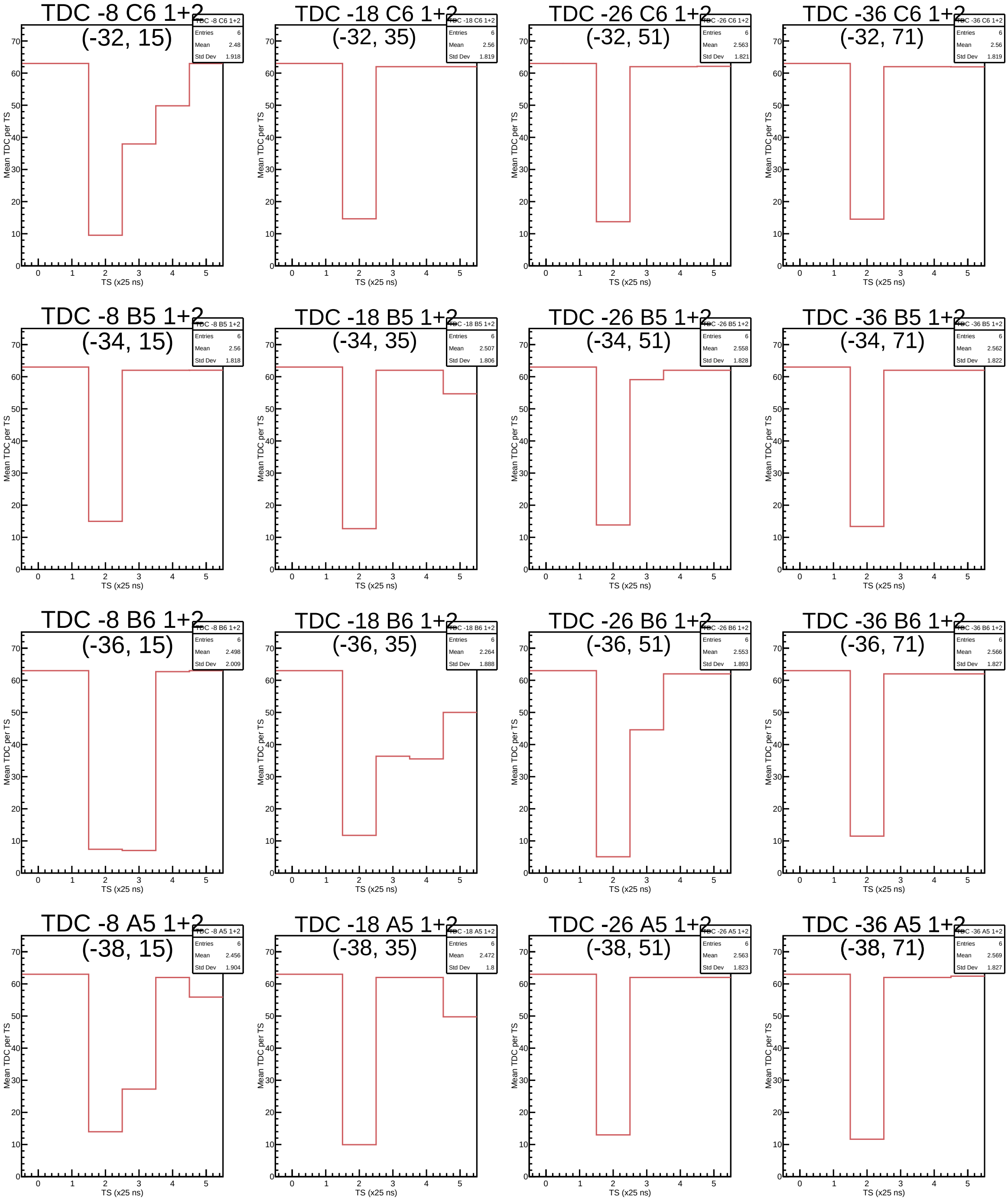

Figure A.2. TDC shapes histograms of all channels in run 321585 (cont.).

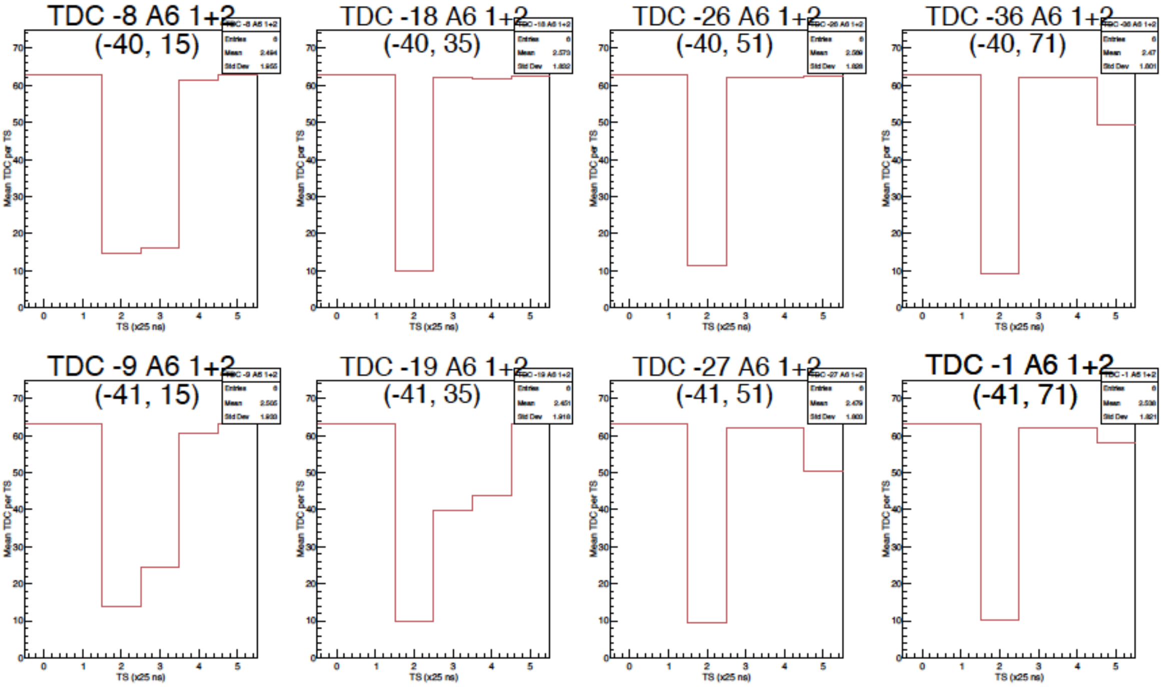

Figure A.2. TDC shapes histograms of all channels in run 321585 (cont.).

A.3. Q_1 Histograms

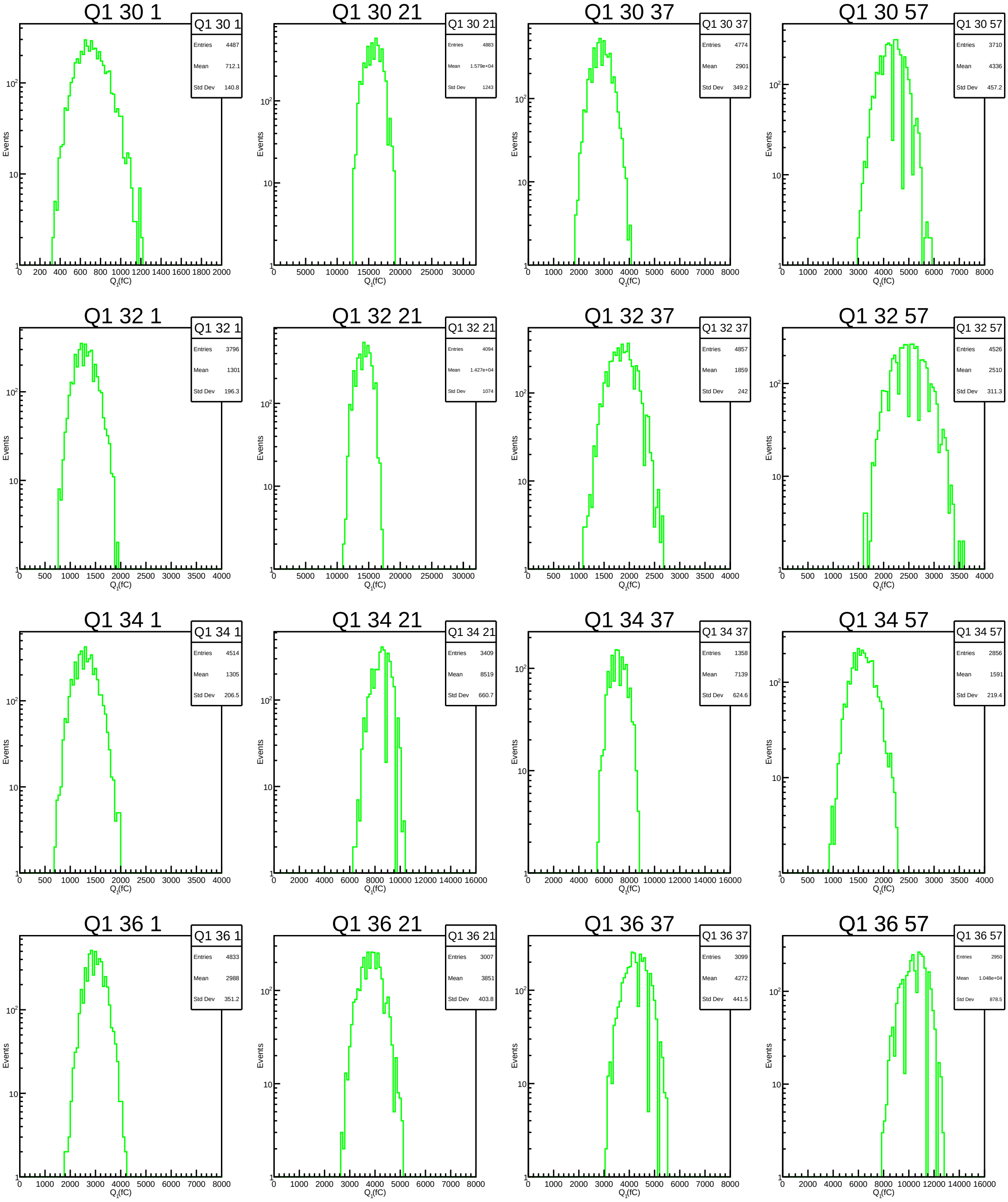

Figure A.3. Q_1 histograms of all channels in run 321585.

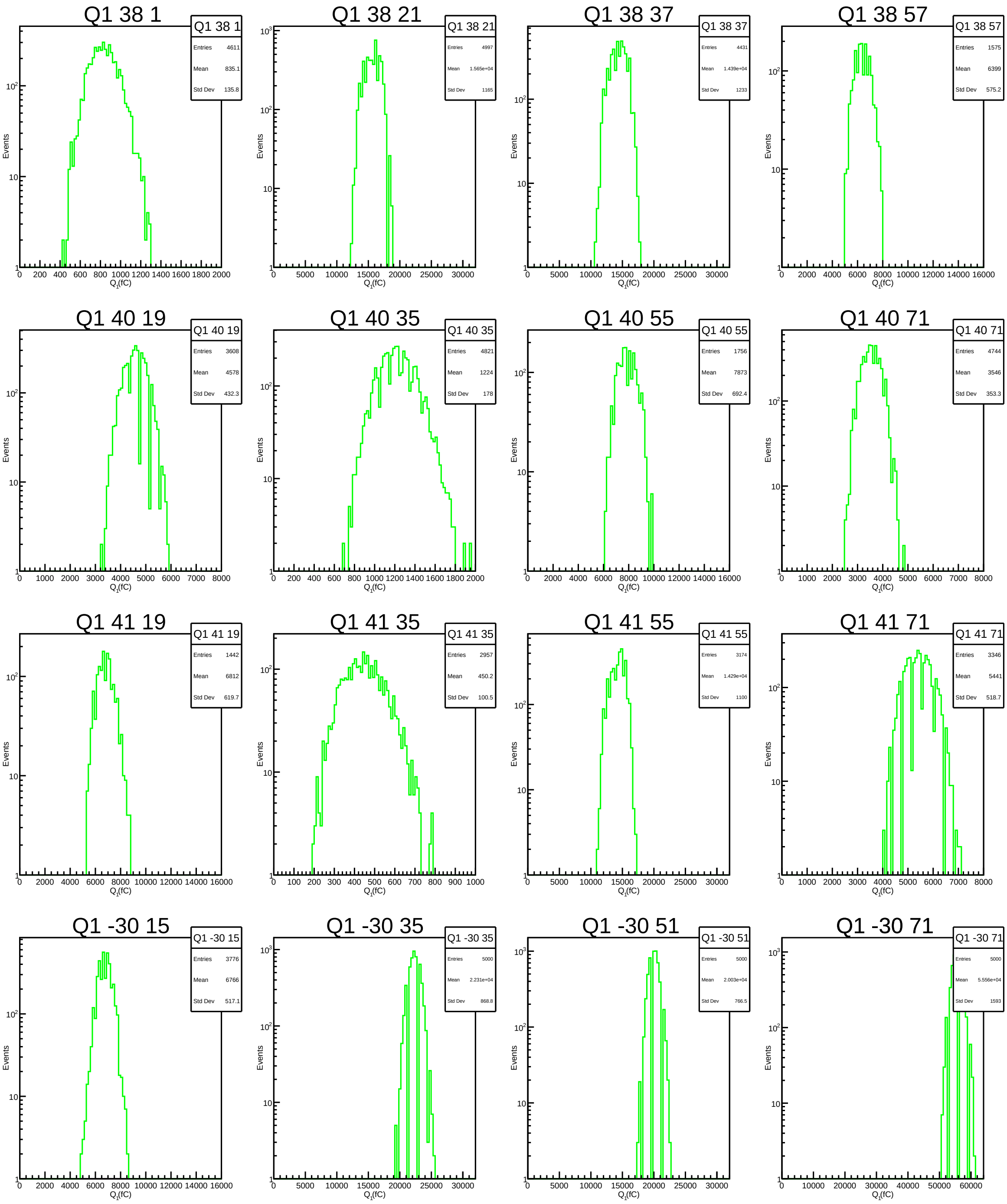

Figure A.3. Q_1 histograms of all channels in run 321585 (cont.).

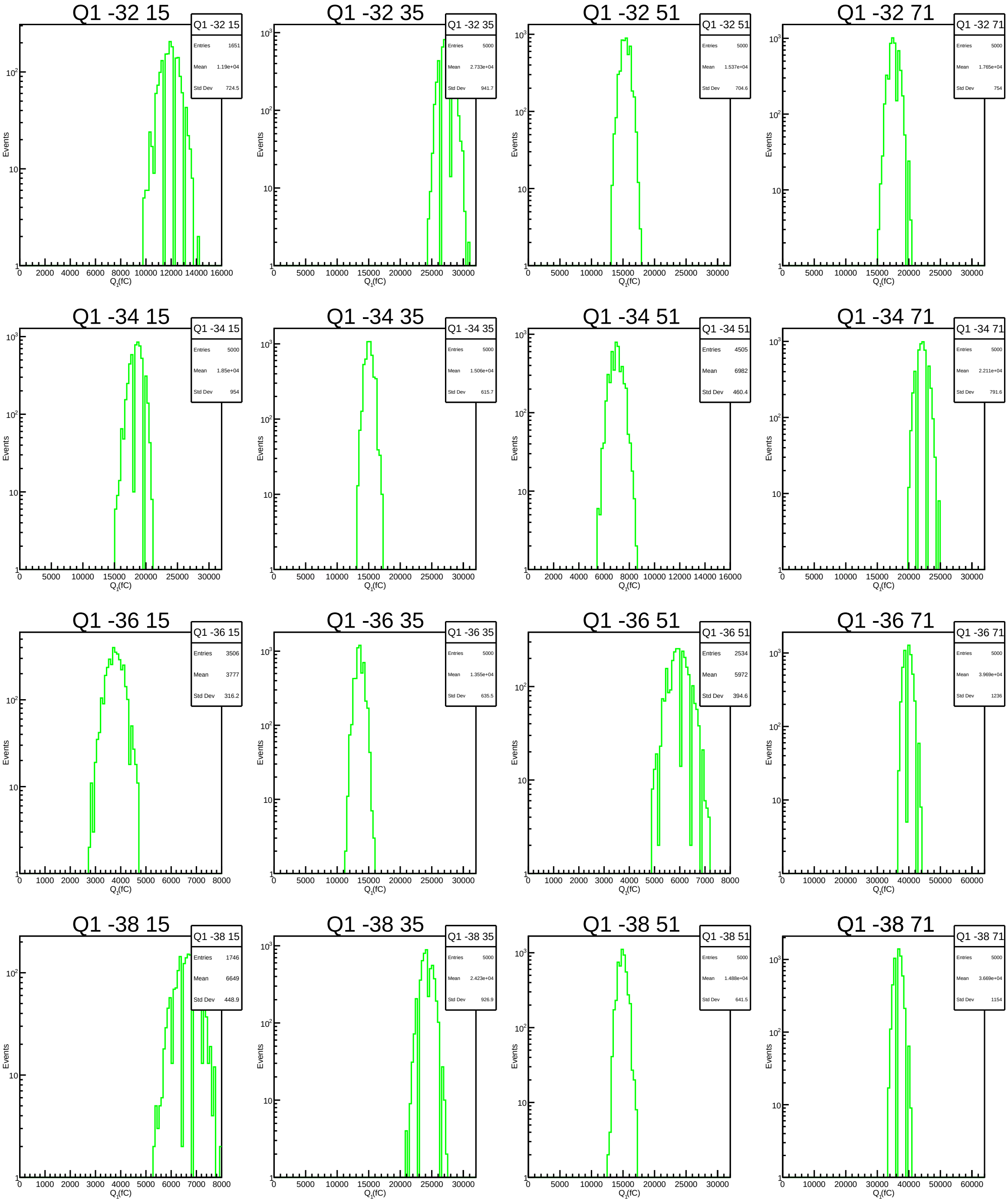

Figure A.3. Q_1 histograms of all channels in run 321585 (cont.).

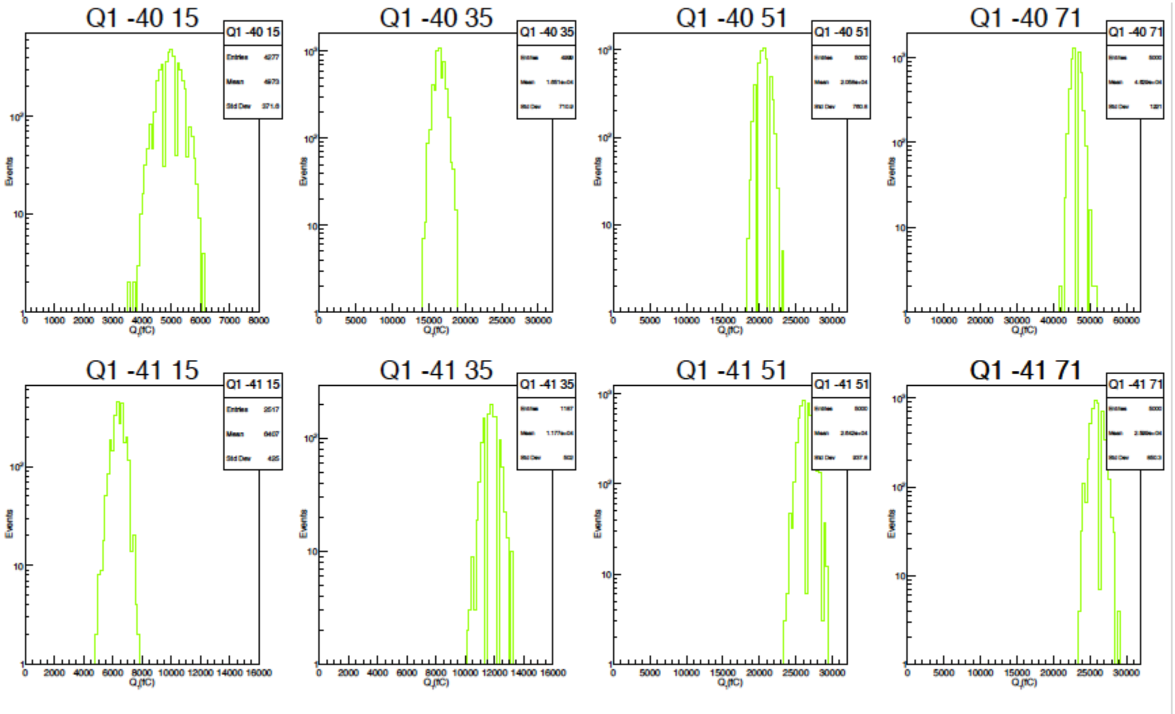

Figure A.3. Q_1 histograms of all channels in run 321585 (cont.).

A.4. Q_2 Histograms

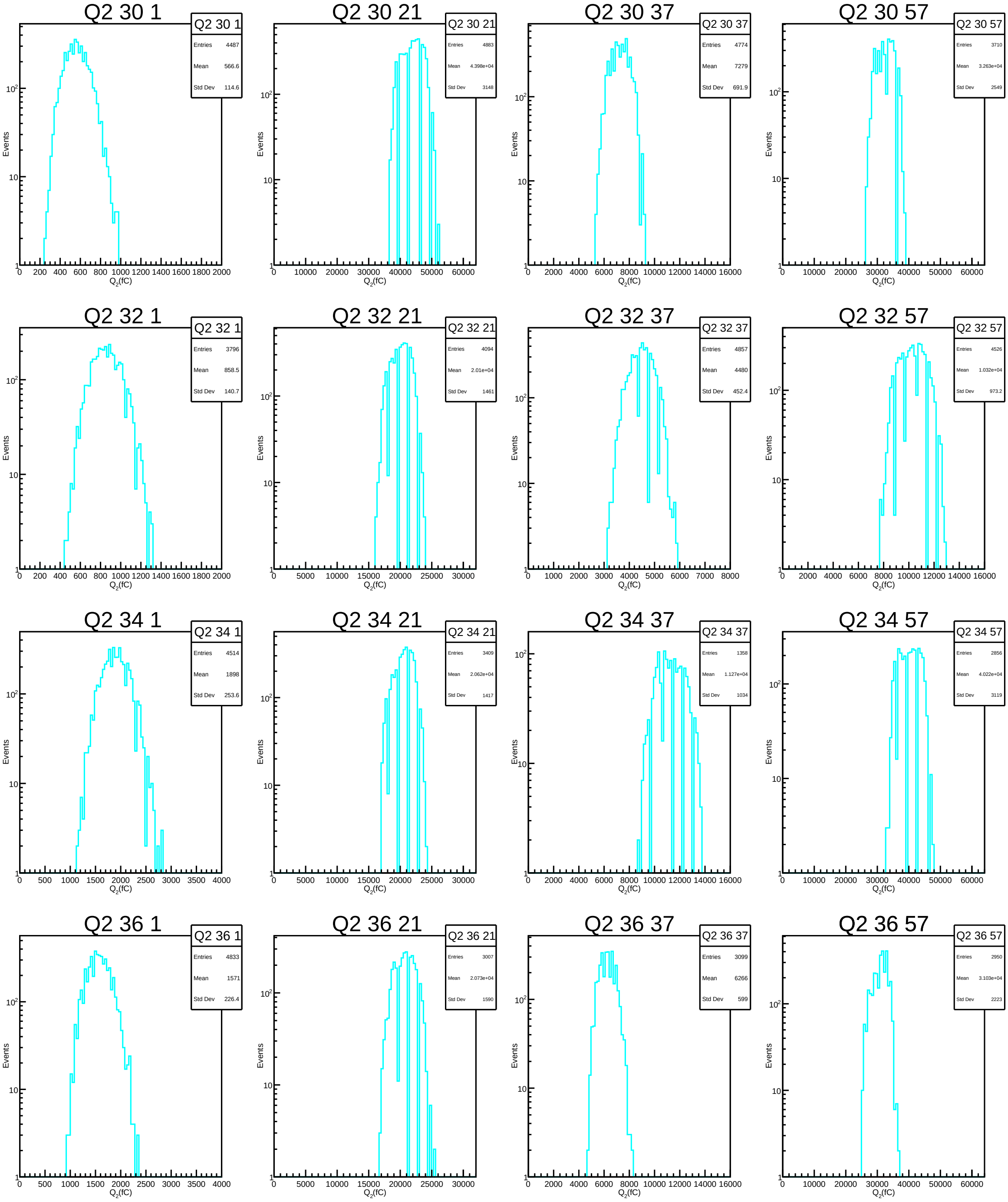

Figure A.4. Q_2 histograms of all channels in run 321585.

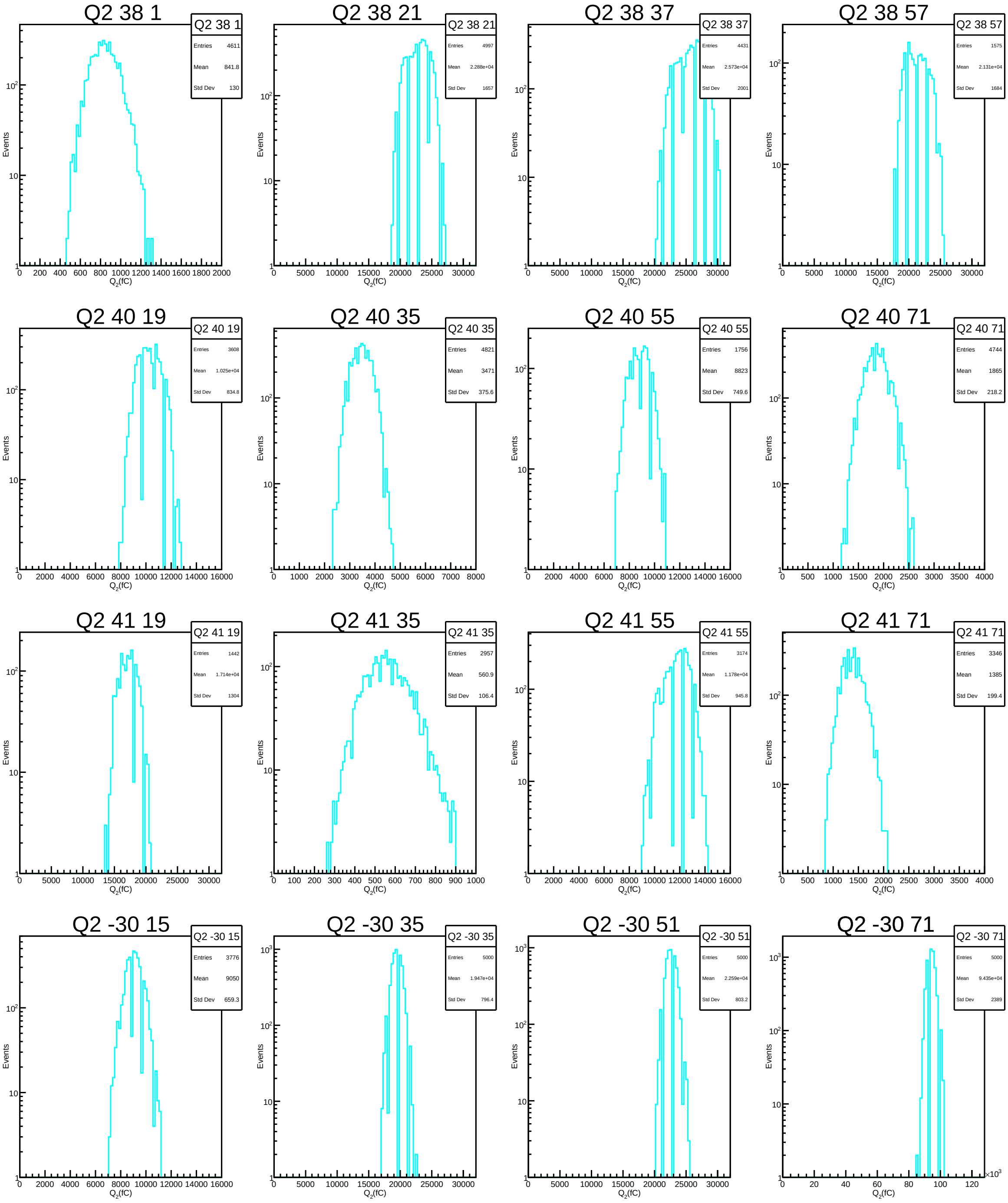

Figure A.4. Q_2 histograms of all channels in run 321585 (cont.).

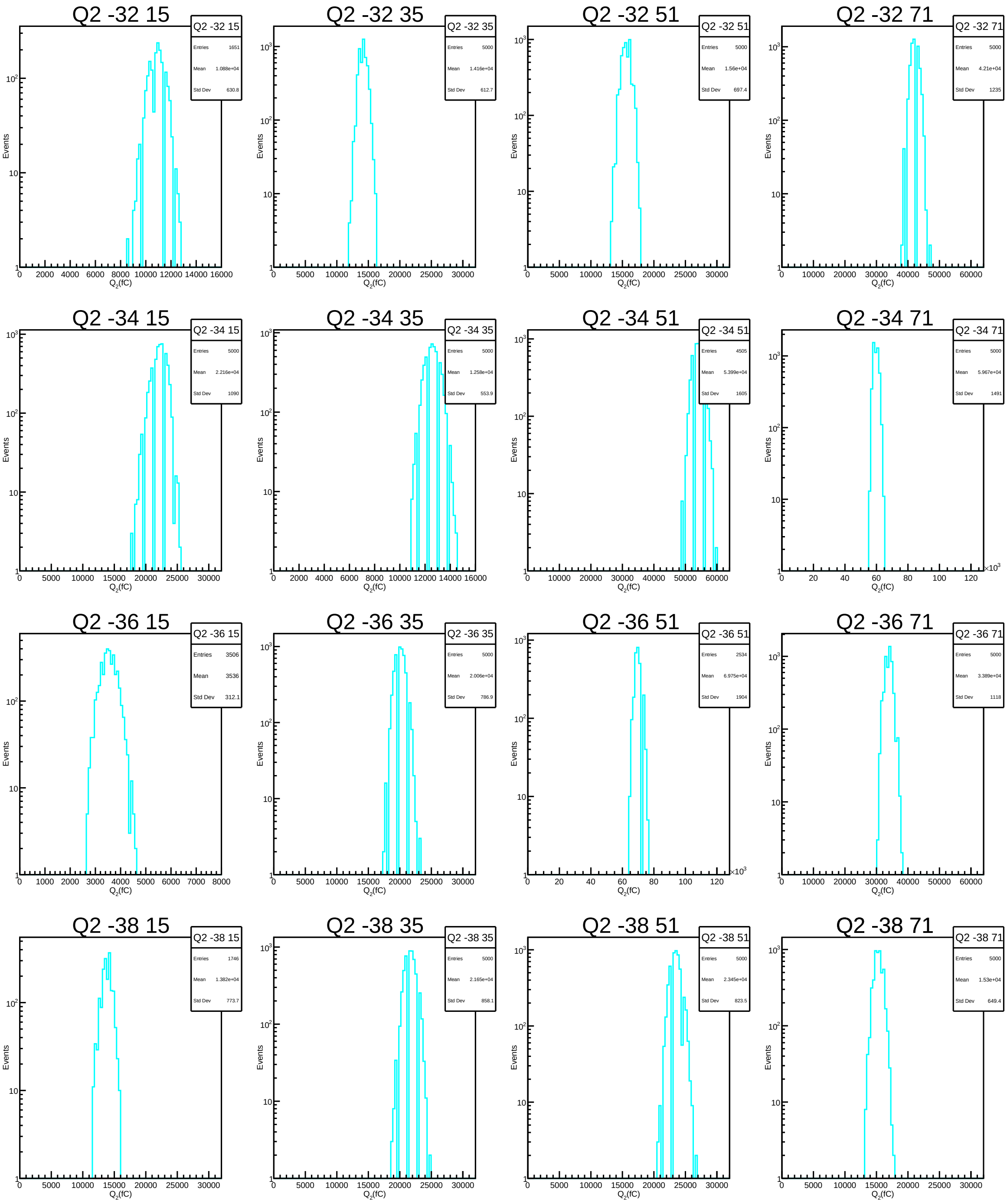

Figure A.4. Q_2 histograms of all channels in run 321585 (cont.).

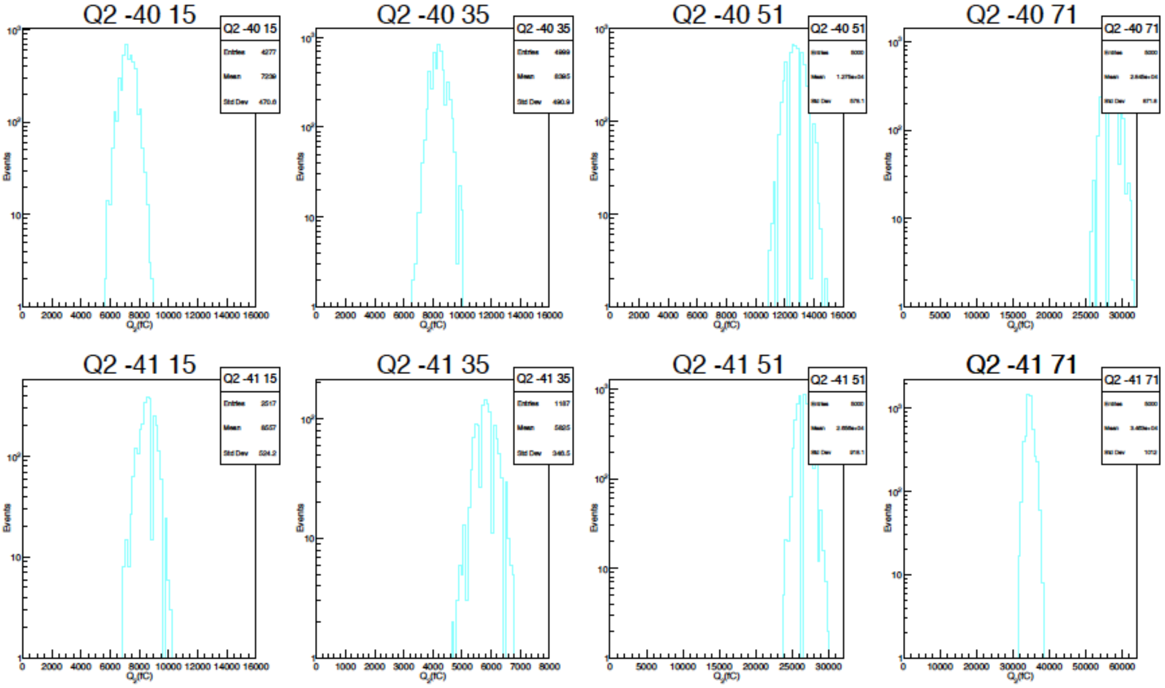

Figure A.4. Q_2 histograms of all channels in run 321585 (cont.).

A.5. $\frac{Q_2}{Q_1}$ Histograms

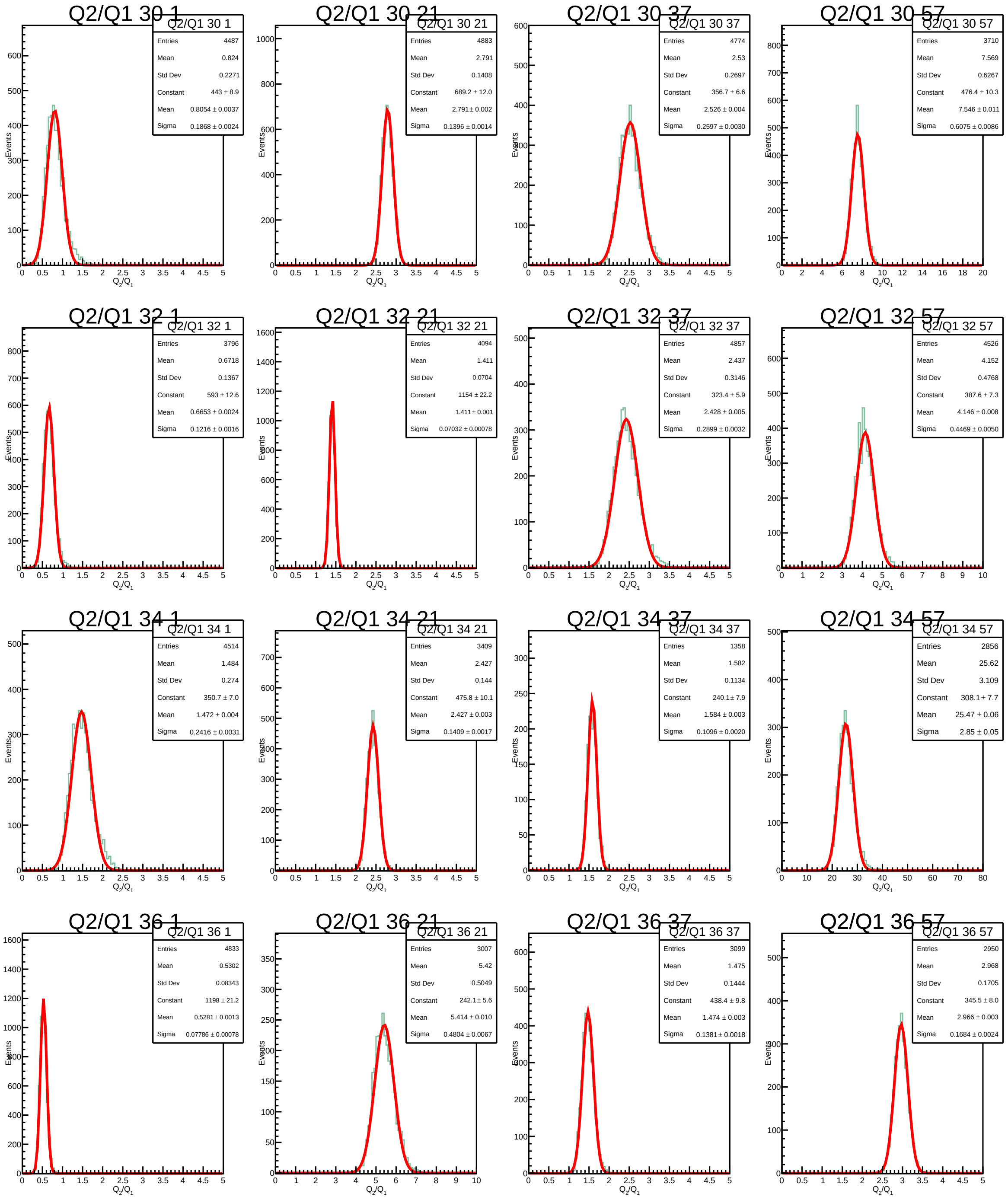

Figure A.5. $\frac{Q_2}{Q_1}$ histograms of all channels in run 321585.

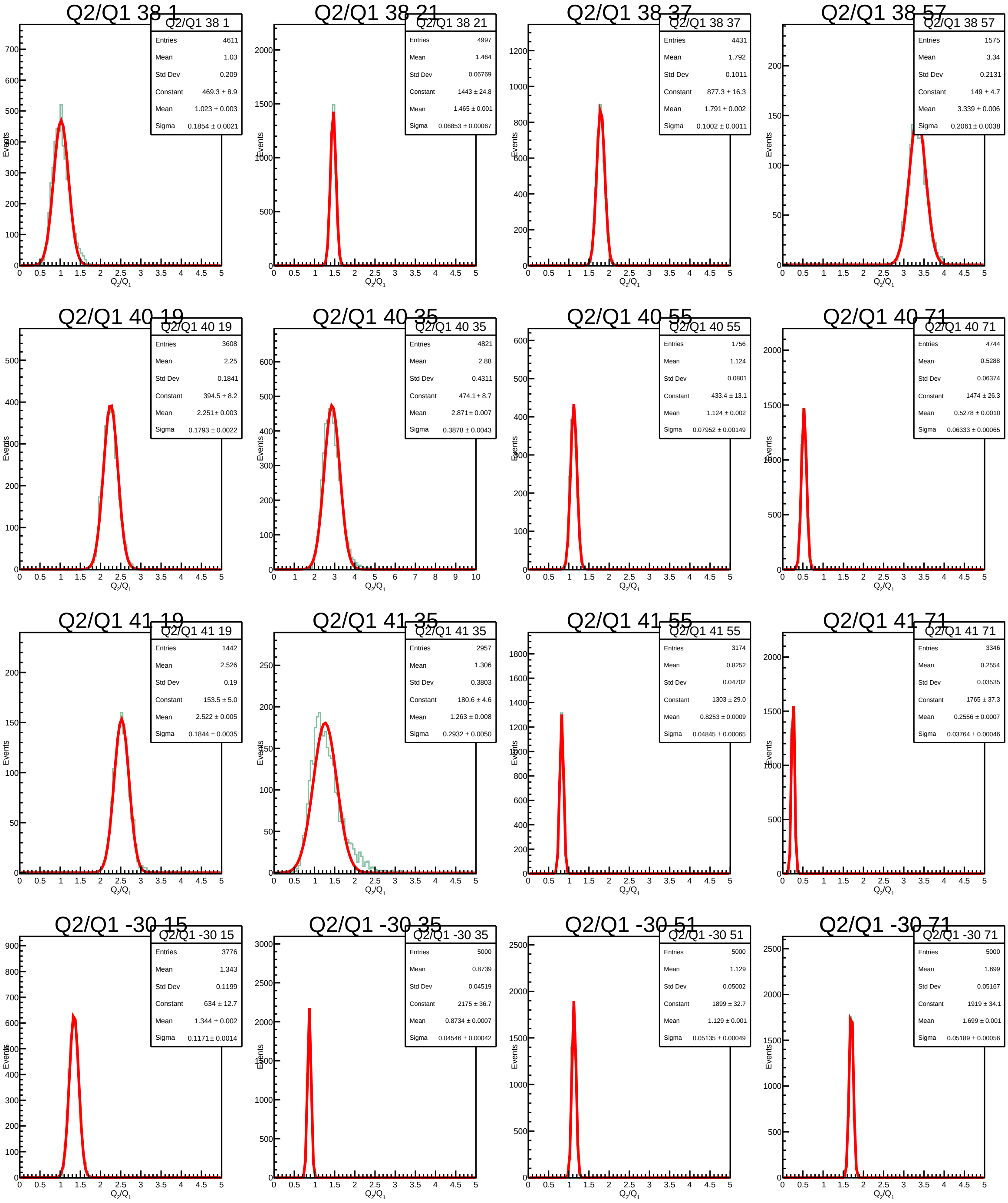

Figure A.5. $\frac{Q_2}{Q_1}$ histograms of all channels in run 321585 (cont.).

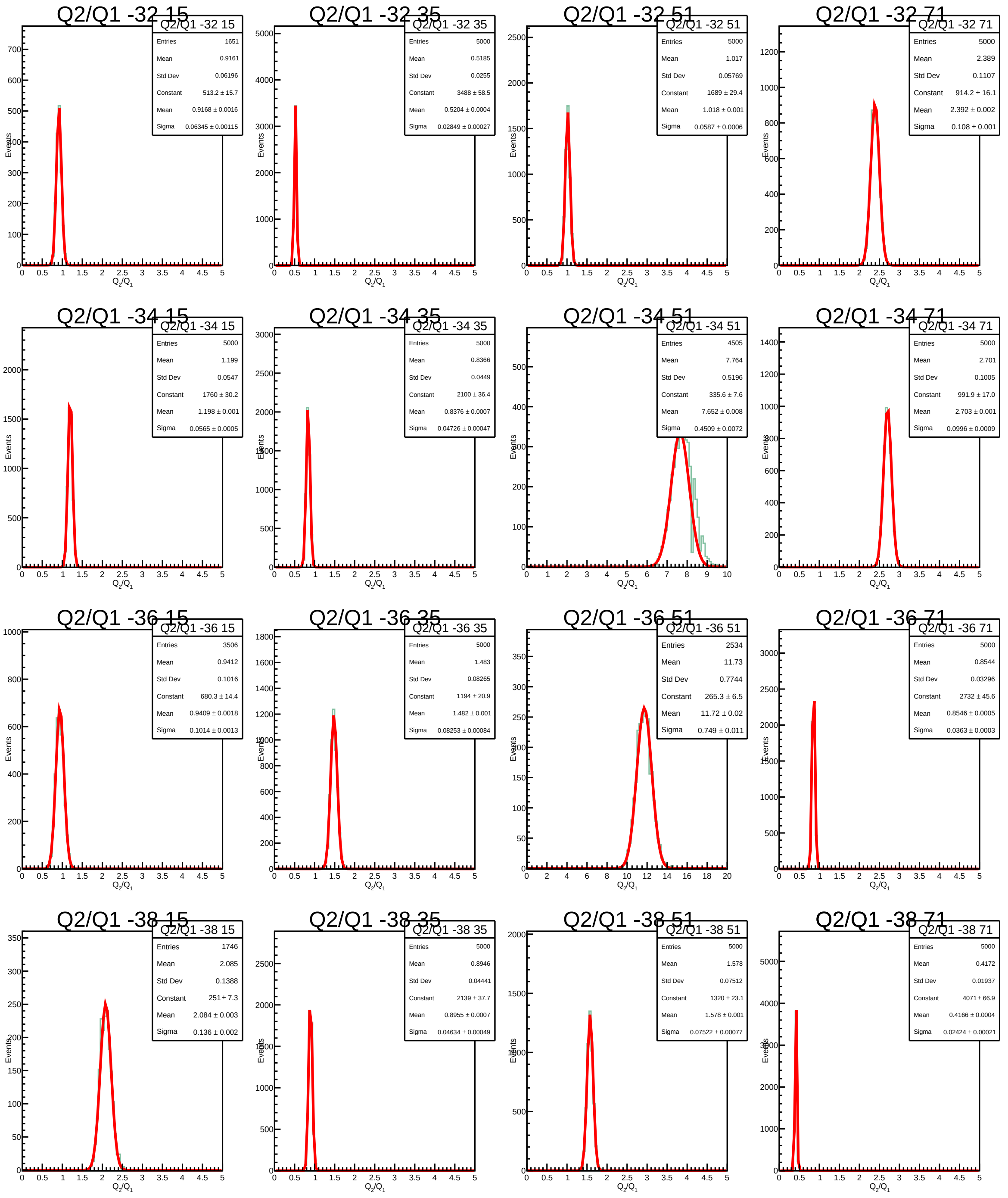

Figure A.5. $\frac{Q_2}{Q_1}$ histograms of all channels in run 321585 (cont.).

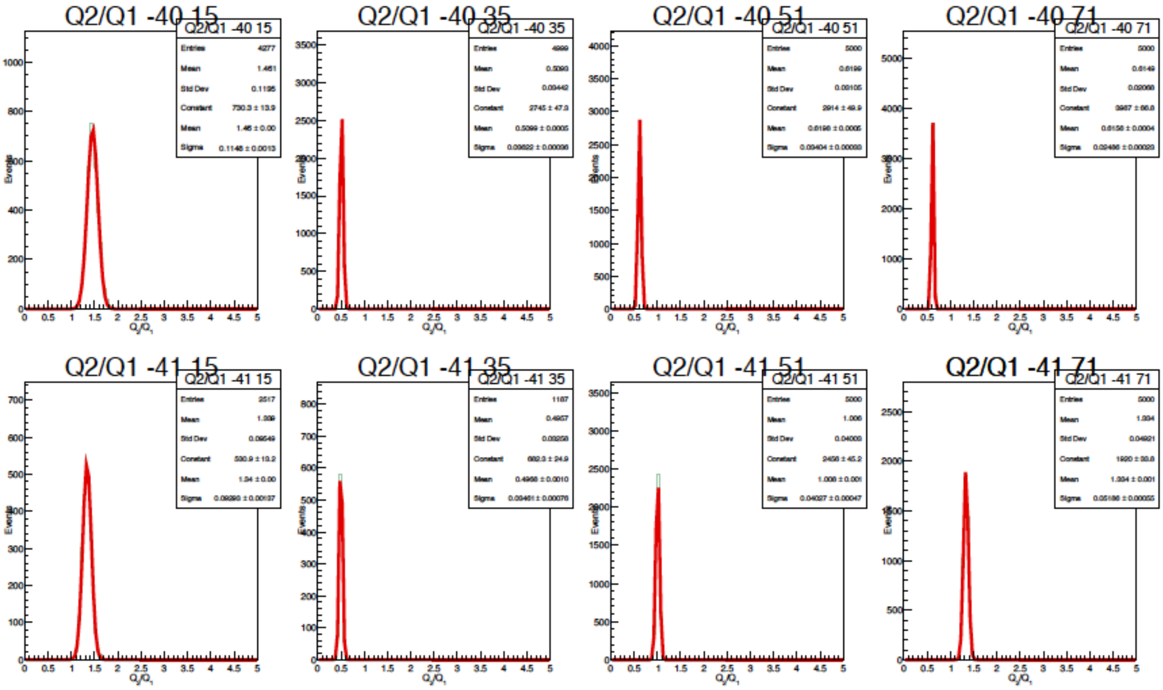

Figure A.5. $\frac{Q_2}{Q_1}$ histograms of all channels in run 321585 (cont.).

A.6. TS_2 TDC Scatter Plots

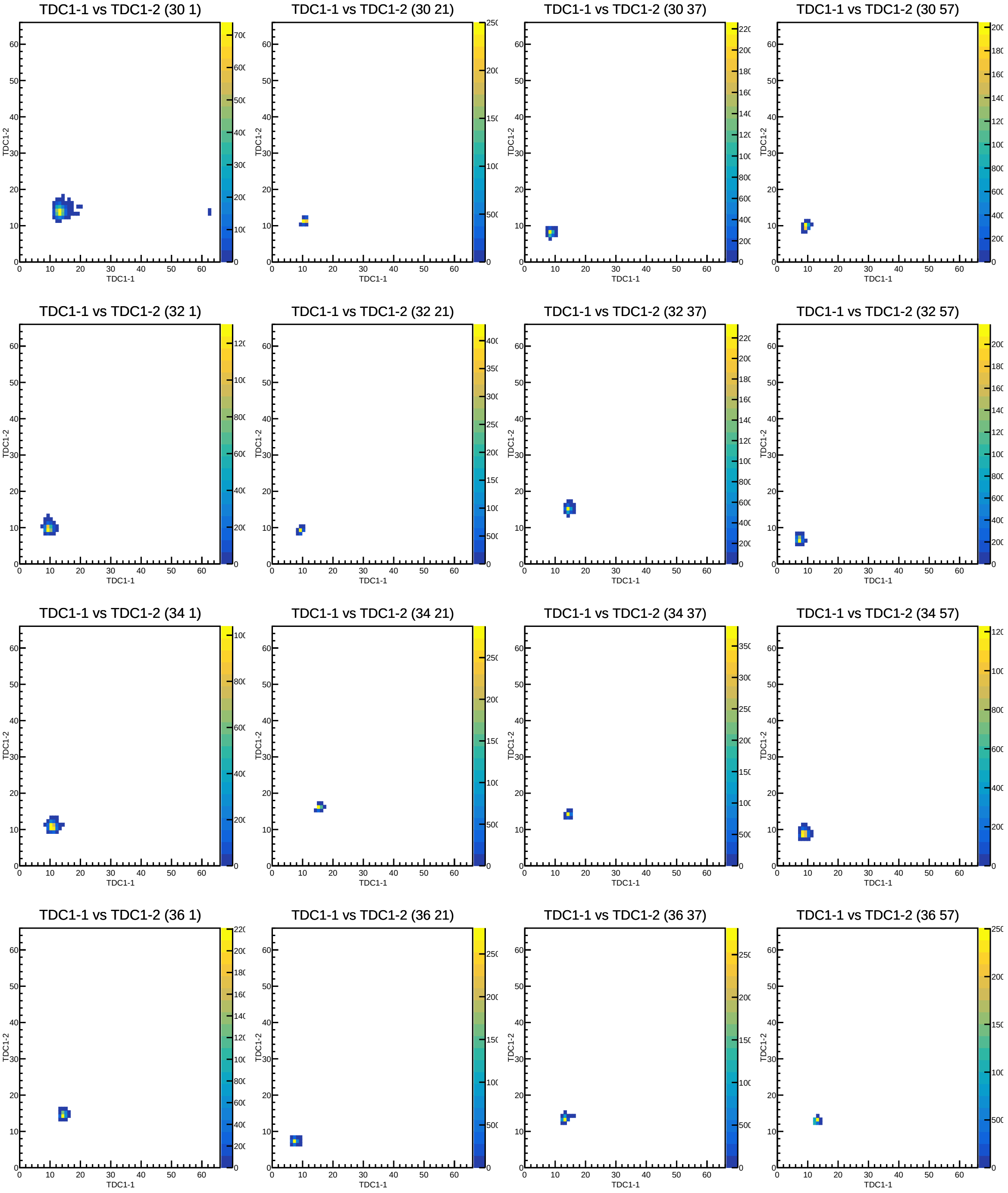

Figure A.6. Scatter plots of all TDC channels belonging to time slice 2 in run 321585.

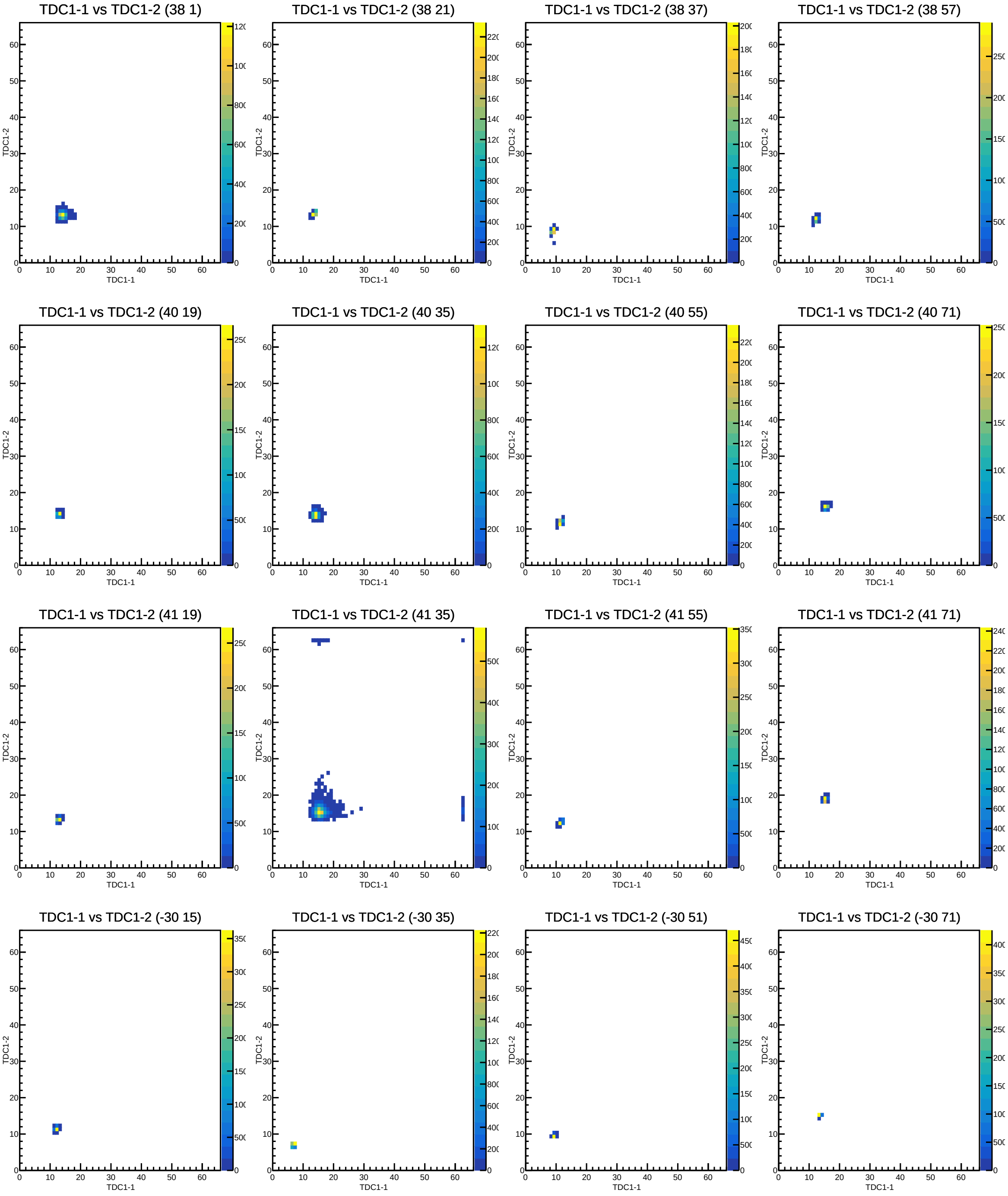

Figure A.6. Scatter plots of all TDC channels belonging to time slice 2 in run 321585 (cont.).

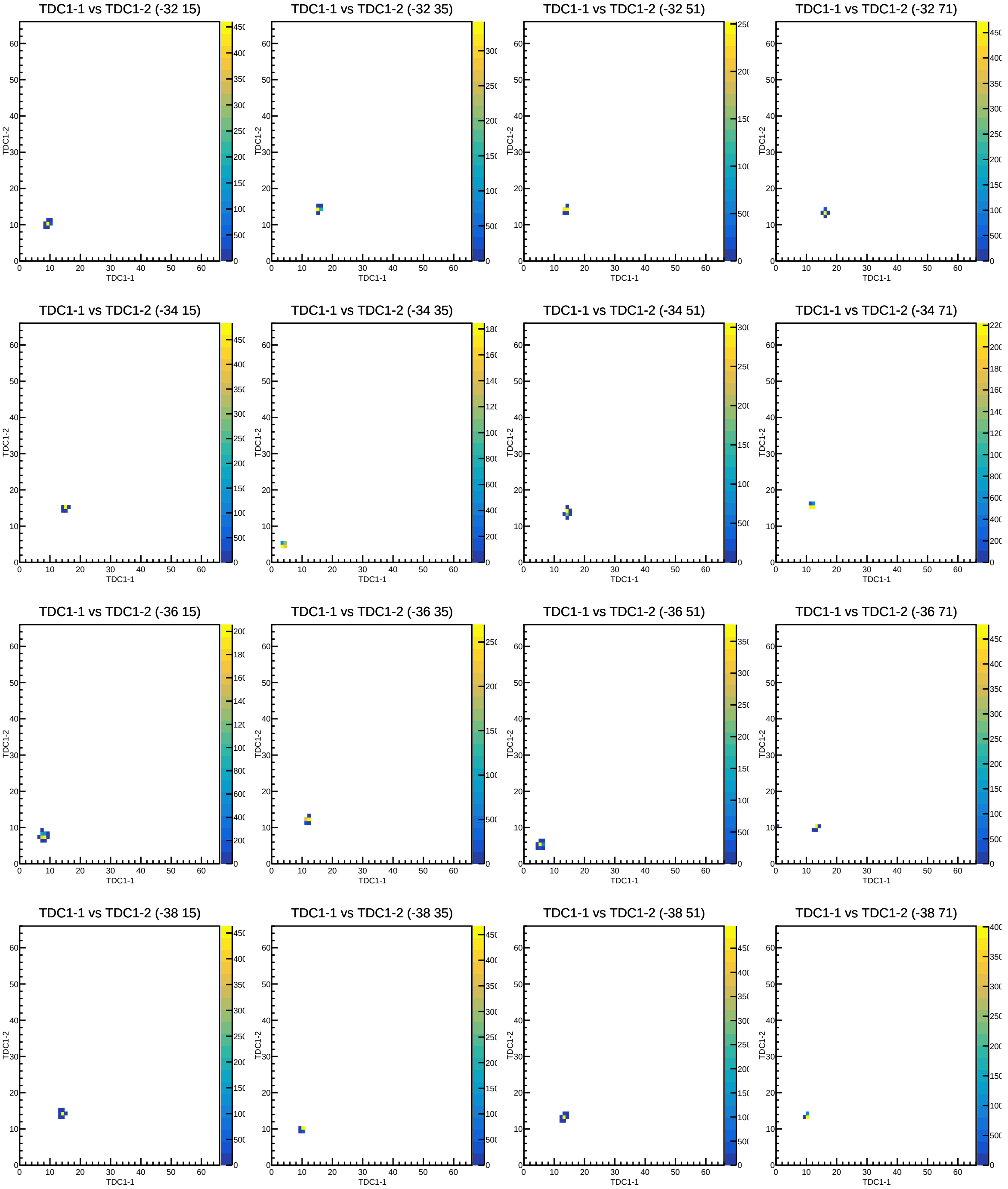

Figure A.6. Scatter plots of all TDC channels belonging to time slice 2 in run 321585 (cont.).

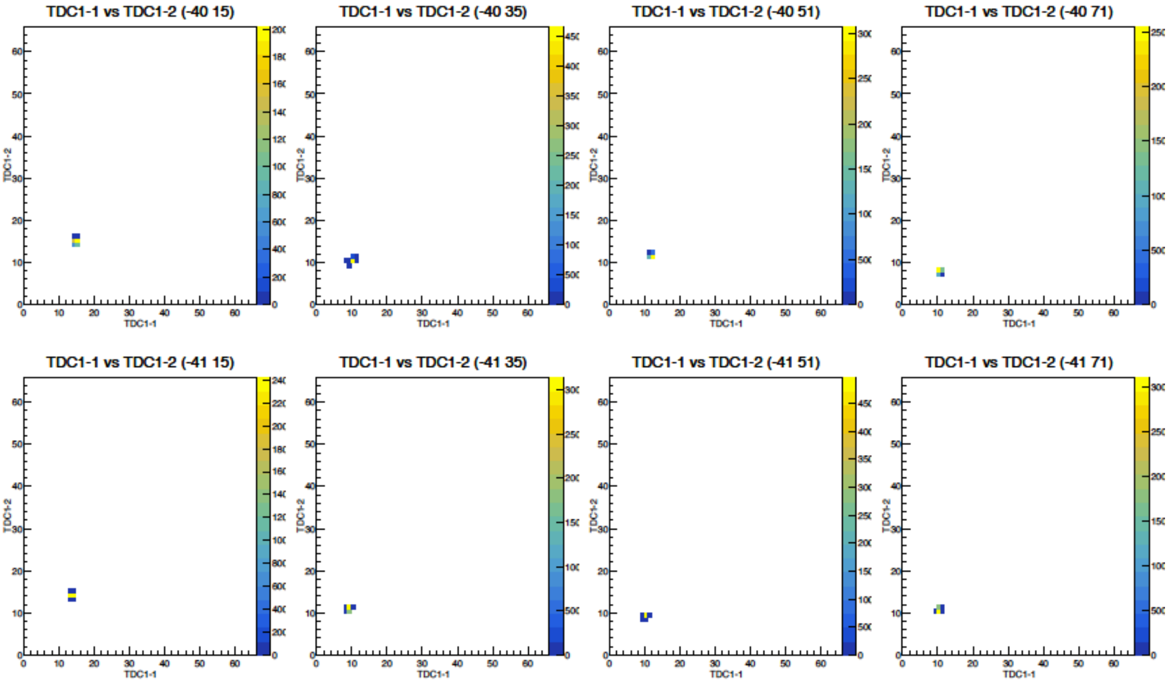

Figure A.6. Scatter plots of all TDC channels belonging to time slice 2 in run 321585 (cont.).

A.7. TS_3 TDC Scatter Plots

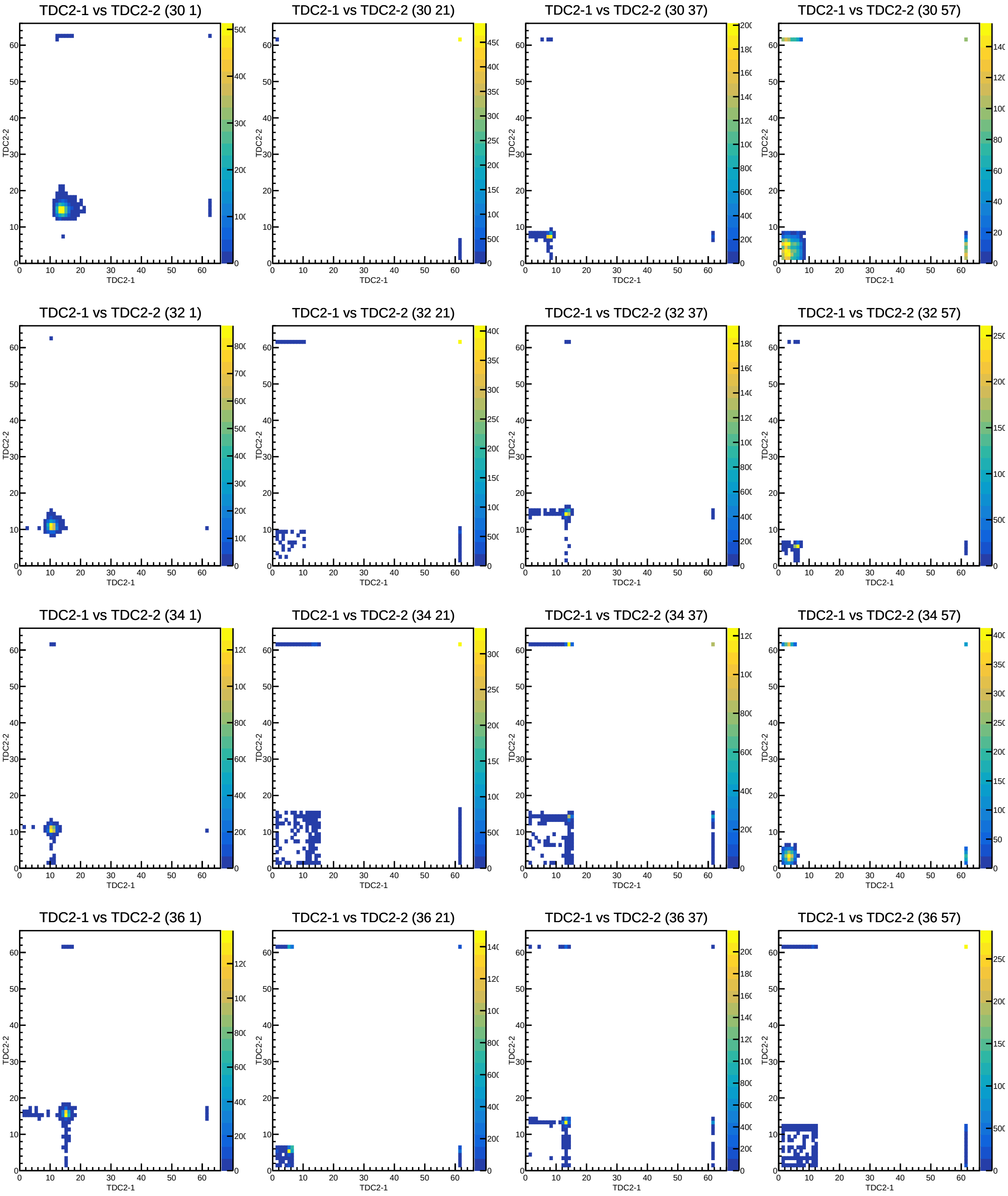

Figure A.7. Scatter plots of all TDC channels belonging to time slice 3 in run 321585.

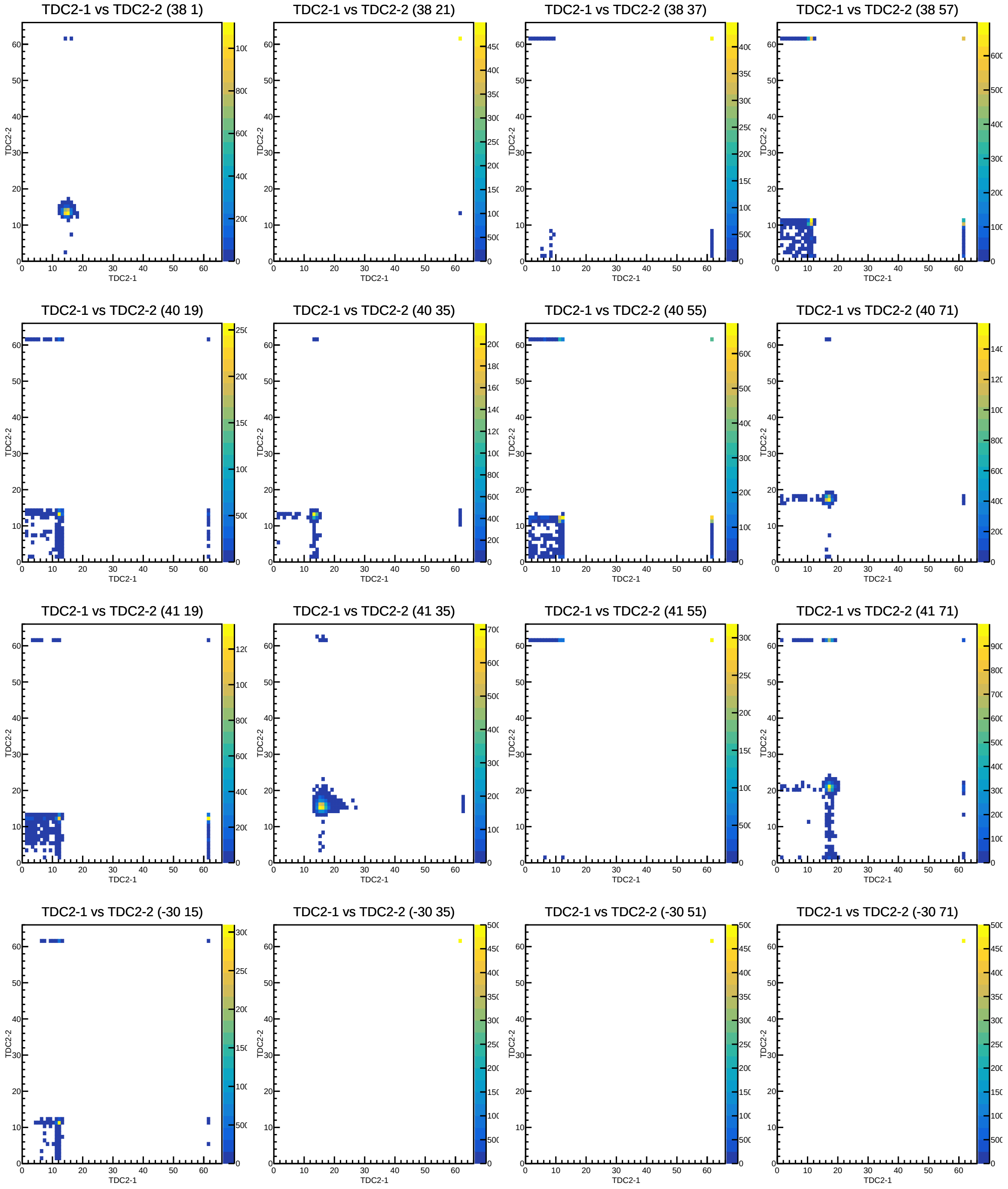

Figure A.7. Scatter plots of all TDC channels belonging to time slice 3 in run 321585 (cont.).

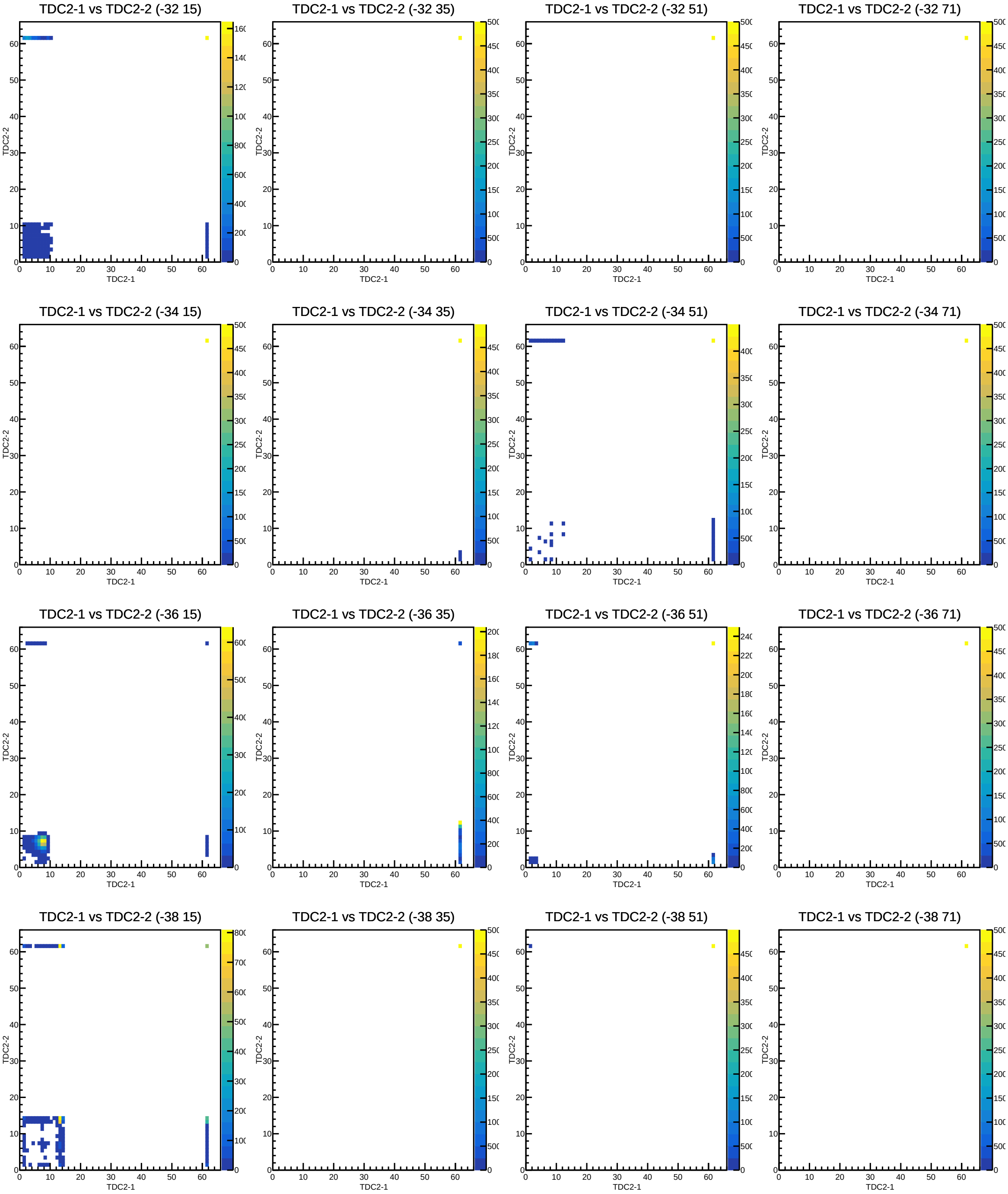

Figure A.7. Scatter plots of all TDC channels belonging to time slice 3 in run 321585 (cont.).

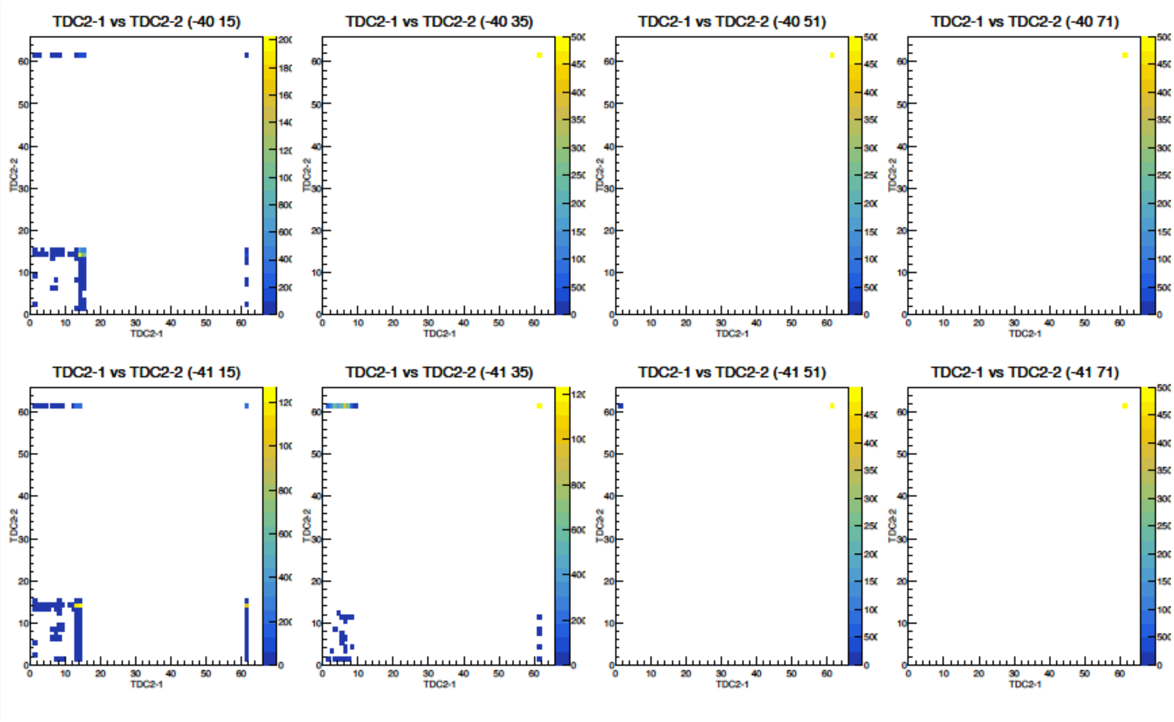

Figure A.7. Scatter plots of all TDC channels belonging to time slice 3 in run 321585 (cont.).

A.8. TS_2 ADC Scatter Plots

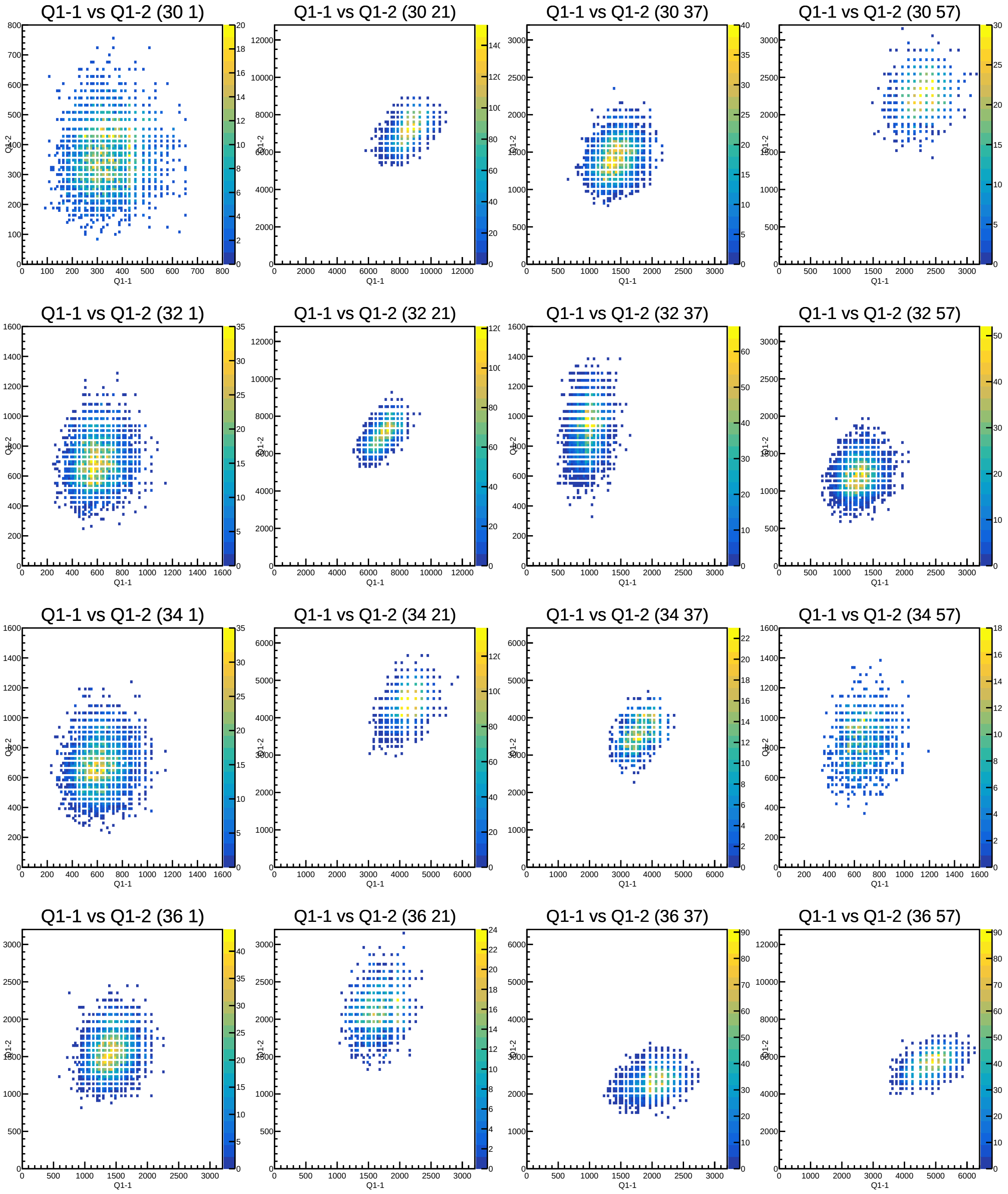

Figure A.8. Scatter plots of all ADC channels belonging to time slice 2 in run 321585.

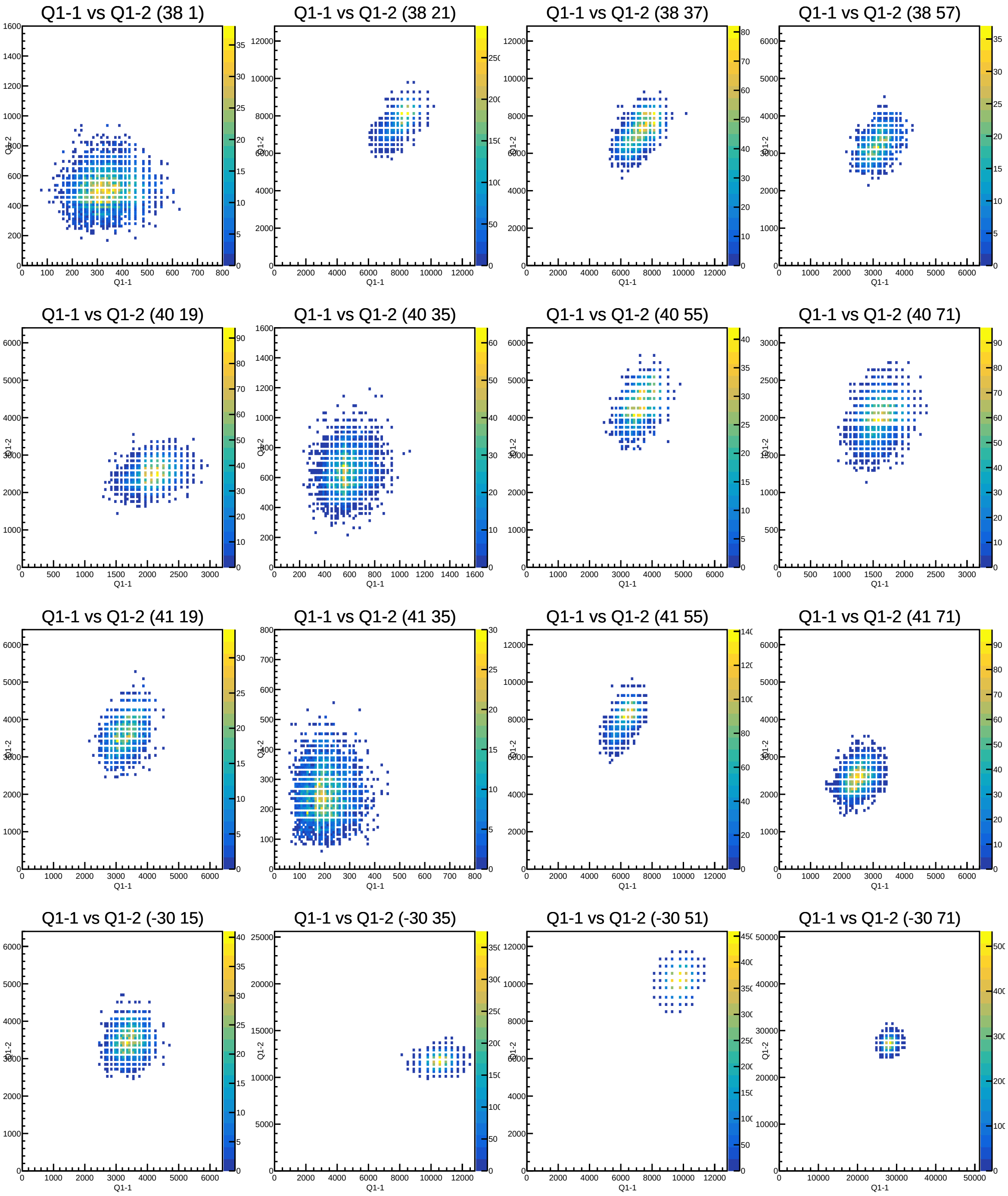

Figure A.8. Scatter plots of all ADC channels belonging to time slice 2 in run 321585 (cont.).

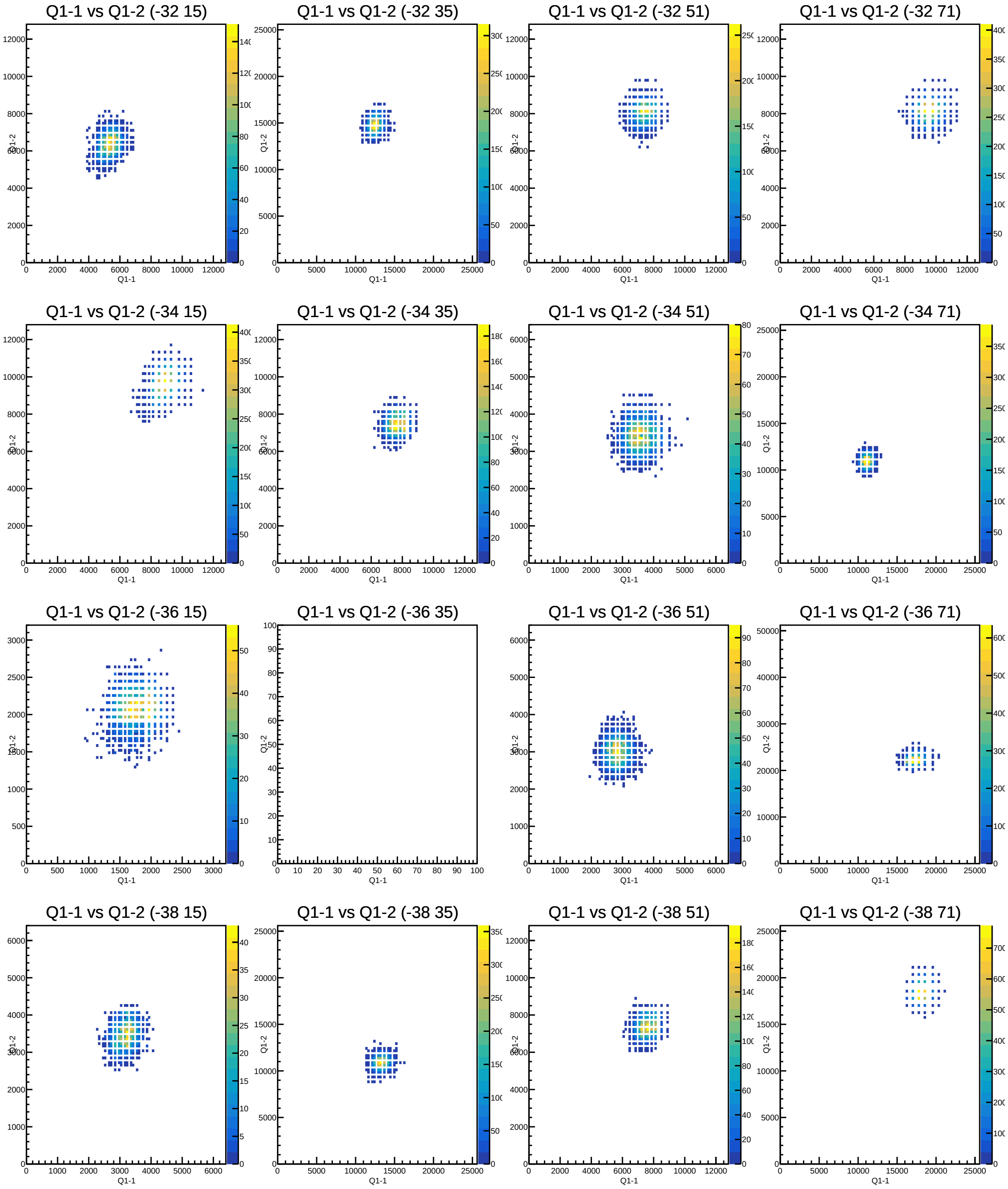

Figure A.8. Scatter plots of all ADC channels belonging to time slice 2 in run 321585 (cont.).

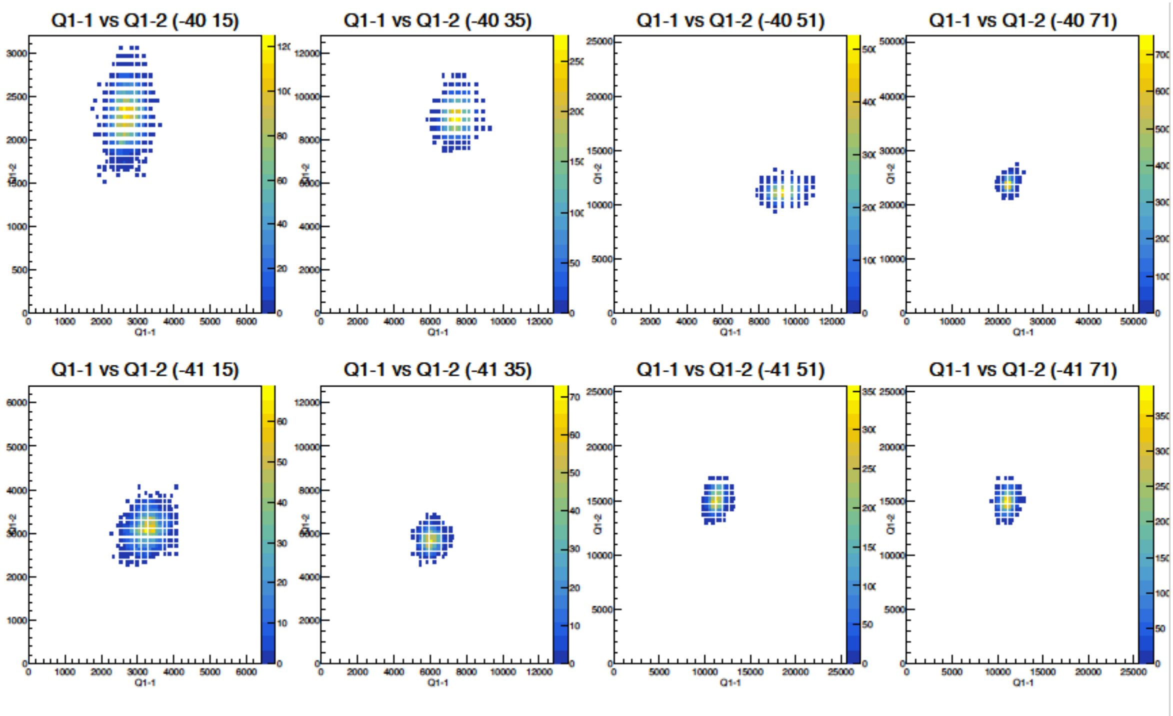

Figure A.8. Scatter plots of all ADC channels belonging to time slice 2 in run 321585 (cont.).

A.9. TS_3 ADC Scatter Plots

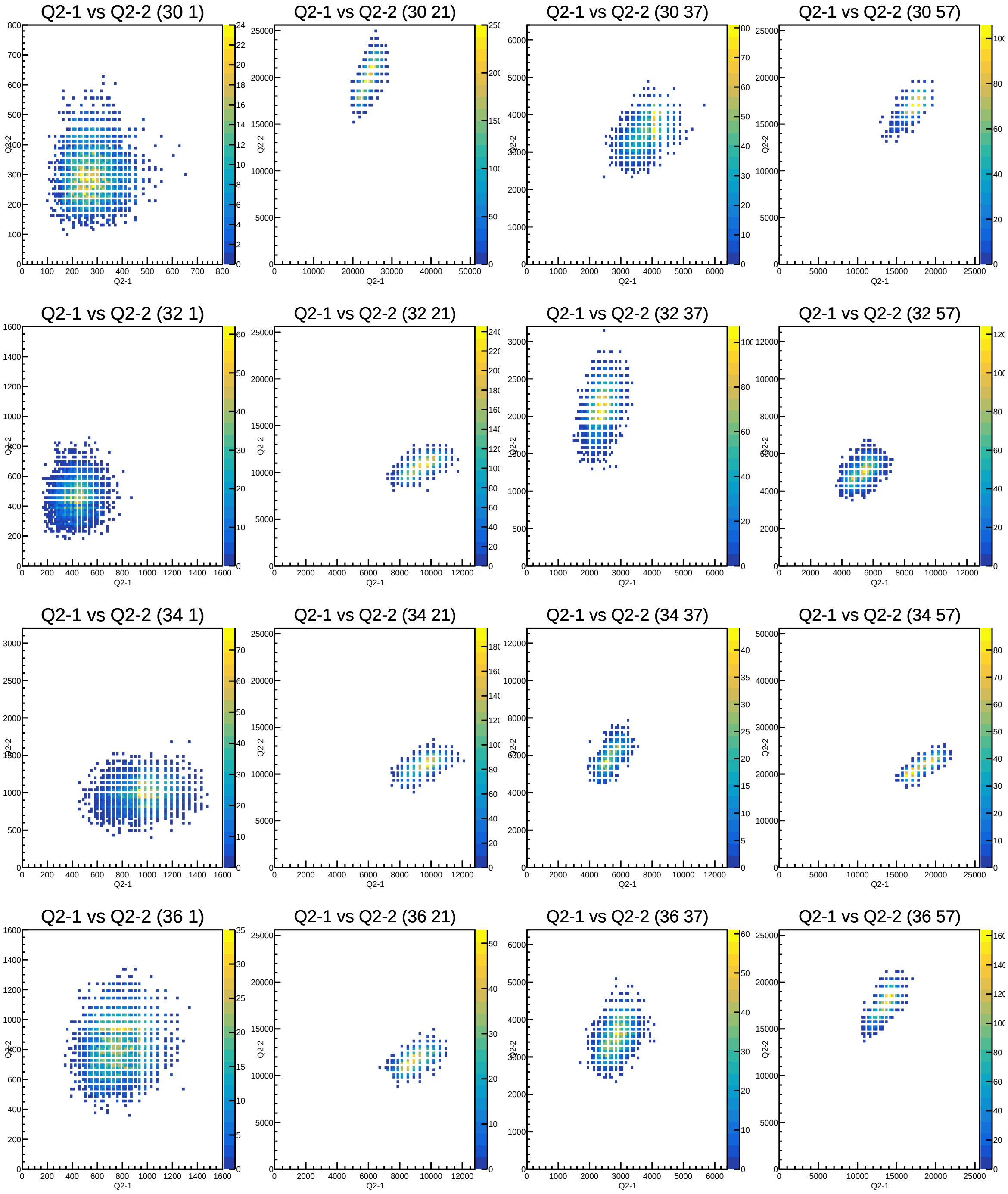
Q2-1 vs Q2-2 (30 1)
Q2-1 vs Q2-2 (30 21)
Q2-1 vs Q2-2 (30 37)
Q2-1 vs Q2-2 (30 57)
Q2-1 vs Q2-2 (32 1)
Q2-1 vs Q2-2 (32 21)
Q2-1 vs Q2-2 (32 37)
Q2-1 vs Q2-2 (32 57)
Q2-1 vs Q2-2 (34 1)
Q2-1 vs Q2-2 (34 21)
Q2-1 vs Q2-2 (34 37)
Q2-1 vs Q2-2 (34 57)
Q2-1 vs Q2-2 (36 1)
Q2-1 vs Q2-2 (36 21)
Q2-1 vs Q2-2 (36 37)
Q2-1 vs Q2-2 (36 57)

Figure A.9. Scatter plots of all ADC channels belonging to time slice 3 in run 321585.

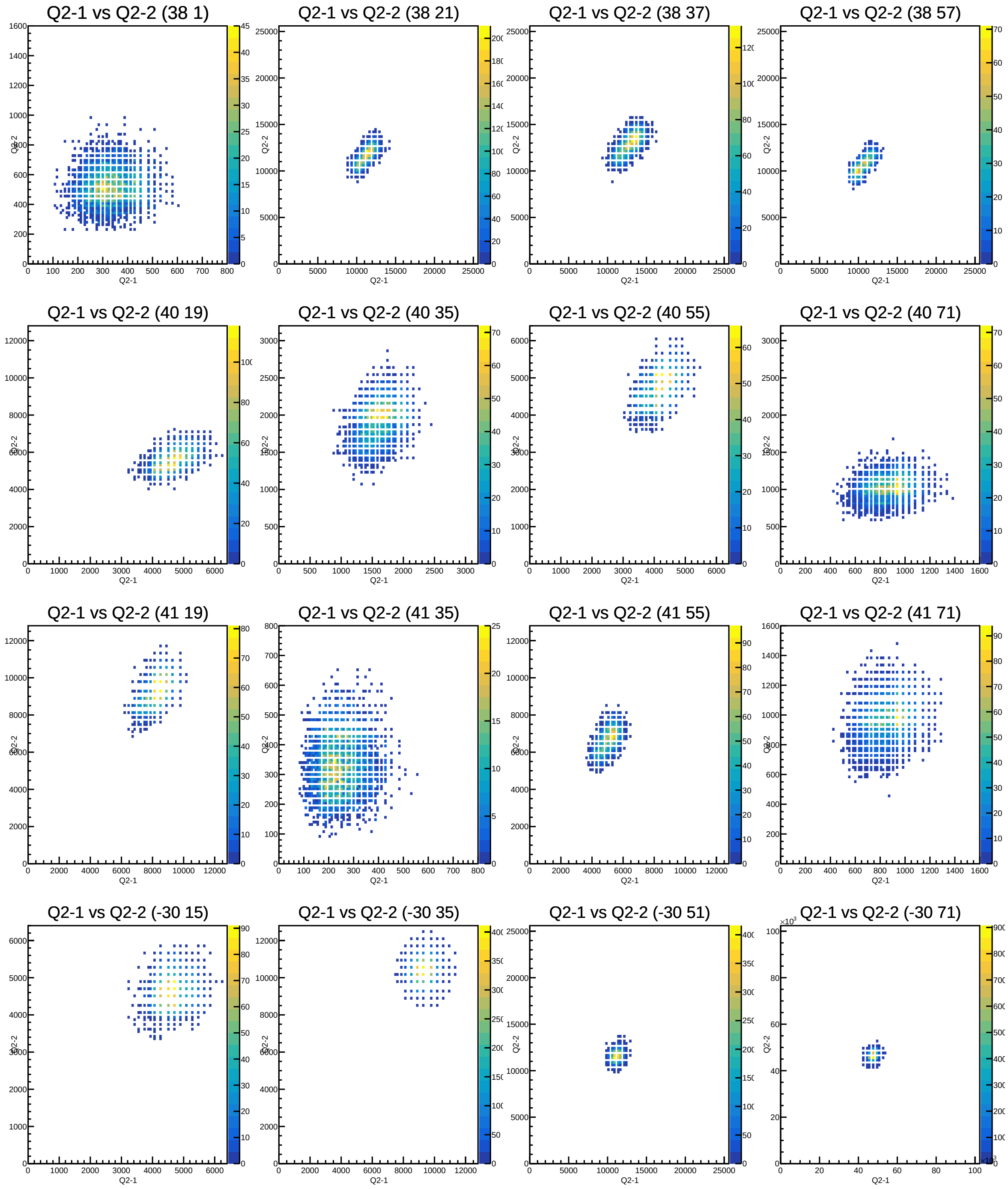

Figure A.9. Scatter plots of all ADC channels belonging to time slice 3 in run 321585 (cont.).

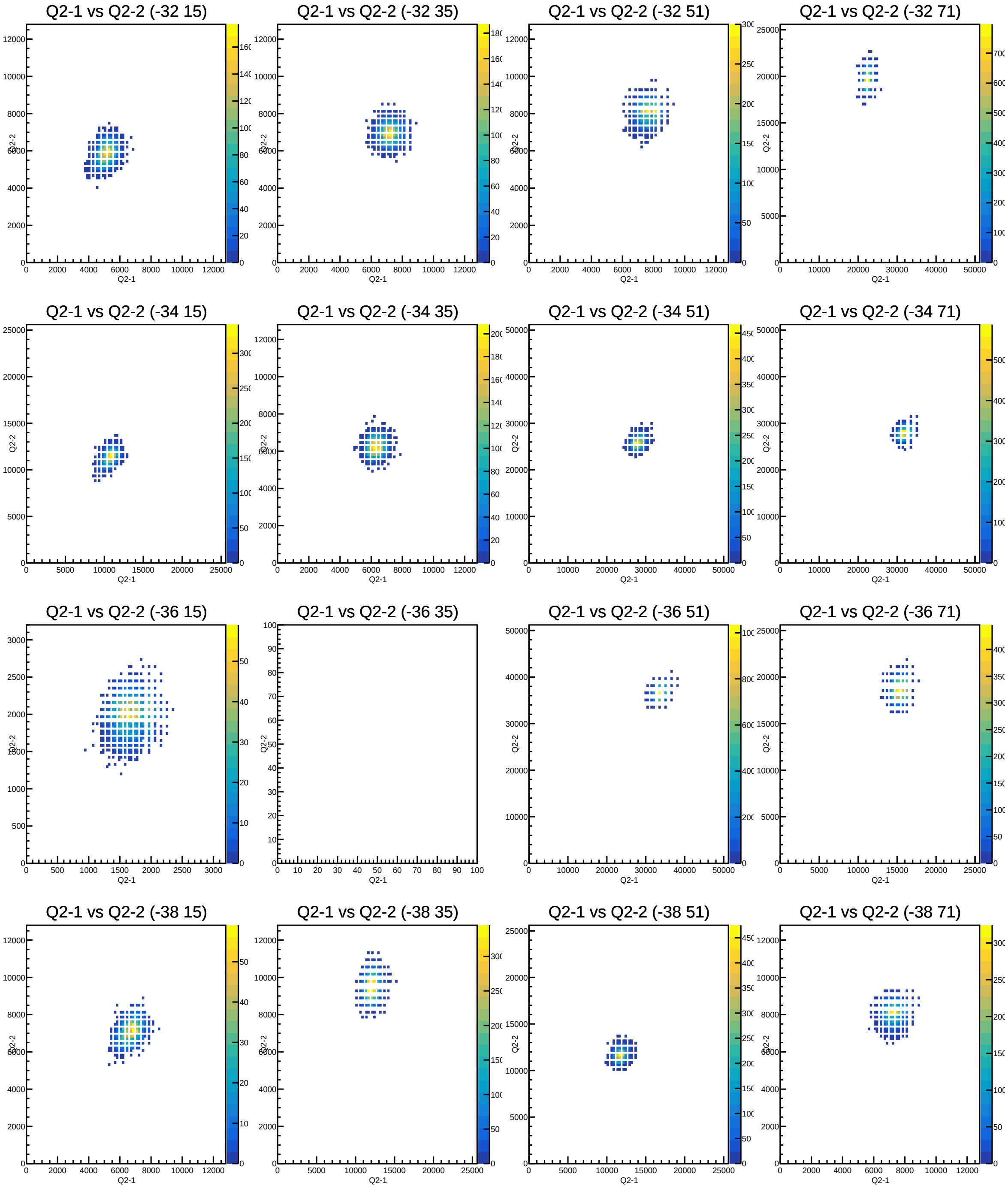

Figure A.9. Scatter plots of all ADC channels belonging to time slice 3 in run 321585 (cont.).

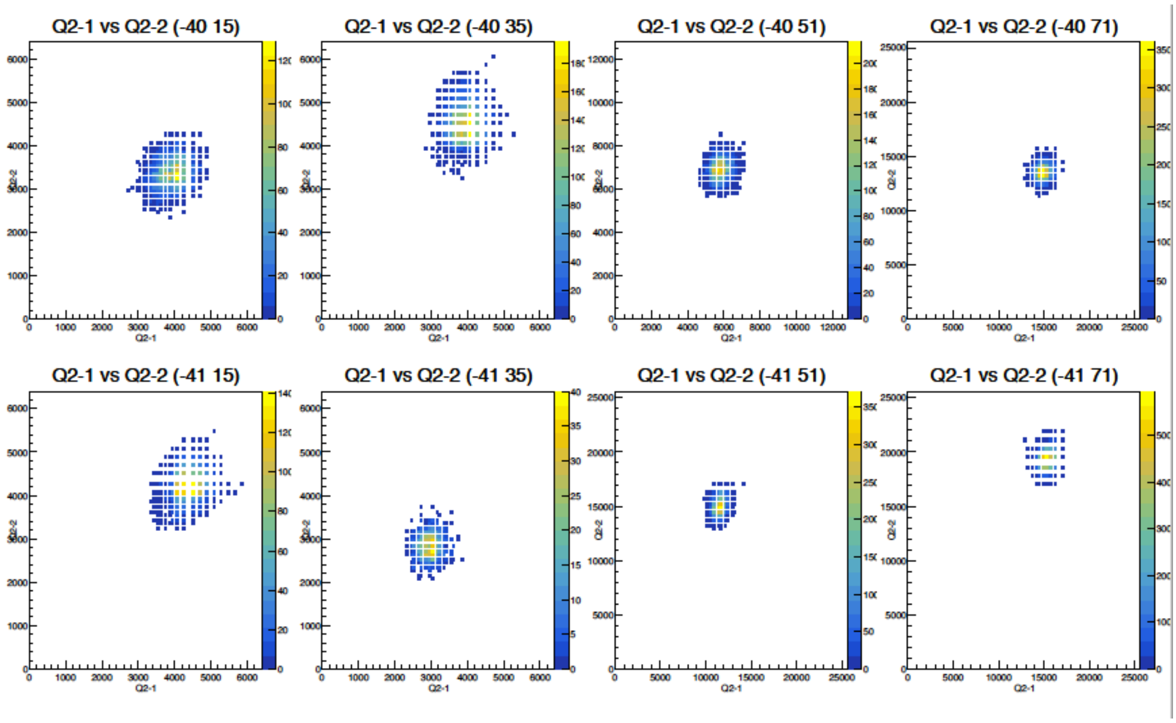

Figure A.9. Scatter plots of all ADC channels belonging to time slice 3 in run 321585 (cont.).